



Pacific Northwest
NATIONAL LABORATORY

*Proudly Operated by **Battelle** Since 1965*

Validated Models for Radiation Response and Signal Generation in Scintillators: Final Report

PL10-Scin-theor-PD2Jf

October 2014

SN Kerisit
F Gao
YL Xie
LW Campbell

RM Van Ginhoven
ZG Wang
MP Prange
DX Wu

DISCLAIMER

This report was prepared as an account of work sponsored by an agency of the United States Government. Neither the United States Government nor any agency thereof, nor Battelle Memorial Institute, nor any of their employees, makes **any warranty, express or implied, or assumes any legal liability or responsibility for the accuracy, completeness, or usefulness of any information, apparatus, product, or process disclosed, or represents that its use would not infringe privately owned rights.** Reference herein to any specific commercial product, process, or service by trade name, trademark, manufacturer, or otherwise does not necessarily constitute or imply its endorsement, recommendation, or favoring by the United States Government or any agency thereof, or Battelle Memorial Institute. The views and opinions of authors expressed herein do not necessarily state or reflect those of the United States Government or any agency thereof.

PACIFIC NORTHWEST NATIONAL LABORATORY
operated by
BATTELLE
for the
UNITED STATES DEPARTMENT OF ENERGY
under Contract DE-AC05-76RL01830

Printed in the United States of America

Available to DOE and DOE contractors from the
Office of Scientific and Technical Information,
P.O. Box 62, Oak Ridge, TN 37831-0062;
ph: (865) 576-8401
fax: (865) 576-5728
email: reports@adonis.osti.gov

Available to the public from the National Technical Information Service
5301 Shawnee Rd., Alexandria, VA 22312
ph: (800) 553-NTIS (6847)
email: orders@ntis.gov <<http://www.ntis.gov/about/form.aspx>>
Online ordering: <http://www.ntis.gov>



This document was printed on recycled paper.

(8/2010)

Validated Models for Radiation Response and Signal Generation in Scintillators: Final Report

SN Kerisit	RM Van Ginhoven
F Gao	ZG Wang
YL Xie	MP Prange
LW Campbell	DX Wu

October 2014

Prepared for
the U.S. Department of Energy
under Contract DE-AC05-76RL01830

Pacific Northwest National Laboratory
Richland, Washington 99352

Abstract

This Final Report presents work carried out at Pacific Northwest National Laboratory (PNNL) under the project entitled “Validated Models for Radiation Response and Signal Generation in Scintillators” (Project number: PL10-Scin-theor-PD2Jf) and led by Drs. Fei Gao and Sebastien N. Kerisit.

This project was divided into four tasks:

- 1) Electronic response functions (*ab initio* data model)
- 2) Electron-hole yield, variance, and spatial distribution
- 3) *Ab initio* calculations of information carrier properties
- 4) Transport of electron-hole pairs and scintillation efficiency

Detailed information on the results obtained in each of the four tasks is provided in this Final Report. Furthermore, published peer-reviewed articles based on the work carried under this project are included in Appendix.

This work was supported by the National Nuclear Security Administration, Office of Nuclear Nonproliferation Research and Development (DNN R&D/NA-22), of the U.S. Department of Energy (DOE).

Acronyms and Abbreviations

DOE	Department of Energy
ERSP	Electronic ReSPonse
FY	Fiscal Year
GGA	Generalized Gradient Approximation
KMC	Kinetic Monte Carlo
LDA	Local-Density Approximation
LLNL	Lawrence Livermore National Laboratory
LO	Longitudinal Optical
NWEGRIM	NorthWest Electron and Gamma-Ray Interaction with Matter
PNNL	Pacific Northwest National Laboratory
STE	Self-Trapped Exciton
STH	Self-Trapped Hole
WFU	Wake Forest University

Contents

Abstract	iii
Acronyms and Abbreviations	iv
1.0 Objective, Strategy, and Findings Summary	1.7
1.1 Objective	1.7
1.2 Computational strategy	1.7
1.3 Summary of findings and achievements	1.7
2.0 Task 1: Electronic response functions (<i>ab initio</i> data model)	2.9
2.1 Summary of progress	2.9
2.2 Peer-reviewed publications	2.9
2.3 Progress during project.....	2.9
3.0 Task 2: Electron-hole yield, variance and spatial distribution.....	3.11
3.1 Summary of progress	3.11
3.2 Peer-reviewed publications	3.11
3.3 Progress during project.....	3.11
4.0 Task 3: <i>Ab initio</i> calculations of information carrier properties.....	4.13
4.1 Summary of progress	4.13
4.2 Peer-reviewed publications	4.13
4.3 Progress during project.....	4.13
4.3.1 Intrinsic defects and Tl and Na dopants in CsI.....	4.13
4.3.2 Self-trapped excitations in pure and Tl-doped NaI	4.14
5.0 Task 4: Transport of electron-hole pairs and scintillation efficiency	5.15
5.1 Summary of progress	5.15
5.2 Peer-reviewed publications	5.15
5.3 Progress during project.....	5.15
5.3.1 Electron thermalization in halide scintillators.....	5.15
5.3.2 Nonlinear quenching of electron-hole pairs (STE-STE annihilation)	5.17

Figures

Fig. 1. Flow chart of computational modeling process (with names of the codes developed in this project shown in the upper left-hand corners of each box).....	1.7
Fig. 2. Dielectric function (a and c) and energy loss function (b and d) of electrons in CaF ₂ (top) and BaF ₂ (bottom).....	2.10
Fig. 3. Calculated and experimental electron energy loss spectra of CsI (left) and NaI (right). ...	2.10
Fig. 4. Mean energy per electron-hole pair, W , and Fano factor, F , as a function of incident photon energy for NaI (left) and CsI (right).	3.11
Fig. 5. Calculated spatial distributions of electron-hole pairs for 10-keV photon events in NaI (left) and CsI (right), where electrons and holes are distinguished by size and color, as indicated in the legend.	3.12
Fig. 6. Stopping power as a function of electron energy in BaF ₂ (left) and CaF ₂ (right). Also shown are results from the Bethe-Bloch equation and the ESTAR program.	3.12
Fig. 7. Defects levels in CsI. LDA and GGA (PBE) are both shown, results are the same within errors of the techniques.....	4.13
Fig. 8. The four near-neighbor hops available to the STE or STH in NaI.	4.14
Fig. 9. Spin density isosurfaces drawn at 0.001 electron/bohr ³ around an STE (left) and the transition state for a 120° STH jump (right).	4.14
Fig. 10. Electron-phonon scattering rates as a function of electron energy.....	5.16
Fig. 11. Distance distributions of the (a) recombined and (b) stopped electrons for a 2-keV incident γ -ray.	5.16
Fig. 12. Time distributions of the (a) recombined and (b) stopped electrons for a 2-keV incident γ -ray.	5.16
Fig. 13. Fraction of Tl-trapped electrons and recombined electron-hole pairs as a function of Tl concentration for an incident γ -ray energy of 2 keV	5.16
Fig. 14. Fraction of Tl-trapped, stopped and recombined electrons as a function of incident γ -ray energy for a Tl concentration of 0.1 mol%.	5.16
Fig. 15. Schematic of the elementary species (black), elementary processes (blue), and possible final outcomes (red) considered in the KMC model of scintillation.....	5.17
Fig. 16. Calculated light yield as a function of z-position and excitation density and comparison with the z-scan data and second-order component determined by WFU.....	5.17
Fig. 17. Decay curves of the (Tl ⁺) [*] emission of CsI:0.3%Tl calculated at two excitation densities and comparison with the WFU experimental results.	5.17
Fig. 18. Decay curves of the STE emission of pure CsI calculated at two excitation densities and comparison with the WFU experimental data.....	5.17

1.0 Objective, Strategy, and Findings Summary

1.1 Objective

This project aims to develop multiphysics simulation models, validated by innovative experiments, which predict radiation response and signal generation in inorganic scintillators. The models will enable identifying the physical limits of detection response in scintillators and provide a theoretical basis to improve performance and accelerate discovery of new scintillators.

1.2 Computational strategy

We have developed and applied a suite of physics models at multiple scales to simulate the three main stages of the scintillation process in γ -ray detectors: initial energy cascade to produce energetic particles; thermalization of particles into low-energy excitations, and relaxation of excitations to produce scintillation light. Simulations of these individual stages are combined to produce a unified approach that can predict scintillator performance from knowledge of a few material parameters (Fig. 1).

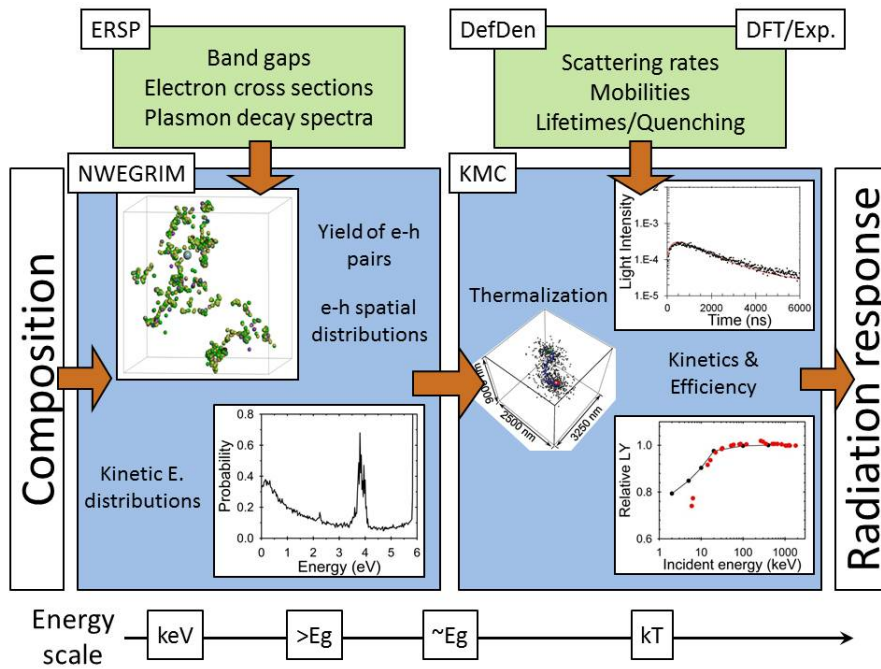


Fig. 1. Flow chart of computational modeling process (with names of the codes developed in this project shown in the upper left-hand corners of each box).

1.3 Summary of findings and achievements

We have developed a suite of computational physics models to simulate the γ -ray and electron response of inorganic scintillators over a wide range of length and time scales in order to provide a fundamental understanding of materials performance and the origins of nonproportionality. The methodological and scientific developments achieved in this lifecycle were greatly facilitated by

collaborations with experimentalists and theoreticians who are also involved in this program's effort to enhance our knowledge of scintillator physics.

Extensive developments of our in-house code of electronic response (ERSP) allowed us to compute the complex dielectric function and plasmon decay spectra of alkali and alkaline-earth halides, and good agreement was found with experimental data when available. These data, together with our *ab initio* data model for determining interaction cross sections, enabled us to determine the stopping power, mean energy per electron-hole pair, maximum theoretical light yield and spatial distribution of individual electron-hole pairs of a number of scintillator materials (NaI, CsI, BaF₂, CaF₂, LaBr₃, and SrI₂) using NWEGRIM.

Outputs of the NWEGRIM calculations served as input for the simulations of electron thermalization in alkali and alkaline-earth halides using a semi-classical phenomenological model implemented in a Monte Carlo code. This work provided, for the first time, a theoretical prediction of the spatial and temporal length scales involved in the thermalization stage of γ -ray irradiated inorganic scintillators.

Additionally, simulations of the transport of thermalized carriers were performed with our lattice kinetic Monte Carlo (KMC) code, in particular for CsI. These simulations were informed, in part, by electronic structure calculations of carriers and defects in scintillator lattices performed in this project. Notably, we developed and applied a cluster-based embedded *ab initio* approach, which, in combination with solid-state density functional theory calculations, was used to calculate the migration barriers of self-trapped holes and excitons and the driving force for capture at dopant sites. Through a collaboration with Prof. Williams at Wake Forest University, the KMC model was used to model the z-scan experiments carried out at WFU and enabled us to shed light on the mechanisms of nonlinear quenching.

The combination of these physics models has allowed us to develop an improved understanding of the elementary mechanisms that underlie the nonproportional behavior of inorganic scintillators. Namely, three mechanisms have been identified, confirmed, and/or quantified using our computational strategy:

1. Because of the rapid self trapping of holes and the low values of the LO phonon energies in alkali halides, electrons that escape the electric field of the holes during thermalization can travel long distances, resulting in significant charge separation. Large separation distances favor deep trapping of electrons over electron-hole recombination, thus reducing the scintillation efficiency. Because of the diminishing stopping power with increasing incident energy, this process becomes increasingly dominant at high incident energies and can explain the observed decreasing relative light yield of alkali halides at these incident energies.
2. At the end of the energy cascade and before thermalization, the ionization track terminates with a radius on the order of a few nanometers. In this volume, the carrier densities are high enough to prevent a significant fraction of the electrons from escaping the electric field of the holes in that region of the track during thermalization. The resulting rapid electron-hole pair recombination leads to the formation of closely located STEs that can participate in second-order nonlinear quenching.
3. At low incident energies, the increase in stopping power with decreasing incident energy leads to an increase in electron-hole pair density, which, following the mechanism described in 2, gives rise to increasing extents of nonlinear quenching through STE-STE annihilation. This phenomenon explains the decreasing relative light yield with decreasing incident energy observed for almost all inorganic scintillators.

2.0 Task 1: Electronic response functions (*ab initio* data model)

2.1 Summary of progress

A computer code (ERSP) was developed to determine the electronic loss rates of conduction electrons and holes from the ground state electronic structure of a given scintillator. Applications to four scintillators (CsI, NaI, CaF₂, BaF₂) are presented.

2.2 Peer-reviewed publications

L.W. Campbell and F. Gao *Journal of Luminescence* 137 (2013) 121-123

2.3 Progress during project

In this task, an in-house computer code (Electronic ReSPonse, ERSP) was developed to calculate the electronic response of scintillator materials and provide inputs to the simulations of the energy cascade. The approach developed under this task consists in first calculating the ground state electronic structure of scintillator materials using density functional theory with either the local density approximation or the generalized gradient approximation. The calculated ground state electronic structure is then used as input in ERSP to compute the complex dielectric function, which, in turn, is used to determine the rate of electronic losses of a conduction electron or hole in the energy range up to about 10-20 eV from the band edges. From these calculations, the mean free path of electrons and holes as well as the spectrum of secondary electrons and holes for a given energy and momentum transfer can be determined and used as input for NWEGRIM simulations of electron-hole yield and spatial distribution. This approach allows for modeling the interactions of low-energy particles within scintillator lattices and thus lower the energy cutoff with respect to that used in traditional radiation response codes, thereby enabling us to determine the microscopic structure of ionization tracks.

This approach was applied to four halide scintillators during the course of this project, namely CsI, NaI, BaF₂, and CaF₂. For example, dielectric functions and energy loss functions of CaF₂ and BaF₂ are shown in Fig. 2. The results for CaF₂ show a strong valence plasmon at 17 eV, while for BaF₂ a narrow valence plasmon-like feature at 19.0 eV and a broad plasmon-like resonance between 26 eV and 30 eV are evident. The use of these data to parameterize the distributions of secondary particles in NWEGRIM for plasmon excitations represents an important step to eliminate possible errors caused by the empirical model of plasmon decay typically used.

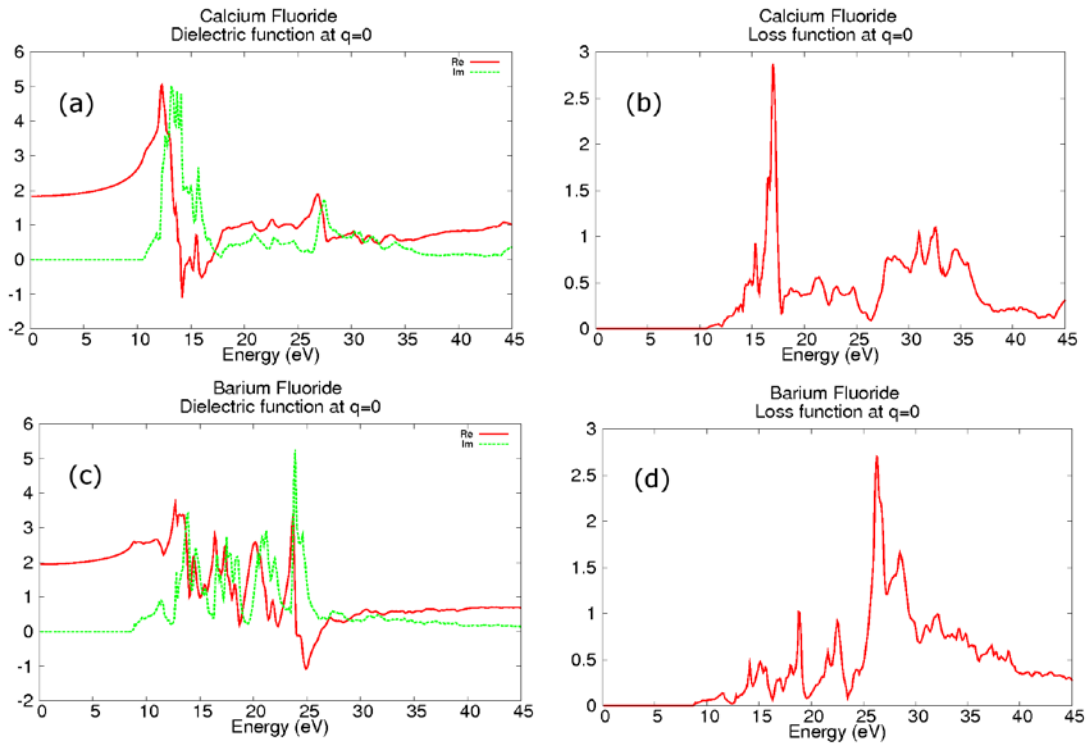


Fig. 2. Dielectric function (a and c) and energy loss function (b and d) of electrons in CaF_2 (top) and BaF_2 (bottom).

For CsI, the predicted electron energy loss reproduces all the peaks observed experimentally at the correct intensities, although our calculations are blue-shifted by about 2 eV compared to experiment. In addition, we predict a high-frequency index of refraction (n_∞) of 1.64 compared to the measured value of 1.74; our predicted bandgap is 5.5 eV compared to experimental measurements of 6.0 to 6.4 eV. The reasonably close agreement of the bandgap is particularly encouraging given that CsI is notorious for having a difficult to compute bandgap. Similar calculations on NaI had similar agreement with n_∞ predicted to be 1.69 compared to a measured 1.73, and a bandgap of 6.1 eV compared to a measured 5.8 to 5.9 eV. Collectively, these results indicate that our approach is validated against experimental data, when available, and thus provides a reliable set of input functions for NWEGRIM calculations.

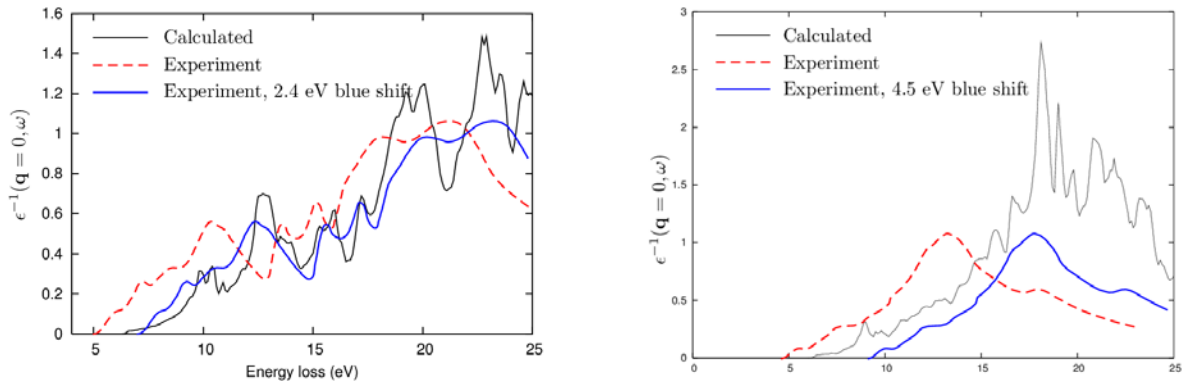


Fig. 3. Calculated and experimental electron energy loss spectra of CsI (left) and NaI (right).

3.0 Task 2: Electron-hole yield, variance and spatial distribution

3.1 Summary of progress

Significant improvements of our computer code for simulating energy cascades (NWEGRIM) were achieved under this project, including the implementation of multiple elastic scattering theory for calculating the spatial distribution of electron-hole pairs and the development of a new approach for determining the stopping power of scintillator materials. Applications to a number of halide scintillators are presented.

3.2 Peer-reviewed publications

F. Gao, Y.L. Xie, S.N. Kerisit, L.W. Campbell, and W.J. Weber *Nuclear Instruments and Methods in Physics Research A* 652 (2011) 564-567

3.3 Progress during project

Multiple elastic scattering theory was implemented in NWEGRIM to allow for simulating the spatial distribution of electron-hole pairs, in addition to the electron-hole pair yield. Cross sections for interband transition, plasmon excitation, and inner-shell ionization at high energies were combined with the low-energy cross sections determined in Task 1 to provide input data sets for NWEGRIM calculations. The yields and spatial distributions of electron-hole pairs were calculated for a range of halide scintillators: CsI, NaI, CaF₂, BaF₂, SrI₂, and LaBr₃. Simulations were carried out for incident photon energies ranging from 50 eV to 1 MeV. Up to 10⁵ photon events were simulated at each energy to ensure convergence of the results. The primary and secondary electrons were followed until their energies were less than twice the bandgap energy.

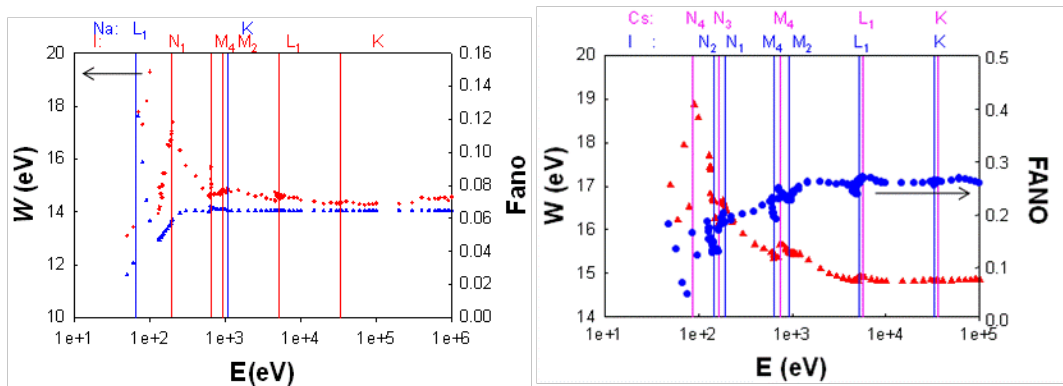


Fig. 4. Mean energy per electron-hole pair, W , and Fano factor, F , as a function of incident photon energy for NaI (left) and CsI (right).

From these simulations, the mean energy per electron-hole pair, W , and the Fano factor (variance of the number of electron-hole pairs produced), F , can be calculated and examples of the variation of these two intrinsic properties with incident photon energy are shown in Fig. 4 for NaI and CsI. Electron-hole

pairs are produced almost exclusively by interband transitions and plasmon excitation in NaI, whereas inner shell ionization, and the corresponding atomic relaxation, also produces a significant number of electron-hole pairs in CsI. The additional channel for electron-hole pair creation gives rise to a larger calculated Fano factor for CsI. Examples of the spatial distributions obtained from these simulations are shown in Fig. 5, again for NaI and CsI. Analysis of electron-hole pair spatial distributions revealed that the track radius near the track end is approximately a few nanometers for CsI and NaI, in good agreement with the values predicted by WFU based on the results of z-scan and K-dip experiments.

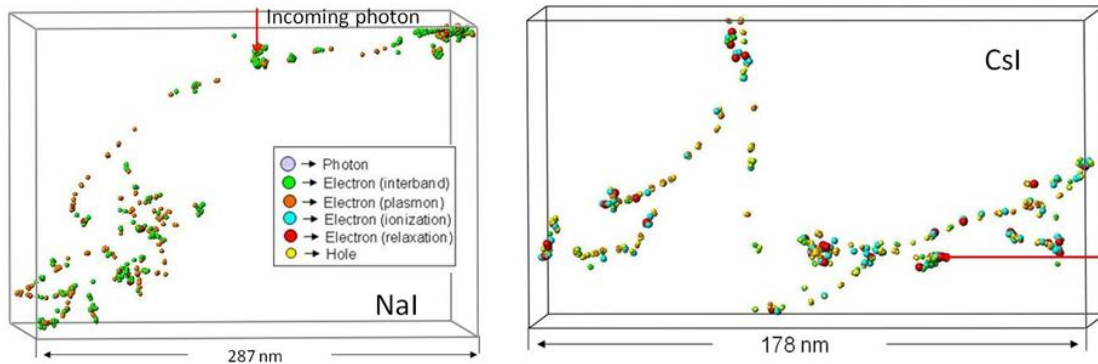


Fig. 5. Calculated spatial distributions of electron-hole pairs for 10-keV photon events in NaI (left) and CsI (right), where electrons and holes are distinguished by size and color, as indicated in the legend.

Other developments included the implementation of an algorithm for calculating the stopping power (dE/dx) and its fluctuations. The approach consists in allowing electrons of a given energy to collide once or twice in a thin film of the material of interest. Calculations were carried out for the halide scintillators listed above. Examples of variations in stopping power as a function of incident electron energy are shown in Fig. 6. The results can be compared to the Bethe-Bloch theory and good agreement is obtained in the energy range 100 eV to 100,000 eV. At higher energies, our calculations agree with the stopping powers calculated with the ESTAR program, provided by NIST, which uses the Bethe-Bloch equation with the density-effect correction of Sternheimer. Our calculations provide values of the stopping power at low energies, where the Bethe-Bloch theory is known to break down. This approach can provide input for the phenomenological and rate-theory-based models of scintillations used by other NA-22-funded researchers, which rely on linear energy deposition (*i.e.* conceptually linear ionization tracks).

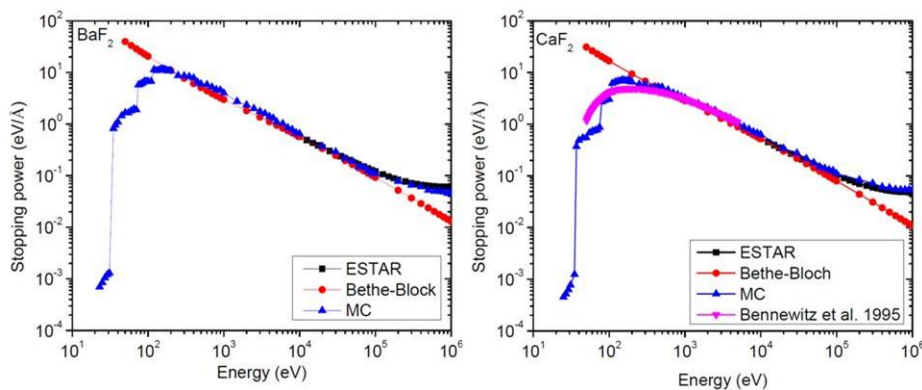


Fig. 6. Stopping power as a function of electron energy in BaF₂ (left) and CaF₂ (right). Also shown are results from the Bethe-Bloch equation and the ESTAR program.

4.0 Task 3: Ab initio calculations of information carrier properties

4.1 Summary of progress

An embedded *ab initio* cluster approach was developed to simulate the formation and mobility of self-trapped excitations in scintillators and applied to NaI. Periodic DFT calculations of intrinsic defects and dopants in CsI were also performed.

4.2 Peer-reviewed publications

M.P. Prange, R.M. Van Ginhoven, N. Govind, and F. Gao *Physical Review B* 87 (2013) 115101

R.M. Van Ginhoven and P.A. Schultz *Journal of Physics: Condensed Matter* 25 (2013) 495504

J. Bang, Z.G. Wang, F. Gao, S. Meng, and S.B. Zhang *Physical Review B* 87 (2013) 205206

4.3 Progress during project

Calculations under this task involved both conventional solid-state (periodic) DFT and embedded *ab initio* cluster (non-periodic) calculations. The latter approach was developed in this project and employs an array of classical charges to simulate the interior of an ionic solid in which the electronic structure of a smaller quantum-mechanical cluster is computed including nonlocal exchange effects. The solid-state DFT approach was employed to characterize the electronic and structural properties of intrinsic defects and Tl and Na dopant centers in CsI, while the embedded cluster approach was used to determine the formation, stability, and mobility of self-trapped excitations in pure and Tl-doped NaI.

4.3.1 Intrinsic defects and Tl and Na dopants in CsI.

A spectrum of intrinsic and dopant defect levels is shown in Fig. 7. These results are useful in determining the properties of defects, and identifying defects that may be involved in carrier and charge trapping in CsI. We find that the Tl and Na centers can accept one or two electrons and couple to long-range relaxations in the surrounding crystal lattice to distort strongly off-center to multiple distinct minima, even without a triplet excitation. The long-range distortions are a mechanism to couple to phonon modes in the crystal, and are expected to play an important role in the phonon-assisted transport of polarons in activated CsI and subsequent light emission in this scintillator.

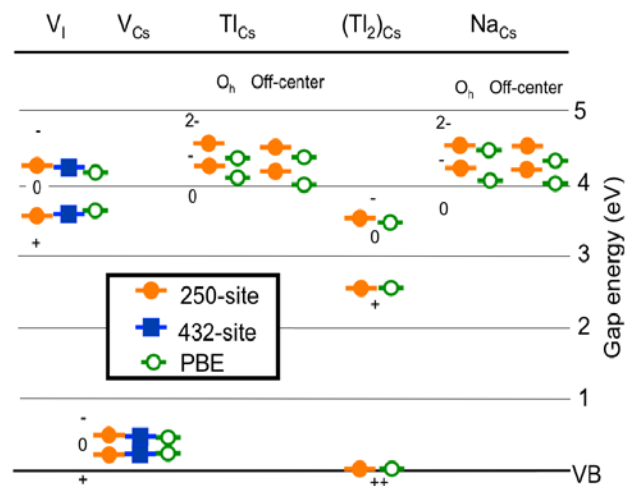


Fig. 7. Defects levels in CsI. LDA and GGA (PBE) are both shown, results are the same within errors of the techniques.

4.3.2 Self-trapped excitations in pure and Tl-doped NaI

We found that on-center self-trapped holes and excitons are stable in NaI compared to delocalized states, but electrons do not self-trapped in our calculations even for pure HF. The calculated emission energy of 4.27 eV for the STE is in good agreement with the experimental value of 4.21 eV. Assuming the conventional picture in which self-trapped excitations migrate via the transfer of lattice distortion and spin density between adjacent sites, we calculated the energy barriers for hopping of the STE and STH for each of the four possible hop angles between iodine neighbor pairs, as shown in Fig. 8.

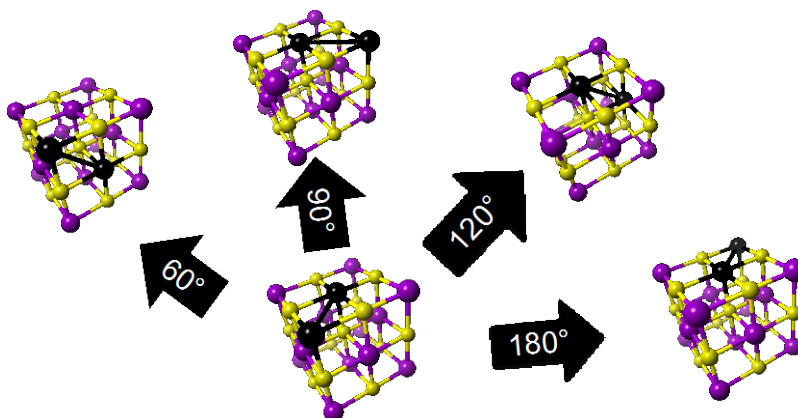


Fig. 8. The four near-neighbor hops available to the STE or STH in NaI.

We show the spin density for the relaxed STH and for the transition state of the 120° hop in Fig. 9. Calculated migration barriers varied between 0.20 and 0.28 eV and were essentially identical for both STE and STH. Therefore, in contrast to what was previously assumed, our calculations show that STEs and STHs are equally mobile in NaI. These migration barriers can be used directly in kinetic Monte Carlo models of scintillation.

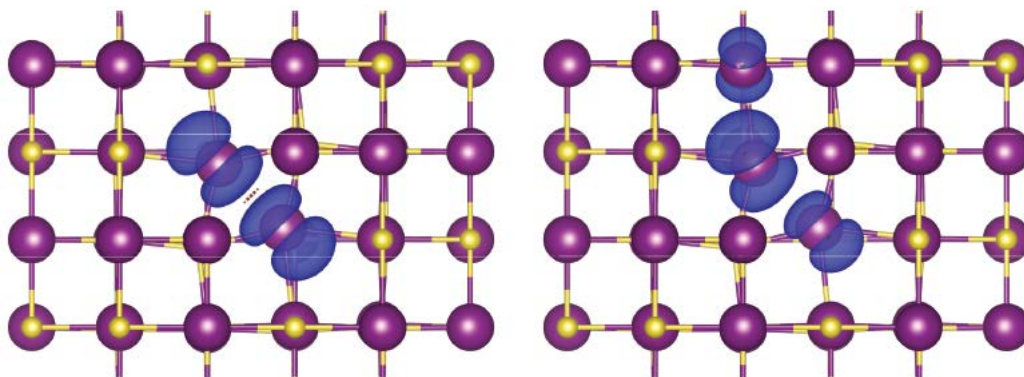


Fig. 9. Spin density isosurfaces drawn at 0.001 electron/bohr³ around an STE (left) and the transition state for a 120° STH jump (right).

Calculations of self-trapped excitations in Tl-doped NaI found two neutral triplet excitons trapped at Tl sites. Both triplet states were calculated to be stable compared to a (bulk) STE near a singlet Tl by ~0.25 eV and hence diffusing STEs are expected to easily trapped when encountering Tl impurities. Again, this result can inform KMC models of scintillation.

5.0 Task 4: Transport of electron-hole pairs and scintillation efficiency

5.1 Summary of progress

A Monte Carlo model of electron thermalization was developed and applied to CsI, NaI, CaF₂, and BaF₂. Our KMC model of scintillation was also extended to allow for simulations of nonlinear quenching processes at high excitation densities similar to those at the track end of ionization tracks.

5.2 Peer-reviewed publications

Z.G. Wang, Y.L. Xie, B.D. Cannon, L.W. Campbell, F. Gao, and S.N. Kerisit *Journal of Applied Physics* 110 (2011) 064903

Z.G. Wang, Y.L. Xie, L.W. Campbell, F. Gao, and S.N. Kerisit *Journal of Applied Physics* 112 (2012) 014906

Z.G. Wang, R.T. Williams, J.Q. Grim, F. Gao, and S.N. Kerisit *Physica Status Solidi B* 250 (2013) 1532-1540

5.3 Progress during project

Two activities were pursued under this task: (1) the development and application of a model of electron thermalization in halide scintillators; and (2) the extension of our KMC model of scintillation to include nonlinear quenching of electron-hole pairs through dipole-dipole Förster transfer.

5.3.1 Electron thermalization in halide scintillators

A Monte Carlo model of electron thermalization in inorganic scintillators was developed under this task and was applied to pure and TI-doped alkali iodides (CsI and NaI) and pure alkaline-earth halides (CaF₂ and BaF₂). This model is based on semi-classical phenomenological models of electron scattering with both optical and acoustic phonons. The electron scattering rates obtained with these models for the four materials of interest are shown in Fig. 10. In addition, the model includes explicit treatment of the effects of internal electric fields on electron trajectories.

For all four pure materials, a large fraction of the electrons rapidly recombine with self-trapped holes. The distances the electrons that avoid recombination (stopped electrons) travel during thermalization show a distribution that peaks between approximately 25 and 50 nm and that can extend to a few hundreds of nanometers, as shown in Fig. 11. The time required for all the electrons to reach thermal energy varies from approximately 0.5 ps for CaF₂ to 7 ps for CsI, as shown in Fig. 12. The LO phonon energy was found to be the major parameter determining the differences in thermalization time and distance between the four pure materials.

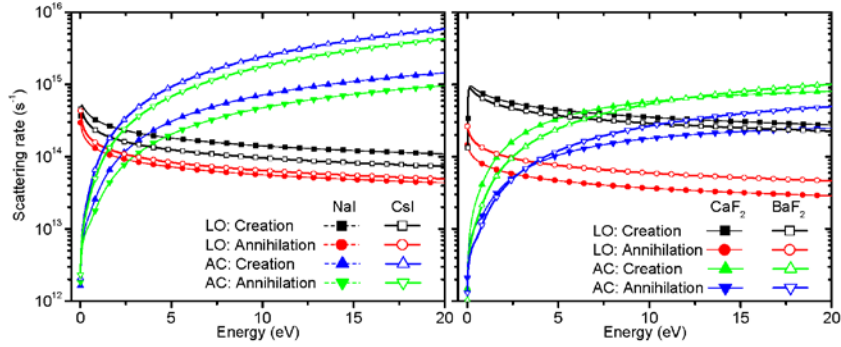


Fig. 10. Electron-phonon scattering rates as a function of electron energy.

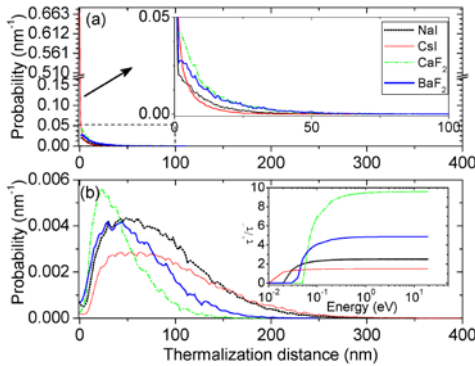


Fig. 11. Distance distributions of the (a) recombined and (b) stopped electrons for a 2-keV incident γ -ray.

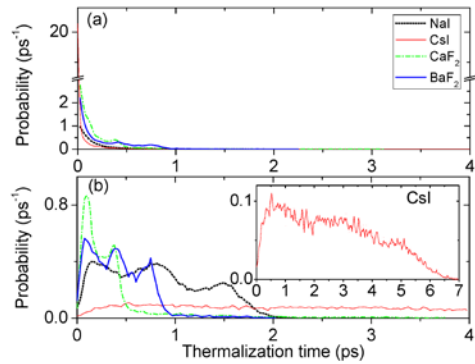


Fig. 12. Time distributions of the (a) recombined and (b) stopped electrons for a 2-keV incident γ -ray.

The effect of doping CsI and NaI with Tl was also investigated whereby electrons can trap at Tl sites as they thermalize. The fraction of Tl-trapped electrons increases with increasing Tl concentration mostly to the detriment of stopped electrons. In addition, the fraction of Tl-trapped electrons shows an asymptotic behavior that reflects the experimentally observed scintillation light output *versus* Tl concentration. The fraction of Tl-trapped electrons increases with increasing incident energy to the detriment of the fraction of recombined electrons, which is consistent with experimental observation of the decrease of the light component corresponding to prompt exciton capture at Tl sites.

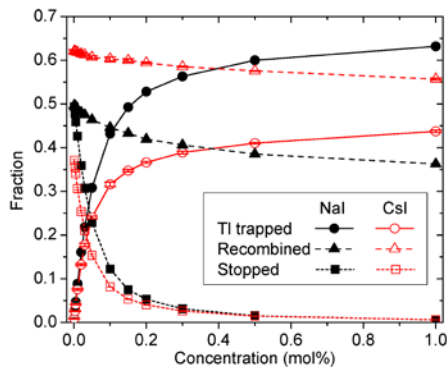


Fig. 13. Fraction of Tl-trapped electrons and recombined electron-hole pairs as a function of Tl concentration for an incident γ -ray energy of 2 keV

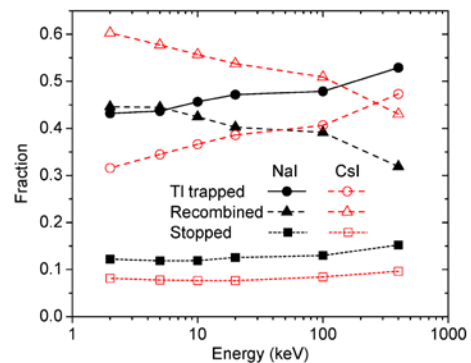


Fig. 14. Fraction of Tl-trapped, stopped and recombined electrons as a function of incident γ -ray energy for a Tl concentration of 0.1 mol%.

5.3.2 Nonlinear quenching of electron-hole pairs (STE-STE annihilation)

A KMC model of scintillation mechanisms developed for simulating the kinetics and efficiency of scintillation of γ -ray irradiated CsI was modified to extend its applicability to high excitation densities. A schematic of the processes considered in the model is shown in Fig. 15. Specifically, a distance-dependent dipole-dipole Förster transfer process (STE-STE annihilation) was added to the KMC model. This process is active in high-density regions of ionization tracks and is believed to be responsible for the nonproportional response of scintillators at low incident energies. Recent experimental data on the excitation density dependence of scintillation light yields obtained under UV excitation by our collaborators at WFU offered an unprecedented opportunity to parameterize this process for CsI. Excellent agreement with the experimentally-derived second-order component was obtained within the framework of the existing KMC scintillation model (Fig. 16).

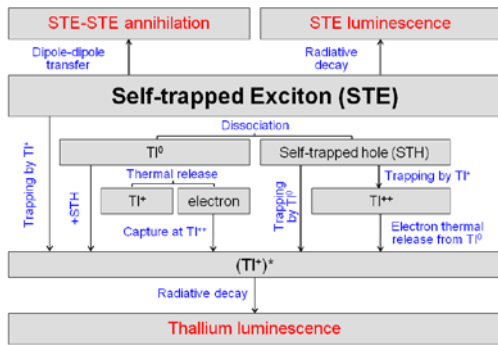


Fig. 15. Schematic of the elementary species (black), elementary processes (blue), and possible final outcomes (red) considered in the KMC model of scintillation

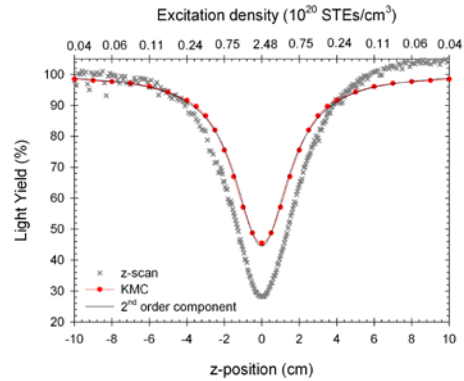


Fig. 16. Calculated light yield as a function of z-position and excitation density and comparison with the z-scan data and second-order component determined by WFU.

Using the same set of parameters, good agreement was also obtained with the kinetics of scintillation of TI-doped CsI (Fig. 17) and pure CsI (Fig. 18). In particular, good agreement was obtained for the rising time of the $(\text{TI}^+)^*$ emission Fig. 17 once STHs and STEs were set to be equally mobile based on the information obtained in Task 3. Such microscopic models of scintillation mechanisms can be used in combination with γ -ray induced ionization tracks calculated by NWEGRIM to investigate the nonproportional response of CsI and other scintillators.

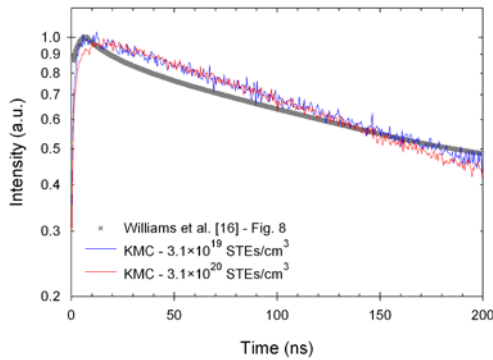


Fig. 17. Decay curves of the $(\text{TI}^+)^*$ emission of CsI:0.3%TI calculated at two excitation densities and comparison with the WFU experimental results.

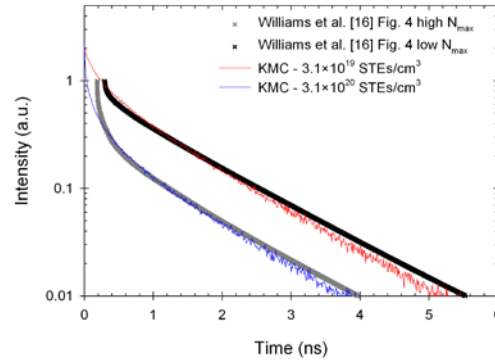
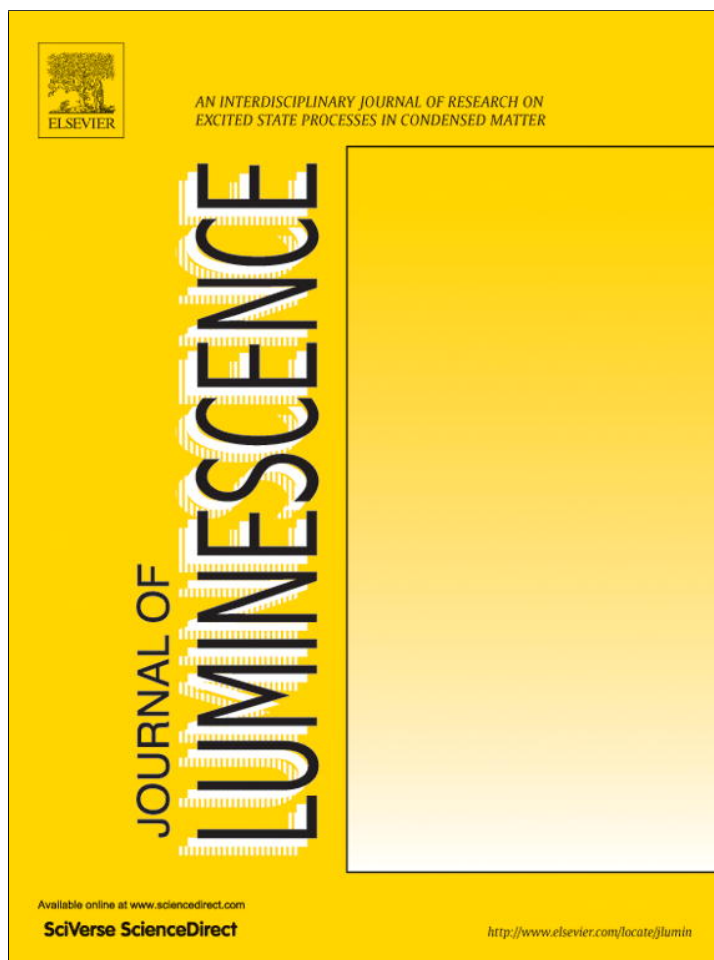


Fig. 18. Decay curves of the STE emission of pure CsI calculated at two excitation densities and comparison with the WFU experimental data.

Appendix A

Peer-Reviewed Publications

Provided for non-commercial research and education use.
Not for reproduction, distribution or commercial use.



(This is a sample cover image for this issue. The actual cover is not yet available at this time.)

This article appeared in a journal published by Elsevier. The attached copy is furnished to the author for internal non-commercial research and education use, including for instruction at the authors institution and sharing with colleagues.

Other uses, including reproduction and distribution, or selling or licensing copies, or posting to personal, institutional or third party websites are prohibited.

In most cases authors are permitted to post their version of the article (e.g. in Word or Tex form) to their personal website or institutional repository. Authors requiring further information regarding Elsevier's archiving and manuscript policies are encouraged to visit:

<http://www.elsevier.com/copyright>



Excited state electronic properties of sodium iodide and cesium iodide

L.W. Campbell*, F. Gao

Pacific Northwest National Laboratory, 3335 Q Avenue Mail Stop J4-80, Richland, WA 99354, United States

ARTICLE INFO

Article history:

Received 11 September 2012

Received in revised form

22 December 2012

Accepted 28 December 2012

Available online 4 January 2013

Keywords:

Electronic screening

Electronic lifetime

Electron cascade

Plasmon decay

Sodium iodide

Cesium iodide

ABSTRACT

We compute from first principles the dielectric function, loss function, lifetime and scattering rate of quasiparticles due to electronic losses, and secondary particle spectrum due to plasmon decay in two scintillating alkali halides, sodium iodide and cesium iodide. Particular emphasis is placed on quasiparticles within several multiples of the bandgap from the band edges. A theory for the decay spectra of plasmons and other electronic excitations in crystals is presented. Applications to Monte Carlo radiation transport codes are discussed.

© 2013 Published by Elsevier B.V.

1. Introduction

Predicting the response of a material to the passage of charged particle radiation is a challenging computational problem, particularly at low energies where the electronic structure cannot be treated as an electron gas. At a basic level, the physics is well known. We start with a high energy electron present in the material; perhaps one liberated from a core or valence state by an x-ray or gamma photon through photoelectric absorption or Compton scattering, perhaps created by radioactive decay or gamma ray induced pair production, or perhaps introduced by a beam or external high energy physics event. As the electron traverses the material, the Coulomb field of the charged projectile excites further electronic excitations. This will result in a partial transfer of the primary electron's energy and momentum to the excitation, resulting in the excitation of a core or valence electron to a conduction band. The resulting conduction electron may also be highly energetic, capable of creating additional electronic excitations. The hole may be produced in a highly excited state, whose atomic relaxation creates further electron-hole pairs through the Auger process. For electrons in the lower conduction band and valence holes, energy losses to phonons compete with electronic processes and become dominant close to the threshold for electronic excitation. The electronic cascade stops when no individual electron or hole has enough energy to excite a valence electron across the bandgap, thus preventing further electronic

processes in the cascade. The end result is that the original energy of the initial charged particle has become distributed among a number of hot conduction electrons and valence holes. In semiconductor detectors, these charge carriers are the measured signal, creating a current pulse which is picked up with attached electronic instrumentation. In scintillator materials, the process leading to the signal continues—charge carriers will continue to lose energy to phonons until they become thermalized, and then either recombine to produce optical photons that are picked up with photodetectors, or are trapped or recombine non-radiatively and do not contribute to the measured signal. An accurate understanding of the electronic cascade process will be useful for the design of radiation detectors, the search for new detector materials, and the interpretation of the signals of such detectors.

Available codes dealing with this subject typically look at tracks rather than microscopic response [1,2]. While high energy knock-off electrons are tracked, those secondary particles whose energy is below a cutoff threshold are not explicitly followed and their effects accounted for in an average way. In this approximation, the low energy excitations simply provide a “stopping power” or continuous energy loss per unit distance by which the primary electron travels. This involves knowing the parameters that give rise to the stopping power in each material, and does not allow computational studies of such issues as the average signal or its variance from first principles. While a number of attempts have been made to extend the scope of the simulation to consider each electronic excitation, such simulations to date rely on electron-gas like approximations [3–5] or free atom approximations [6,7] that lead to questionable values when the electron energy falls low enough for band structure

* Corresponding author.

E-mail address: luke.campbell@pnl.gov (L.W. Campbell).

effects to significantly affect its dispersion. Since it is just this low energy response that determines when the electron cascade will end, it is important to include a more realistic model of the low energy electronic behavior.

The response to a charged particle is ultimately a problem involving the basic methods of predicting electronic excited states and response functions, where the particle of radiation is treated as a quasiparticle excitation in the medium. Calculations of the electronic response have long been used to predict such quantities as the dielectric function, optical absorption spectrum, and electron energy loss spectrum (EELS) [8–12]. The rate of excitations produced by a perturbing field (such as the Coulomb field of the radiation particle) is found using the imaginary part of the dielectric screening of the material. Summing up all such excitations that are allowed by relevant conservation laws gives the total rate at which the perturbation produces excitations, corresponding to the rate at which the radiation particle scatters out of its current state to a state of lower energy. Experimentally measured optical absorption or electron energy loss spectra, with assumed free-electron energy dispersion relations and plane wave electrons propagating in the solid, have been used to calculate inelastic mean free paths and stopping powers of electrons in alkali halides using summations of this type [13]. When the dielectric function is calculated in the random phase approximation (RPA) and corrected by the distribution of the electron wave function in the material, these summations are equivalent to finding the imaginary part of the self-energy in Hedin's *GW* approximation [14] (not an acronym, the *G* stands for Green's function operator, and *W* is the screened Coulomb interaction operator). This *GW* approximation is widely used to reproduce excited state quasiparticle properties, and has been employed to calculate the electronic lifetime of hot electrons in the metals Cu and Al [15], the imaginary self-energy [16] and electronic response including electronic lifetime [17] of hot electrons and holes in the semiconductor silicon, and the inelastic mean free path and stopping power of electrons up to 10 MeV in Au, Ag, and Cu [18]. Carrying out electron lifetime calculations in the *GW* approximation with a full RPA dielectric function allows to avoid extrapolating the zero wave vector loss function, and thus avoid simplistic approximations of the loss function dispersion. In this way, realistic behavior for the prominent plasmon-like excitations can be included while simultaneously allowing for correct limiting behavior at high and low wave vectors.

In order to understand the scintillation process from first principles, we chose to start with two common scintillating radiation detector materials, sodium iodide and cesium iodide, and investigate the screening, average lifetime of excited electron states, and the spectrum of secondary particles produced by plasmon excitations within the RPA and *GW* approximations. The lifetime is closely related to such quantities of interest as the mean free path, stopping power, and valence excitation cross sections. These quantities, and the secondary particle spectra of plasmon decay, served as input into the Monte Carlo code NorthWest Electron and Gamma Ray Interaction in Matter (NWEGRIM) in order to predict the signals from beta and gamma radiation and associated track nanostructure [4,5]. Because core-level excitations and atomic relaxation depend almost entirely on the element of the atom involved in the excitation [19], and because the core level excitations and decay modes are well tabulated [20], these processes can already be handled accurately by standard Monte Carlo radiation transport techniques. We thus concentrate on excitations of the valence electrons, which are difficult to handle in a simple fashion since they are strongly affected by the electronic structure of the material under consideration. While the NWEGRIM results on NaI and CsI have previously been reported [21,22], this is the first description of

the *ab initio* electronic structure calculations used in those studies. NWEGRIM outputs a spatial distribution of conduction electrons and holes whose energies have fallen below the threshold for exciting further valence to conduction band transitions. This distribution is passed as input to further simulations that investigate the diffusion of the hot charge carriers until thermalization and trapping [22], which in turn is input into a kinetic Monte Carlo simulation for the diffusion and ultimate recombination of the charge carriers to produce the final signal in the form of light [23,24].

2. Theory

In this section, and elsewhere in this paper, we work exclusively in atomic units ($e = \hbar = m_e = 1$) unless otherwise noted. We will cover the basic theory of electronic screening, the rate at which electrons suffer losses while traversing the material, and the spectrum of secondary particles produced during these losses.

2.1. Screening

In semiconductors and insulators the longitudinal dielectric function in the limit of the Random Phase Approximation (RPA) takes the form [25,26]

$$z.\text{epsi}_{\mathbf{k},\mathbf{k}'}^{-1}(\mathbf{q},\omega) = \delta_{\mathbf{k},\mathbf{k}'} - \frac{4\pi}{|\mathbf{q}+\mathbf{K}||\mathbf{q}+\mathbf{K}'|} \sum_c^{\text{unocc}} \sum_v^{\text{occ}} \int_{\text{B.Z.}} \frac{d^3k}{(2\pi)^3} \times \left[\frac{\rho_{cv}(\mathbf{k},\mathbf{q}+\mathbf{K})\rho_{vc}^*(\mathbf{k},\mathbf{q}+\mathbf{K}')}{\omega - z.\text{epsiv}_{vc}(\mathbf{k}) + z.\text{epsiv}_{v'}(\mathbf{k}-\mathbf{q}) + i\eta} - \frac{\rho_{vc}(\mathbf{k},\mathbf{q}+\mathbf{K})\rho_{vc}^*(\mathbf{k},\mathbf{q}+\mathbf{K}')}{\omega + z.\text{epsiv}_{vc}(\mathbf{k}) - z.\text{epsiv}_{v'}(\mathbf{k}-\mathbf{q}) + i\eta} \right], \quad (1)$$

where the notation unocc restricts the sum to unoccupied bands and occ to occupied bands, B.Z. indicates the integral is to be taken over the first Brillouin zone, the wave vector \mathbf{q} is restricted to the first Brillouin zone, \mathbf{K} and \mathbf{K}' are reciprocal lattice vectors, and the notation for the density matrix elements reflects the fact that a density operator of wave vector \mathbf{q} can only connect Bloch waves $\psi_{n,\mathbf{k}}(\mathbf{r})$ with wave vectors differing by \mathbf{q}

$$\rho_{nn'}(\mathbf{k},\mathbf{q}+\mathbf{K}) = \int d^3r \psi_{n,\mathbf{k}}(\mathbf{r})\psi_{n',\mathbf{k}-\mathbf{q}}^*(\mathbf{r})e^{-i(\mathbf{q}+\mathbf{K})\cdot\mathbf{r}}. \quad (2)$$

This is a form which can be conveniently calculated using modern electronic structure codes. Once sufficient matrix elements in the reciprocal lattice vector space have been found to adequately express the response, the inverse longitudinal dielectric function $z.\text{epsi}_{\mathbf{k},\mathbf{k}'}^{-1}(\mathbf{q},\omega)$ is found as a matrix inverse.

The RPA does not include interactions between the conduction electrons and holes, and thus cannot reproduce excitons. Excitons are fundamental to the process of scintillation, they are vital to the process of transport of the thermalized charge carriers in a scintillator, and the decay of excitons can produce scintillation light (although in NaI and CsI, most of the light yield comes from thallium activator dopants). However, experimentally the oscillator strength of excitons is small, so that although they produce well-defined peaks they are expected to be a relatively minor perturbation to the overall process of the creation of charge carriers in the crystal and the decay of multi-eV collective excitations. The fine structure from effects beyond the RPA is likely to be washed out during the integration process leading to the total quasiparticle lifetime and thus effects on the lifetime are likely to be small. Conduction electron–hole interactions are known to shift the location of plasmon resonances by a couple of eV in semiconductors [27], although their effect in alkali halide collective excitations is unknown. This could potentially change the plasmon decay spectrum by creating the bulk of the

excitations at a different energy than what is calculated. This effect is a subject for future research.

2.2. Rate of loss

We take the initial state of our system $|\Psi_I\rangle$ as the ground state $|\Psi_0\rangle$ of an N electron system except for a single additional electron in a conduction band n with wave vector \mathbf{k} that represents the radiation particle traversing the crystal,

$$|\Psi_I\rangle = a_{n,\mathbf{k}}^\dagger |\Psi_0\rangle \quad (3)$$

and the final state $|\Psi_\alpha\rangle$ as a series of particle–hole excitations of the N particle system $|\Psi_{ph}\rangle$ of total energy ω_{ph} with an additional electron in conduction band n' and wave vector \mathbf{k}' representing the scattered radiation particle,

$$|\Psi_\alpha\rangle = a_{n',\mathbf{k}'}^\dagger |\Psi_{ph}\rangle. \quad (4)$$

The rate at which the radiation particle transfers energy to electronic excitations of the initial state I of the material is given by Fermi's golden rule [28]

$$\Gamma_I = 2\pi \sum_\alpha |\langle \Psi_\alpha | H_{\text{int}} | \Psi_I \rangle|^2 \delta(\omega_{\alpha I}), \quad (5)$$

where $\omega_{\alpha I}$ is the energy difference between the state α and state I . The interaction Hamiltonian can be taken as the Coulomb interaction between the charge density of the radiation electron and the material

$$H_{\text{int}} = \sum_{\mathbf{K}} \int_{\text{B.Z.}} \frac{d^3q}{(2\pi)^3} \frac{4\pi}{q^2} \rho_r(-\mathbf{q}-\mathbf{K}) \rho(\mathbf{q}+\mathbf{K}), \quad (6)$$

where $\rho(\mathbf{q})$ is the charge density operator for the electrons of the material and $\rho_r(\mathbf{q})$ is the charge density operator for the radiation electron

$$\rho_r(\mathbf{q}) = \sum_{n,n'} \int_{\text{B.Z.}} \frac{d^3k}{(2\pi)^3} a_{n',\mathbf{k}-\mathbf{q}}^\dagger a_{n,\mathbf{k}} \rho_{nn'}(\mathbf{k},\mathbf{q}). \quad (7)$$

Neglecting exchange terms between these two density operators and generalizing to also allow the case where the radiation particle is a hole, we obtain

$$\begin{aligned} \Gamma_n(\mathbf{k}) &= 2\pi \sum_{n'} \sum_{\mathbf{K}\mathbf{K}'} \int_{\text{B.Z.}} \frac{d^3q}{(2\pi)^3} \frac{4\pi}{|\mathbf{q}+\mathbf{K}|^2} \frac{4\pi}{|\mathbf{q}+\mathbf{K}'|^2} \\ &\quad \times \rho_{nn'}(\mathbf{k},\mathbf{q}+\mathbf{K}) \rho_{nn'}^*(\mathbf{k},\mathbf{q}+\mathbf{K}') \\ &\quad \times \sum_{ph} \langle \Psi_{ph} | \rho(\mathbf{q}+\mathbf{K}) | \Psi_0 \rangle \langle \Psi_0 | \rho^\dagger(\mathbf{q}+\mathbf{K}') | \Psi_{ph} \rangle \\ &\quad \times \delta(\omega(1-2f_n) - z.\text{epsiv}_{;n}(\mathbf{k}) + z.\text{epsiv}_{;n'}(\mathbf{k}-\mathbf{q})), \end{aligned} \quad (8)$$

where f_n is the occupation function for band n (for metals, or finite temperatures, we would need to consider occupation as a function of wave number as well. In the case of materials with a bandgap, where the bandgap energy is much larger than the temperature, this functional dependence on \mathbf{k} can be suppressed).

The inverse dielectric function can be expressed in terms of density matrix elements of the exact many particle states [29,30]

$$\begin{aligned} z.\text{epsiv}_{;\mathbf{K}\mathbf{K}'}^{-1}(\mathbf{q},\omega) - \delta_{\mathbf{K}\mathbf{K}'} &= \frac{4\pi}{|\mathbf{q}+\mathbf{K}||\mathbf{q}+\mathbf{K}'|} \\ &\quad \times \sum_n \left[\frac{\langle \Psi_0 | \rho(\mathbf{q}+\mathbf{K}) | \Psi_n \rangle \langle \Psi_n | \rho^\dagger(\mathbf{q}+\mathbf{K}') | \Psi_0 \rangle}{\omega - (E_n - E_0) + i\eta} \right. \\ &\quad \left. - \frac{\langle \Psi_0 | \rho^\dagger(\mathbf{q}+\mathbf{K}') | \Psi_n \rangle \langle \Psi_n | \rho(\mathbf{q}+\mathbf{K}) | \Psi_0 \rangle}{\omega + (E_n - E_0) + i\eta} \right]. \end{aligned} \quad (9)$$

If we define W as the screened Coulomb interaction

$$W_{\mathbf{K}\mathbf{K}'}(\mathbf{q},\omega) = \frac{4\pi}{|\mathbf{q}+\mathbf{K}||\mathbf{q}+\mathbf{K}'|} z.\text{epsiv}_{;\mathbf{K}\mathbf{K}'}^{-1}(\mathbf{q},\omega), \quad (10)$$

then using Eq. (9) the rate of loss for an electron in a crystal becomes

$$\begin{aligned} \Gamma_n(\mathbf{k}) &= 2i \sum_{n'} \int_0^\infty d\omega \int_{\text{B.Z.}} \frac{d^3q}{(2\pi)^3} \sum_{\mathbf{K}\mathbf{K}'} \\ &\quad \times \rho_{nn'}(\mathbf{k},\mathbf{q}+\mathbf{K}) \rho_{nn'}^*(\mathbf{k},\mathbf{q}+\mathbf{K}') W_{\mathbf{K}\mathbf{K}'}^{(A)}(\mathbf{q},\omega) \\ &\quad \times \delta(\omega(1-2f_n) - z.\text{epsiv}_{;n}(\mathbf{k}) + z.\text{epsiv}_{;n'}(\mathbf{k}-\mathbf{q})), \end{aligned} \quad (11)$$

where $W_{\mathbf{K}\mathbf{K}'}^{(A)} = (W_{\mathbf{K}\mathbf{K}'} - W_{\mathbf{K}\mathbf{K}'}^\dagger)/2$ is the anti-Hermitian part of W .

With a few simple transformations, this result can be related to other well known quantities. The one electron Green's function in energy space can be written as [30]

$$G(\mathbf{r},\mathbf{r}',E) = \sum_n \int_{\text{B.Z.}} \frac{d^3k}{(2\pi)^3} \frac{\psi_{n,\mathbf{k}}(\mathbf{r}) \psi_{n,\mathbf{k}}^*(\mathbf{r}')}{E - z.\text{epsiv}_{;n}(\mathbf{k}) + i\eta(1-2f_n)}. \quad (12)$$

With this expression, the popular GW expression for the self-energy [14]

$$\Sigma(\mathbf{r},\mathbf{r}',E) = i \int \frac{d\omega}{2\pi} G(\mathbf{r},\mathbf{r}',E-\omega) W(\mathbf{r},\mathbf{r}',\omega) \quad (13)$$

has diagonal orbital matrix elements given by

$$\begin{aligned} \langle n,\mathbf{k} | \Sigma(E) | n,\mathbf{k} \rangle &= i \int \frac{d\omega}{2\pi} \sum_{n'} \int_{\text{B.Z.}} \frac{d^3q}{(2\pi)^3} \sum_{\mathbf{K}\mathbf{K}'} W_{\mathbf{K}\mathbf{K}'}(\mathbf{q},\omega) \\ &\quad \times \frac{\rho_{nn'}(\mathbf{k},\mathbf{q}+\mathbf{K}) \rho_{nn'}^*(\mathbf{k},\mathbf{q}+\mathbf{K}')}{E - \omega - z.\text{epsiv}_{;n'}(\mathbf{k}-\mathbf{q}) + i\eta(1-2f_{n'})}. \end{aligned} \quad (14)$$

The screened interaction can be expressed in spectral form

$$\begin{aligned} W_{\mathbf{K}\mathbf{K}'}(\mathbf{q},\omega) &= \frac{4\pi}{|\mathbf{q}+\mathbf{K}|^2} \delta_{\mathbf{K}\mathbf{K}'} \\ &\quad + \frac{i}{\pi} \int_0^\infty d\omega' \left[\frac{1}{\omega - (\omega' - i\eta)} - \frac{1}{\omega + (\omega' - i\eta)} \right] W_{\mathbf{K}\mathbf{K}'}^{(A)}(\mathbf{q},\omega'). \end{aligned} \quad (15)$$

Inserting this spectral representation in Eq. (14), we see that

$$\Gamma_n(\mathbf{k}) = 2 |\text{Im} \langle n,\mathbf{k} | \Sigma(z.\text{epsiv}_{;n}(\mathbf{k})) | n,\mathbf{k} \rangle|. \quad (16)$$

A significant body of work exists on calculating the self-energy in the GW approximation [31]. Reducing our expression to this method thus allows us to take advantage of this published experience in this study.

2.3. Secondary particle spectra

Eq. (11) shows that the energy loss of charged particles is due to a suitably weighted sum over electronic excitations of all energy transfers ω and momentum transfers \mathbf{q} from the particle to the medium. The function inside the integrand is thus the (un-normalized) excitation spectrum. The inverse dielectric function is seen to have a central importance in determining the weights of the excitations, and Eq. (1) shows how this function is composed of individual particle–hole excitations from valence bands ν and wave vectors $\mathbf{k}-\mathbf{q}$ to conduction bands c and wave vectors \mathbf{k} . Thus, we can similarly expect to decompose any electronic excitation into a spectrum of secondary conduction electrons and holes that result from the decay of the excitation with the specified energy and momentum transfer.

A primary motivation for this decomposition comes from collective resonances where the dielectric screening nearly vanishes, thus amplifying the perturbing field over large distances and providing a strong channel for losses. These resonances, called plasmons, are common in condensed media and are a major player in electronic losses. The mechanisms described in the previous subsections are well known and describe the influence of the plasmons (among other excitations) on losses, but the subsequent decay of the plasmon excitations has not been well studied. Chung and Everhart [32] have

previously developed a theory for plasmon decay in nearly free electron metals. Here, we extend the theory to crystalline semiconductors and insulators and apply it not just to plasmons but to any electronic excitation.

A rigorous derivation of the form of the secondary particle spectra is provided in Appendix A. We find that the unnormalized spectrum for the promotion of a valence electron from band v and wave vector $\mathbf{k}-\mathbf{q}$ to a conduction band c with wave vector \mathbf{k} by an excitation with energy transfer ω and momentum transfer \mathbf{q} for reciprocal lattice vector contributions \mathbf{K}, \mathbf{K}' is given by the partial loss function $L_{cv;\mathbf{K}\mathbf{K}'}(\mathbf{k}; \mathbf{q}, \omega)$, as defined in Eq. (A.12). Secondary particle spectra are taken by forming suitable sums and integrals over $L_{cv;\mathbf{K}\mathbf{K}'}(\mathbf{k}; \mathbf{q}, \omega)$. The unnormalized energy spectrum of the secondary conduction electrons, for example, is given by

$$L_{\mathbf{K}\mathbf{K}'}(E; \mathbf{q}, \omega) = \sum_c \sum_v^{\text{unocc}} \int_{\text{B.Z.}} \frac{d^3k}{(2\pi)^3} \delta(E - z.\text{epsiv}_c(\mathbf{k})) L_{cv;\mathbf{K}\mathbf{K}'}(\mathbf{k}; \mathbf{q}, \omega). \quad (17)$$

If local fields are neglected, the inverse dielectric functions become diagonal and, up to a normalization constant,

$$L_{cv}(\mathbf{k}; \mathbf{q}, \omega) \propto |\rho_{cv}(\mathbf{k}, \mathbf{q})|^2 \delta(\omega - z.\text{epsiv}_c(\mathbf{k}) + z.\text{epsiv}_v(\mathbf{k}-\mathbf{q})), \quad (18)$$

where \mathbf{q} is now allowed to extend beyond the first Brillouin zone. This approximation has the advantage that the inverse dielectric function does not need to be pre-computed prior to evaluation of the normalized secondary particle spectrum.

3. Methods

To obtain the initial orbitals for our calculation, we used the ABINIT electronic structure code [33–35]. ABINIT uses a plane wave basis set to perform density functional theory (DFT) [36] computations on periodic crystals. A lattice parameter of 4.57 Å was chosen for CsI [37–39] and 6.46 Å for NaI [37]. The wave function was found in the local density approximation (LDA) on two separate primary and secondary \mathbf{k} -point grids, each a $10 \times 10 \times 10$ grid in the first Brillouin zone. The primary \mathbf{k} -point grid is a Γ point centered grid, while the secondary grid is shifted by $0.001 \mathbf{b}_1 + 0.0005 \mathbf{b}_2$ from the primary grid where \mathbf{b}_1 , \mathbf{b}_2 , and \mathbf{b}_3 are the primitive reciprocal lattice vectors of the crystal. This shift was chosen so that the offset between grids gives a wave vector \mathbf{q} adequate to reproduce the limit $\mathbf{q} \rightarrow 0$ for which later calculations of the electronic response are sufficiently converged while still large enough to avoid numerical errors due to finding a small difference in close quantities. A converged electronic structure was obtained with a plane wave cutoff energy of 20 hartree. Troullier Martins pseudopotentials [40] were used. Cs was represented by the 6s valence and 5p semi-core electrons, Na by the 3s valence electron, and I by the 5s and 5p valence electrons. All more tightly bound electrons were considered non-interacting core electrons and handled through their effects on the pseudopotentials.

No electronic excitations are possible for quasiparticles with energies less than the bandgap from the band edge—the quasiparticle must give up at least one bandgap's worth of energy to promote a valence electron to the conduction band, and it must itself have an unoccupied orbital of the required energy into which it can decay. DFT methods are notorious for underestimating the bandgap. Using the Kohn–Sham energy eigenvalues [36] directly in Eq. (1) would have led to quasiparticles exciting losses at energies lower than what is physically possible. Our LDA ground state electronic structure results give bandgaps which are too small by a factor of around two, as indicated in Table 1. To

Table 1

Energies of selected transitions between the highest valence band and lowest conduction band. Column GW(1) lists ABINIT calculated GW bandgaps which were used for orbital energies in our calculations, GW(2) lists self-energies calculated using methods described in this work. Experimental values for NaI taken from [47–49]; values for CsI from [47,48,50,51].

Material	Transition	Bandgap (eV)			
		LDA	GW (1)	GW (2)	Experiment
NaI	$\Gamma \rightarrow \Gamma$	3.41	5.14	6.07	5.9, 5.8, 5.75
CsI	$\Gamma \rightarrow \Gamma$	3.15	4.78	5.49	6.1, 6.3, 6.37, 6.0
CsI	$M \rightarrow \Gamma$	3.08	4.74	5.44	

correct for this, we adjust the band energies with a GW calculation, using the native ABINIT capabilities. A plasmon pole screening matrix found with 30 bands, a wave function cutoff of 4 hartree, and a dielectric matrix cutoff of 3.6 hartree, plus a self-energy calculation with 50 bands, a cutoff energy of 10 hartree, and an exchange cutoff energy of 6 hartree was sufficient to converge the calculation to within 0.004 eV. For the purpose of simulating ionization losses of radiation particles, an accurate estimate of the bandgap is crucial since the amount of ionization per incident energy is strongly bandgap dependent. Because of a significant discrepancy remaining between the GW-calculated bandgap and the range of experimental bandgaps, we further increased the bandgap using a scissors operator [41,42] to bring our estimates of ionization more closely in line with what would be expected of the actual material. Conduction band energies of CsI were increased uniformly by 1.5 eV, those of NaI by 0.75 eV. This enforces an optical bandgap of 6.28 eV for CsI and 5.89 eV for NaI.

The density matrix elements $\rho_{nm}(\mathbf{k}, \mathbf{q} + \mathbf{K})$ are evaluated using the Kohn–Sham orbitals. The self-energy operator has been shown to be very nearly diagonal in this basis set [43], implying that the orbitals with many body effects included are very similar to those found in DFT calculations.

The anti-Hermitian part of the dielectric matrix of Eq. (1) is given in Eq. (A.10). This is evaluated on the primary \mathbf{k} point grid for finite \mathbf{q} via the tetrahedron method [44], which finds the contribution from the constant energy surfaces of the delta function over the entire integration volume. The Hermitian components can then be obtained through

$$z.\text{epsi}_{\mathbf{K}\mathbf{K}'}^{(H)}(\mathbf{q}, \omega) = \delta_{\mathbf{K}\mathbf{K}'} + \frac{2}{\pi} \mathcal{P} \int_0^\infty d\omega' z.\text{epsi}_{\mathbf{K}\mathbf{K}'}^{(A)}(\mathbf{q}, \omega') \frac{\omega'}{\omega'^2 - \omega^2},$$

where \mathcal{P} indicates the principal part of the integral. This method has the attractive feature that electronic losses become strictly zero for energy transfers ω below the lowest possible transition energy, preventing the bleed-over into the bandgap which occur when using broadened sums over the calculated \mathbf{k} -points. However, it should be remembered that our calculations were carried out at the RPA level of theory, and thus will miss the excitonic losses that occur at less than the bandgap energy.

At $\mathbf{q} = 0$ the Coulomb potential has a singularity when one or both of the reciprocal lattice vectors \mathbf{K}, \mathbf{K}' equal to zero. However, in the limit $\mathbf{q} \rightarrow 0$ the quantity

$$\frac{4\pi}{|\mathbf{q} + \mathbf{K}| |\mathbf{q} + \mathbf{K}'|^2} \rho_{nm}(\mathbf{k}, \mathbf{q} + \mathbf{K}) \rho_{nm}^*(\mathbf{k}, \mathbf{q} + \mathbf{K}') \quad (19)$$

is well defined in cubic materials for non-degenerate (and non-equal) bands n and n' for all \mathbf{K}, \mathbf{K}' because of the orthogonality of the bands. As such, the actual function integrated in the dielectric function expression is well behaved. We determine $z.\text{epsi}_{\mathbf{K}\mathbf{K}'}^{(A)}(\mathbf{q} \rightarrow 0, \omega)$ by calculating the low wave vector density matrix elements for the small but finite \mathbf{q} between the primary and secondary \mathbf{k} point grids.

The loss is found using Eq. (16), and the imaginary part of the self-energy is evaluated using Eq. (A.5). In this case, the density matrix elements will occur between the same bands, so the singularity at $\mathbf{q}=0$ must be dealt with. This singularity is integrable. For tetrahedral integration cells containing the singular point, the loss is split into singular and non-singular parts

$$\text{Im}\langle n, \mathbf{k} | \Sigma(E) | n, \mathbf{k} \rangle = \langle n, \mathbf{k} | \Sigma_{\text{ns}}(E) | n, \mathbf{k} \rangle + \langle n, \mathbf{k} | \Sigma_s(E) | n, \mathbf{k} \rangle, \quad (20)$$

$$\begin{aligned} \text{Im}\langle n, \mathbf{k} | \Sigma_{\text{ns}}(E) | n, \mathbf{k} \rangle &= \frac{1}{\pi} \sum_{\mathbf{k}, \mathbf{k}'} \sum_{n'} \int_0^\infty d\omega \int_{\text{B.Z.}} \frac{d^3q}{(2\pi)^3} [W_{\mathbf{k}, \mathbf{k}'}^{(A)}(\mathbf{q}, \omega) \\ &\times \rho_{n'n'}(\mathbf{k}, \mathbf{q} + \mathbf{K}) \rho_{n'n'}^*(\mathbf{k}, \mathbf{q} + \mathbf{K}') - A_{n'n'}(\omega) / q^2] \\ &\times \delta(E - z.\text{epsiv};_{n'}(\mathbf{k} - \mathbf{q}) + \omega(2f_{n'} - 1)), \end{aligned} \quad (21)$$

$$\begin{aligned} \text{Im}\langle n, \mathbf{k} | \Sigma_s(E) | n, \mathbf{k} \rangle &= \frac{1}{\pi} \sum_{n'} \int_0^\infty d\omega \int_{\text{B.Z.}} \frac{d^3q}{(2\pi)^3} A_{n'n'}(\omega) / q^2 \\ &\times \delta(E - z.\text{epsiv};_{n'}(\mathbf{k} - \mathbf{q}) + \omega(2f_{n'} - 1)), \end{aligned} \quad (22)$$

where

$$A_{n'n'}(\omega) = 4\pi [z.\text{epsiv};_{0,0}^{-1}(\mathbf{q} \rightarrow \mathbf{0}, \omega)]^{(A)} |\rho_{n'n'}(\mathbf{k}, \mathbf{q} \rightarrow \mathbf{0})|^2.$$

The non-singular term $\text{Im}\langle n, \mathbf{k} | \Sigma_{\text{ns}}(E) | n, \mathbf{k} \rangle$ is integrated normally. The singular $\text{Im}\langle n, \mathbf{k} | \Sigma_s(E) | n, \mathbf{k} \rangle$ is integrated numerically over the constant-energy plane of the tetrahedron. While the singular evaluation is more time intensive, it is only needed for a small number of integration cells and is thus feasible.

The real part of the correlation self-energy can be found by determining $\text{Im}\langle n, \mathbf{k} | \Sigma(E) | n, \mathbf{k} \rangle$ over the full range of E where losses exist, and taking a Hilbert transform. The total self-energy is then found by adding the exchange self-energy. The quasiparticle energies can be recovered by adding the self-energy to the DFT Kohn–Sham eigenvalues and subtracting off the DFT exchange–correlation energy. While quasiparticle energies are not the primary focus of this work, we did take the opportunity to use the machinery developed here to calculate the bandgap of the materials under study since it essentially came at no additional cost and could be used to help validate our calculations.

We follow the usual practice of using the Kohn–Sham eigenvalues for the band energies when evaluating $\Sigma(E)$. If we denote the Kohn–Sham eigenvalues as $z.\text{epsiv};_n^{\text{KS}}(\mathbf{k})$, then

$$z.\text{epsiv};_n(\mathbf{k}) = z.\text{epsiv};_n^{\text{KS}}(\mathbf{k}) + \langle n, \mathbf{k} | \Sigma(z.\text{epsiv};_n(\mathbf{k})) | n, \mathbf{k} \rangle.$$

This leads to $\langle n, \mathbf{k} | \Sigma(z.\text{epsiv};_n^{\text{KS}}(\mathbf{k})) | n, \mathbf{k} \rangle$ being evaluated away from the true quasiparticle energy. This is handled in the typical fashion by computing the renormalization constant [31]

$$Z_n(\mathbf{k}) = \left[1 - \frac{\partial \langle n, \mathbf{k} | \Sigma(E) | n, \mathbf{k} \rangle}{\partial E} \Big|_{E = z.\text{epsiv};_n^{\text{KS}}(\mathbf{k})} \right]^{-1} \quad (23)$$

such that

$$\langle n, \mathbf{k} | \Sigma(z.\text{epsiv};_n(\mathbf{k})) | n, \mathbf{k} \rangle = Z_n(\mathbf{k}) \langle n, \mathbf{k} | \Sigma(z.\text{epsiv};_n^{\text{KS}}(\mathbf{k})) | n, \mathbf{k} \rangle.$$

The rate of interaction of quasiparticles are thus given by

$$\Gamma_n(\mathbf{k}) = 2 |\text{Im}[Z_n(\mathbf{k}) \langle n, \mathbf{k} | \Sigma(z.\text{epsiv};_n^{\text{KS}}(\mathbf{k})) | n, \mathbf{k} \rangle]|,$$

which we approximate as

$$\Gamma_n(\mathbf{k}) = 2 |[\text{Re } Z_n(\mathbf{k})][\text{Im} \langle n, \mathbf{k} | \Sigma(z.\text{epsiv};_n^{\text{KS}}(\mathbf{k})) | n, \mathbf{k} \rangle]|. \quad (24)$$

The lifetime of a quasiparticle is

$$\tau_n(\mathbf{k}) = \frac{1}{\Gamma_n(\mathbf{k})}.$$

The evaluation of the decay spectra was carried out in the limit of neglecting local fields, using Eq. (18). The decay particles are resolved by an energy ΔE , so that the quantity generated is the

energy integral of Eq. (17) between $E - \Delta E/2$ and $E + \Delta E/2$. Integrals of this form are discussed in Lehmann and Taut [44].

3.1. Application to Monte Carlo radiation transport simulations

In Monte Carlo radiation transport codes, electrons are propagated as free classical particles that can interact with materials through various physical processes, such as exciting bremsstrahlung radiation or ionizing core or valence electrons. Below a set energy cutoff, the particle track will be short compared to the macroscopic sizes of objects typically under consideration. No discrete excitations of lesser energy are allowed. Instead, the electron energy loss due to multiple low energy electronic excitations is handled in an average fashion. As the electron traverses matter, energy is continuously deposited at a rate that depends both on the material properties and the electron energy.

To extend this classical approach to lower energies and include all energy losses as discrete events, the chance of interaction of the electron must be known for every type of excitation, including the continuum of transitions involving valence to conduction band excitations. Typically, the chance of excitation is handled through the cross sections $\sigma_i(z.\text{epsiv};_i)$ or inverse mean free paths $\lambda_i^{-1}(z.\text{epsiv};_i)$ for each type of event i , which are related through the density of atoms N/V

$$\lambda_i^{-1}(z.\text{epsiv};_i) = \sigma_i(z.\text{epsiv};_i) N/V. \quad (25)$$

The rate at which a particle of velocity \mathbf{v} creates excitations of type i is related to $\lambda_i^{-1}(z.\text{epsiv};_i)$ by

$$\Gamma_i(z.\text{epsiv};_i) = \lambda_i^{-1}(z.\text{epsiv};_i) |\mathbf{v}|. \quad (26)$$

In this work, we have calculated the total rate at which the electron produces transitions from valence to conduction bands. This can be directly compared to the rate of other energy loss and scattering processes to directly include excitations from the valence band (core electron excitations, with their discrete energy levels and less complicated excitation probabilities, are already considered in these transport codes). Since the quantities worked within the codes are $\sigma_i(z.\text{epsiv};_i)$ or $\lambda_i^{-1}(z.\text{epsiv};_i)$, the valence excitation rate will be converted to an effective cross section per atom or mean free path. This allows the relative probabilities of creating a valence excitation to other kinds of excitations to be correctly determined. However, care must be taken not to confuse this with actual spatial path lengths, since comparisons are done for free classical particles with energy dispersion $z.\text{epsiv};_i(\mathbf{v}) = \mathbf{v} \times \mathbf{v} / (2m_e)$ rather than the band dependent energy dispersion of actual electrons in matter. True mean free paths for particles in a band can be extracted from the lifetimes through the relation [37] $\mathbf{v}_n(\mathbf{k}) = \nabla_{\mathbf{k}} z.\text{epsiv};_n(\mathbf{k})$ if spatial information on the track microstructure or nanostructure is needed.

A classical description of track producing particles can still be a useful approximation [4,5] when dealing with individual valence excitations. In this case, the quantities found in this work can be used to parametrize the curves for interband transitions and plasmon losses, which approximate the full set of valence to conduction transitions. With a proper parametrization, such simulations can reproduce detector response to ionizing radiation, including a full accounting of each charge carrier produced.

4. Results

The calculated LDA and the initial ABINIT *GW* band structure predicts that CsI has an indirect bandgap, with the minimum energy valence to conduction transition from the *M* point in the valence band to the Γ point in the conduction band. This predicted indirect gap is very close to the minimum optical gap

(at the Γ point). Reported measurements of the CsI bandgap are from ultraviolet absorption experiments, and consequently we only have the optical bandgap to compare. Our calculations of NaI lack this complication, with a minimum bandgap for the Γ to Γ point transition.

The experimentally accessible dielectric constant can be shown to be $\epsilon_{\infty} = 1/\epsilon_{0,0}^{-1}(\mathbf{q} \rightarrow 0, \omega \rightarrow 0)$ [26]. However, our calculations are carried out on a static lattice. In a real ionic solid, the application of a macroscopic longitudinal electric field at accessible frequencies would cause the ions to move in response, thus screening the field to a greater extent than is found from the electronic response alone. Fortunately, we can still make meaningful comparisons to measured values. At $\mathbf{q} \rightarrow 0$ and at frequencies far below the energy of the lowest transition, the perturbing field is essentially static as far as the electrons are concerned. In this limit, it makes no difference if the perturbing field is longitudinal or transverse—the electrons of the material are just reacting to a constant field within its volume. If we choose frequencies well below the lowest electronic transition we can use optical measurements to determine the electronic response. If this frequency also happens to be well above that of the highest phonon mode in the material, the lattice will be unable to keep up with the rapidly changing field. Under the approximation that the magnetic susceptibility of the medium is very close to the vacuum susceptibility, the index of refraction of the medium is given by [45] $n(\omega) = \sqrt{\epsilon_{\infty}(\mathbf{q} \rightarrow 0, \omega)}$. We therefore can compute the index of refraction in the low frequency limit and compare it to measured values in the wide gap between the highest phonon mode and lowest electronic transition (a value referred to as n_{∞} , to distinguish it from the static value n_0). This is shown in Table 2.

Fig. 1 shows the dielectric function $1/\epsilon_{0,0}^{-1}(\mathbf{q} \rightarrow 0, \omega)$, while Fig. 2 shows the diagonal loss function $\epsilon_{\mathbf{kk}}^{-1}(\mathbf{q}, \omega)$ for several momentum transfers. Several interesting features are evident in these plots. Plasmons result from anomalous dispersion causing the real part of the dielectric function to dip below zero within the region of transitions and then rise again past the localized region of high imaginary part resulting from the transitions. When the real part is near zero in this crossing and there are only weak transitions to populate the imaginary part, the dielectric function is much less than one indicating that the internal field is increased compared to the applied external field. This amplification of the internal field is a collective resonance of the material and corresponds to the plasmon. At plasmon resonances, the inverse dielectric function exhibits prominent peaks indicating regions of strong losses.

In CsI, an incipient plasmon in the 12–13 eV region resulting from the valence to conduction transitions is seen to be preempted by the rise of Cs 5p to conduction transitions in the 15–20 eV region of the spectrum, resulting in only a weak plasmon-like peak in the loss spectrum with a maximum at 12.7 eV (peak A in Fig. 3). A second broad plasmon is evident in the 18–29 eV region, due to the combined effect of the valence and semi-core electrons. This second plasmon has prominent peaks at 20.1 and 22.9 eV (peaks B and C, respectively, in Fig. 3). Plasmons

in the free electron gas are well understood due to their analytical solution, and exist only at low momentum transfers. We see a similar behavior here, with the plasmon resonances dying away at higher \mathbf{q} values. The structure between 13 and 21 eV that gives the double plasmon structure is found to be mostly due to transitions from orbitals with Cs 5p character. There is a small contribution from valence to conduction transitions, but contributions from orbitals with I 5s character, while not strictly zero, are found to be negligible with contributions of less than 1 part in 100 compared to valence and Cs 5p orbitals in this energy region. The binding energy of the Cs 5s shell is 22.7 eV [52]. If these orbitals were included in the calculations we would expect to see contributions in the screening functions between about 23 and 31 eV, which could have an effect on the second double plasmon peak. However, comparison with the I 5s orbitals suggests that the effect of this shell is negligible. Investigating the magnitude of this effect will be the subject of future work. It is encouraging, however, that the loss function at low momentum transfer is similar to that observed by Kreuzberg [46], with a prominent peak at 10.3 eV (peak A' in Fig. 3) and pair of higher amplitude peaks at 17.9 and 21.3 eV, as shown in Fig. 3 (peaks B' and C', respectively, in Fig. 3). In fact, our calculations reproduce many of the minor peaks seen in this reference as well, at a consistent 2–3 eV greater energy than observed in the experiment. The overestimation of the energies of the plasmon peaks is similar to what is observed in silicon. When the bandgap is corrected with GW calculations but the response function is computed with RPA, the Si plasmon peak is overestimated by approximately 2–3 eV [27]. Bethe–Salpeter corrections in Si, which introduce the conduction electron–hole interactions, correct this overestimation. In our calculations, the scissors operator introduces a uniform blue-shift of 1.5 eV while the complete set of bandgap corrections (including the scissors operator) from the DFT eigenvalues would be expected to result in a blue-shift on the order of 3 eV because a major effect of the GW correction is an overall energy increase of the conduction levels [42]. This indicates that, as was the case with silicon, the plasmon peaks are well reproduced in the RPA when using the bare DFT eigenvalues as the particle energies. We thus suspect that, as with silicon, Bethe–Salpeter calculations of the screening will allow a good representation of the plasmon structure while preserving the correct bandgap.

In NaI, the screening lacks strong core to conduction transitions and is thus simpler. A region of strong transitions emerges in the imaginary part of the dielectric function between 6 and 10 eV, and the recovery of the real part from below zero gives rise to a collective plasmon-like structure at around 18 eV. The presence of continued valence to conduction transitions in the 10–18 eV region delays the onset of the plasmon from its free-electron value of 9.05 eV. Again, the plasmon energy is overestimated compared to measured electron energy loss spectra [46], this time by about 5 eV. Much as with CsI, the plasmon is seen to be a phenomenon which occurs at low momentum transfer. At higher momentum transfers, the peak decreases in amplitude. In addition, it can be seen that, unlike CsI, the plasmon increases in energy with increasing momentum transfer before broadening sufficiently that it is no longer recognizable as a well defined excitation.

The electronic scattering rate of conduction electrons in NaI is shown in Fig. 4, and the same quantity for conduction electrons and Cs 5p character holes in CsI is shown in Fig. 5. The valence bands are shallow enough that their holes cannot excite any further electronic losses. The NaI bands with I 5s character show little dispersion, with energies ranging from 9.35 to 9.65 eV below the valence band maximum and a narrow range of loss rates between 1.85×10^{14} Hz and 2.0×10^{14} Hz. The six bands in CsI with strong Cs 5p character are nearly non-dispersive, with

Table 2

Indices of refraction from calculation and experiment [47]. For comparison, the value obtained from the full RPA screening calculations we performed are given and the value corresponding to that calculated by the ABINIT code for the screening matrix used in the initial GW calculations.

Material	Calculation ($\omega \rightarrow 0$)		Experiment (n_{∞})
	This work	ABINIT	
NaI	1.69	1.81	1.73
CsI	1.64	1.84	1.743

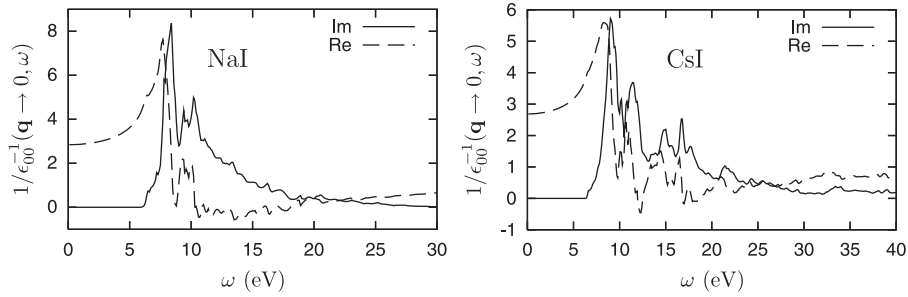


Fig. 1. The zero wave vector dielectric function of NaI (left) and CsI (right).

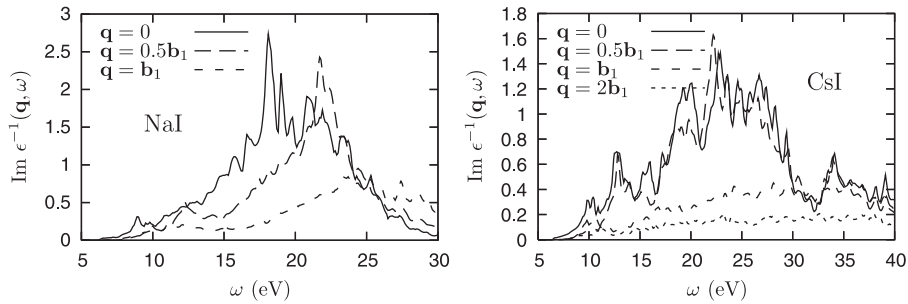


Fig. 2. The diagonal part of the loss function of NaI (left) and CsI (right) at various wave vectors in the direction of a primitive reciprocal lattice vector. Here, we use the convention that $\text{z.eps}^{-1}(\mathbf{q}, \omega) = \text{z.eps}^{-1}_{\mathbf{K}}(\mathbf{q}, \omega)$ for $\mathbf{q} = \mathbf{q}' + \mathbf{K}$ with \mathbf{q}' confined to the first Brillouin zone. The reciprocal lattice vectors have magnitude $|\mathbf{b}| = 1.50 \text{ \AA}^{-1}$ for NaI and $|\mathbf{b}| = 1.37 \text{ \AA}^{-1}$ in CsI.

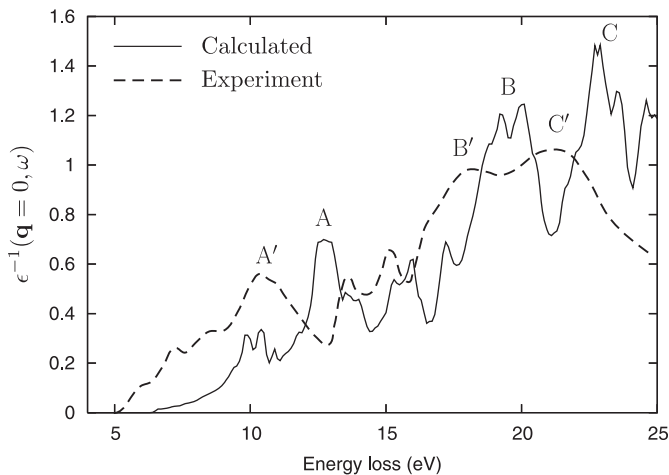


Fig. 3. The zero wave vector loss function of CsI (Solid) compared to the experimental electron energy loss spectrum of Creuzberg [46] (dashed). All major peaks are reproduced, but the calculated results are blue shifted by approximately 2–3 eV compared to the experiment. Major peaks are labeled, with corresponding calculated and measured peaks denoted by the same letter, but with a prime given to the label of the measured peaks.

energies close to 6.2 eV below the valence band maximum. Because these semi-core states are so close to one bandgap energy from the band edge, their lifetimes are strongly influenced by minor shifts in their energies. This sensitivity to the bandgap, neglect of excitons which allow excitation channels below the bandgap and self-trapping behavior which can lower the hole energy, suggests that the lifetimes of the shallowest Cs 5p states in the real material may vary by several orders of magnitude from our calculations. Because the calculated loss rate saturates at around 10^7 Hz for the deepest Cs 5p holes, we expect that states in the actual material with energies below the valence band maximum by a value significantly greater than one bandgap will tend to have loss rates in this range. The two CsI bands with I 5s

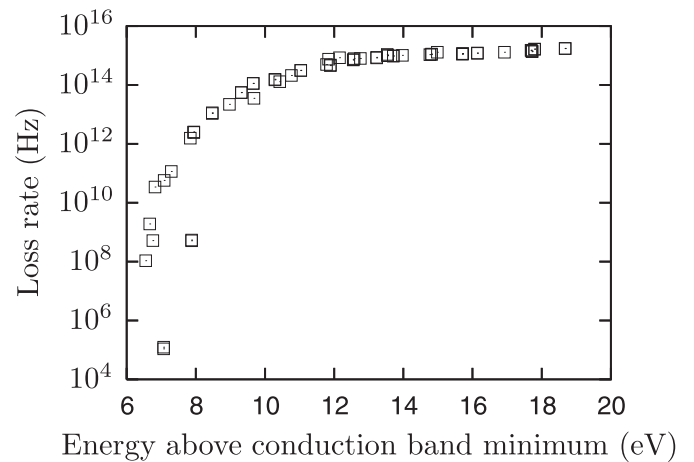


Fig. 4. Scattering rate of NaI conduction electron quasiparticles plotted against their energy.

character are also nearly non-dispersive, with energies ranging from 8.98 to 9.08 eV below the valence band maximum. The losses from these iodine 5s bands are much less affected by minor shifts in band structure, with loss rates near 1.3×10^{15} Hz. The I 5s holes in CsI are not plotted due to the narrow range of their properties and relatively flat dependence of loss on energy.

These figures illustrate how as quasiparticle energies decrease toward the excitation threshold, the rate of excitation drops dramatically and vanishes at the threshold. This is due to an increasingly restricted phase space available to the scattered and excited particles in the excitation rate and loss function integrals, to the point that at the threshold there is no available energy-allowed momentum states to scatter into. Similar behavior has long been known for the Fermi liquid, where quasiparticles at the fermi surface are lossless and the rate of loss increases with increasing energy for the same reason we see here [30]. However, in real materials quasiparticles at the threshold for electronic

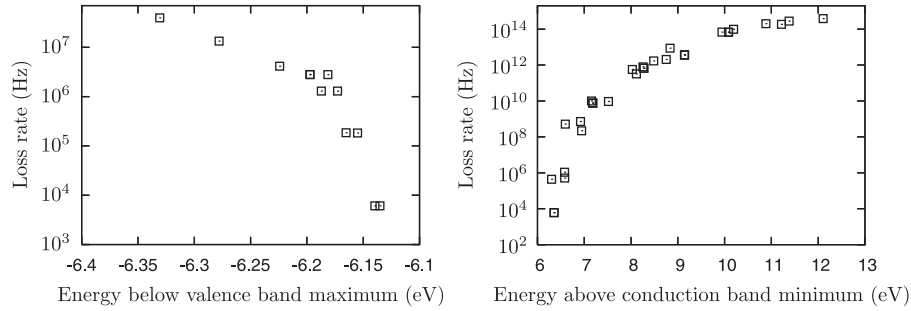


Fig. 5. Scattering rate of hole quasiparticles in the Cs 5p bands (left) of CsI and CsI conduction electron quasiparticles (right) plotted against their energy.

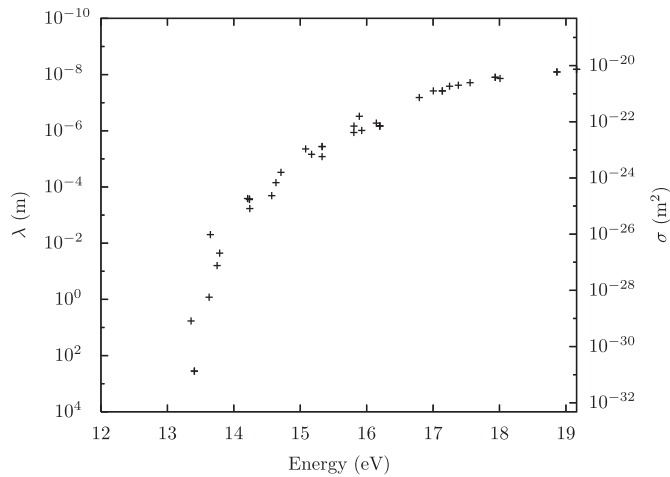


Fig. 6. Effective mean free path $\lambda(z, \epsilon_{\text{psiv}})$ and effective cross section $\sigma(z, \epsilon_{\text{psiv}})$ of CsI valence quasiparticles plotted against their energy as measured from the valence band maximum, the zero of energy used in the NWEGRIM Monte Carlo radiation transport code. In this figure, the magnitude of the classical particle velocity is determined by $|\mathbf{v}| = \sqrt{2z, \epsilon_{\text{psiv}}/m_e}$. The very long mean free paths near the excitation threshold are the result of considering electronic excitations alone—in a real material the mean free path would be significantly reduced for lower energy quasiparticles due to phonon excitations.

excitations do experience losses by scattering off the lattice to produce photons, an effect not considered in this work.

We note that the electronic losses follow a well defined curve as a function of quasiparticle energy. This feature is necessary to allow the classical Monte Carlo radiation transport to work at all. If quantum effects were to spread the loss rates for similar energies but different wave vectors out over many orders of magnitude, methods treating the radiation particles as ballistic objects would fail at low energies. Instead, while there is some variance in the loss rates, we see that the particles can be reasonably well approximated as having a rate of scattering that largely depends on energy with some added fluctuation. The relative fluctuations become largest near the threshold for electronic excitations. In practice, this is not expected to be a problem because near the threshold vibrational losses dominate. The effective mean free paths of conduction electrons in CsI are shown in Fig. 6.

The spectrum of energies of secondary electrons and holes at zero momentum transfer for selected energy transfers corresponding to plasmon-like excitations are shown in Fig. 7 for NaI and Fig. 8 for CsI. The single plasmon peak of NaI is seen to be composed of a majority of valence to conduction transitions, but excitations from the I 5s band to conduction bands have a noticeable minority contribution. The lower energy peak at 12.4 eV in CsI is seen to be made up of entirely valence to conduction transitions, which should be expected based on

energy conservation alone. The pair of peaks at 21.1 and 21.9 eV in CsI are almost entirely the result of transitions from Cs 5p-like orbitals to conduction states, with a small contribution from valence to conduction transitions and an almost negligible contribution from I 5s orbitals to conduction orbitals. These peaks could nearly be considered as typical core-level excitations superimposed on valence to conduction interband transitions, except that the collective screening brings these transitions into resonance and enhances the rate of these transitions.

5. Discussion

We have developed a technique for computing the electronic losses of quasiparticles in semiconductors and insulators. This procedure will give quasiparticle lifetimes and rates of scattering as well as the spectra of secondary particles produced by the scattering. We envision this information as aiding efforts to use low energy radiation transport Monte Carlo codes to simulate the measured signal of novel radiation detector materials. This method has been applied to sodium iodide and cesium iodide, materials commonly used in radiation scintillation detectors. Several aspects of the calculated electronic structure are in reasonably good agreement with experimentally measured values, such as the bandgap, index of refraction, and electron energy loss functions, although our novel predictions such as rate of loss or secondary spectra do not yet have experimental support.

The simulation of secondary particle spectra is still fairly primitive. These early results are calculated neglecting local fields and have been found only at selected energy and momentum transfers corresponding to peaks in the energy loss spectrum, where they can be interpreted as the decay of plasmons. We envision calculation of these spectra and associated cross sections for a grid of energy and momentum transfers that allow replacement of the parametrized free electron gas like models currently used in the Monte Carlo radiation transport simulations with the *ab initio* quantities at low energy and momentum transfers where band structure is expected to have a significant effect on the electronic scattering process.

There are several areas where additional progress would be useful in simulating electronic stopping of charged particles. The inclusion of Bethe–Salpeter effects in the screening will allow the consideration of exciton states, will improve the low energy structure of the dielectric function, and will refine the location of the plasmon resonance. An extension of the method to cover non-cubic materials, whose dielectric response as $\mathbf{q} \rightarrow 0$ is a tensor rather than a scalar, would be useful. In addition, we have only considered electronic losses of the charge carriers. For an accurate end-of-track simulation, the phonon losses will also be needed.

With vacuum levels close to the conduction band minimum, CsI in particular [53] is attractive as a photocathode and offers the

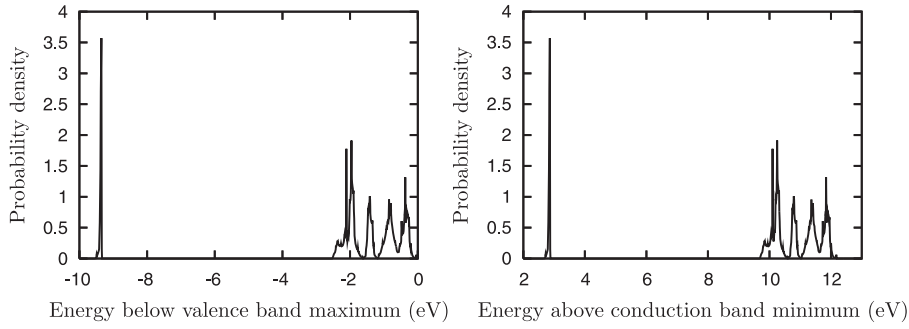


Fig. 7. Secondary spectrum of holes (left) and conduction electrons (right) in NaI for the peak of the 18.1 eV plasmon-like excitation at zero momentum transfer. Note that since the energy of the excitation is fixed, both hole and conduction electron spectra have the same shape and differ only by an overall shift of their energy.

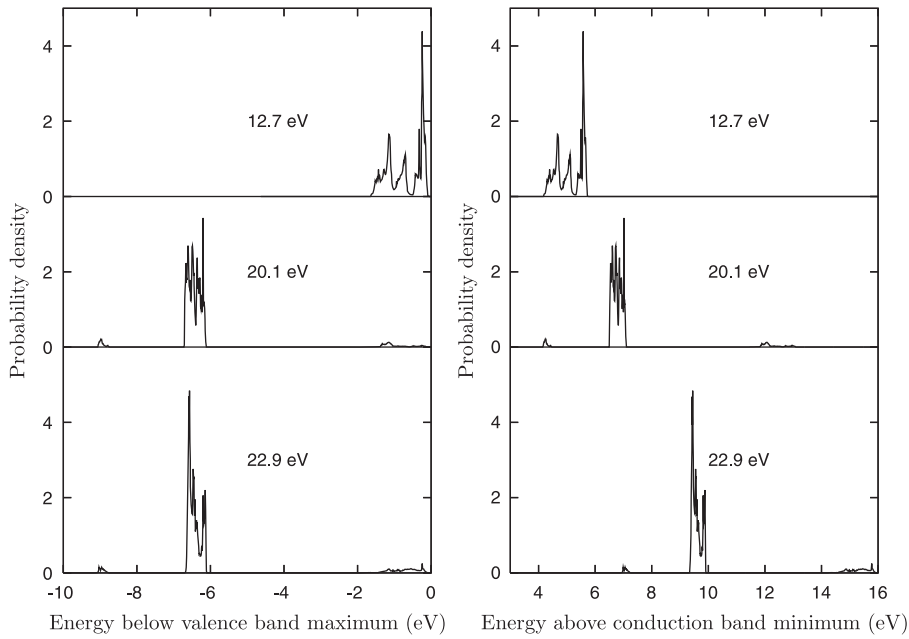


Fig. 8. Secondary spectrum of holes (left) and conduction electrons (right) in CsI for peaks of plasmon-like excitations at zero momentum transfer.

possibility of combining electron energy loss with energy measurements of the emitted secondary electrons to directly resolve the secondary particle spectra for various energy and momentum transfers. Further refinement of coupling between these *ab initio* calculations and Monte Carlo radiation transport codes could lead to comparisons of calculated values of electron escape depth and quantum efficiency of alkali halide photocathodes with measured values.

Acknowledgments

This research was supported by the National Nuclear Security Administration, Office of Nuclear Nonproliferation Research and Engineering (NA-22), of the US Department of Energy (DOE) at the Pacific Northwest National Laboratory, a multiprogram national laboratory operated by Battelle for the U.S. Department of Energy under Contract DE-AC05-76RL01830.

Appendix A. Derivation of the secondary particle spectrum

In this appendix we will put the assumption that the electronic excitations can be decomposed into individual particle–hole like excitations on firmer theoretical footing.

The spectral representation of W from Eq. (15) allows us to separate the self-energy into an exchange part Σ_x and correlation part Σ_c

$$\langle n, \mathbf{k} | \Sigma_x(E) | n, \mathbf{k} \rangle = 4\pi \sum_{n'}^{\text{occ}} \int_{\text{B.Z.}} \frac{d^3 q}{(2\pi)^3} \sum_{\mathbf{K}} \frac{|\rho_{nn'}(\mathbf{k}, \mathbf{q} + \mathbf{K})|^2}{|\mathbf{q} + \mathbf{K}|^2}, \quad (\text{A.1})$$

$$\langle n, \mathbf{k} | \Sigma_c(E) | n, \mathbf{k} \rangle = \frac{i}{\pi} \int_0^\infty d\omega \sum_{n'} \int_{\text{B.Z.}} \frac{d^3 q}{(2\pi)^3} \sum_{\mathbf{K}, \mathbf{K}'} W_{\mathbf{K}, \mathbf{K}'}^{(A)}(\mathbf{q}, \omega) \frac{\rho_{nn'}(\mathbf{k}, \mathbf{q} + \mathbf{K}) \rho_{nn'}^*(\mathbf{k}, \mathbf{q} + \mathbf{K}')}{E - z.\text{epsiv}_{;n}(\mathbf{k} - \mathbf{q}) - (\omega - i\eta)(1 - 2f_{n'})}, \quad (\text{A.2})$$

where occ means that the sum is taken only over occupied bands. The exchange self-energy is purely real, only the correlation contribution leads to losses. Define a matrix in the space of reciprocal lattice vectors

$$M_{\mathbf{K}, \mathbf{K}'}(\mathbf{k}, \mathbf{q}, E, \omega) = i \frac{\rho_{nn'}(\mathbf{k}, \mathbf{q} + \mathbf{K}) \rho_{nn'}^*(\mathbf{k}, \mathbf{q} + \mathbf{K}')}{E - z.\text{epsiv}_{;n}(\mathbf{k} - \mathbf{q}) - (\omega - i\eta)(1 - 2f_{n'})}. \quad (\text{A.3})$$

Split this matrix into a Hermitian and an anti-Hermitian part, $M_{\mathbf{K}, \mathbf{K}'}^{(H)}(\mathbf{k}, \mathbf{q}, E, \omega)$ and $M_{\mathbf{K}, \mathbf{K}'}^{(A)}(\mathbf{k}, \mathbf{q}, E, \omega)$, respectively. We now have

$$\langle n, \mathbf{k} | \Sigma_c(E) | n, \mathbf{k} \rangle = \frac{1}{\pi} \int_0^\infty d\omega \sum_{n'} \int_{\text{B.Z.}} \frac{d^3 q}{(2\pi)^3} \times \text{Tr}[M(\mathbf{k}, \mathbf{q}, E, \omega) W^{(A)}(\mathbf{q}, \omega)]. \quad (\text{A.4})$$

$\text{Tr}[M^{(H)}(\mathbf{k}, \mathbf{q}, E, \omega)W^{(A)}(\mathbf{q}, \omega)]$ is pure imaginary while $\text{Tr}[M^{(A)}(\mathbf{k}, \mathbf{q}, E, \omega)W^{(A)}(\mathbf{q}, \omega)]$ is entirely real. Therefore,

$$\text{Im} \langle n, \mathbf{k} | \Sigma(E) | n, \mathbf{k} \rangle = \frac{1}{\pi} \int_0^\infty d\omega \sum_{n'} \int_{\text{B.Z.}} \frac{d^3 q}{(2\pi)^3} \times \text{Tr}[M^{(H)}(\mathbf{k}, \mathbf{q}, E, \omega)W^{(A)}(\mathbf{q}, \omega)]$$

and

$$\Gamma_n(\mathbf{k}) = \frac{2}{\pi} \left| \int_0^\infty d\omega \sum_{n'} \int_{\text{B.Z.}} \frac{d^3 q}{(2\pi)^3} \sum_{\mathbf{K}, \mathbf{K}'} i \rho_{nn'}(\mathbf{k}, \mathbf{q} + \mathbf{K}) \rho_{nn'}^*(\mathbf{k}, \mathbf{q} + \mathbf{K}') \times W_{\mathbf{K}, \mathbf{K}'}^{(A)}(\mathbf{q}, \omega) \delta(z.\text{epsiv};_n(\mathbf{k}) - z.\text{epsiv};_{n'}(\mathbf{k} - \mathbf{q}) - \omega(1 - 2f_{n'})) \right|. \quad (\text{A.5})$$

The rate of creation of excitations with energy ω , wave vector \mathbf{q} , and reciprocal lattice vectors \mathbf{K} and \mathbf{K}' thus becomes

$$\gamma_{n, \mathbf{K}, \mathbf{K}'}(\mathbf{k}; \mathbf{q}, \omega) = \frac{2}{\pi} \sum_{n'} i W_{\mathbf{K}, \mathbf{K}'}^{(A)}(\mathbf{q}, \omega) \rho_{nn'}(\mathbf{k}, \mathbf{q} + \mathbf{K}) \rho_{nn'}^*(\mathbf{k}, \mathbf{q} + \mathbf{K}') \times \delta(z.\text{epsiv};_n(\mathbf{k}) - z.\text{epsiv};_{n'}(\mathbf{k} - \mathbf{q}) - \omega(1 - 2f_{n'})) \quad (\text{A.6})$$

such that

$$\Gamma_n(\mathbf{k}) = \left| \int d\omega \int_{\text{B.Z.}} \frac{d^3 q}{(2\pi)^3} \sum_{\mathbf{K}, \mathbf{K}'} \gamma_{n, \mathbf{K}, \mathbf{K}'}(\mathbf{k}; \mathbf{q}, \omega) \right|. \quad (\text{A.7})$$

This rate $\gamma_{n, \mathbf{K}, \mathbf{K}'}(\mathbf{k}; \mathbf{q}, \omega)$ can then be considered an un-normalized spectrum of electronic excitations produced by an electron in band n with momentum \mathbf{k} .

We consider these electronic excitations to act as intermediate particles, and find the decay spectra of the excitations themselves. We can determine the secondary particles produced by a given conduction electron via a two-step process—first, find the electronic excitation quasiparticles; and second, resolve the decay of these quasiparticles.

We note that

$$W_{\mathbf{K}, \mathbf{K}'}(\mathbf{q}, \omega) = \frac{4\pi}{|\mathbf{q} + \mathbf{K}| |\mathbf{q} + \mathbf{K}'|} \times \sum_{\mathbf{k}_1, \mathbf{k}_2} [z.\text{epsiv};_{\mathbf{k}, \mathbf{k}_1}(\mathbf{q}, \omega)]^{-1} z.\text{epsiv};_{\mathbf{k}_1, \mathbf{k}_2}^\dagger(\mathbf{q}, \omega) [z.\text{epsiv};_{\mathbf{k}_2, \mathbf{K}'}^\dagger(\mathbf{q}, \omega)]^{-1} \quad (\text{A.8})$$

from which it is easy to show that

$$W_{\mathbf{K}, \mathbf{K}'}^{(A)}(\mathbf{q}, \omega) = \frac{-4\pi}{|\mathbf{q} + \mathbf{K}| |\mathbf{q} + \mathbf{K}'|} \times \sum_{\mathbf{k}_1, \mathbf{k}_2} [z.\text{epsiv};_{\mathbf{k}, \mathbf{k}_1}(\mathbf{q}, \omega)]^{-1} z.\text{epsiv};_{\mathbf{k}_1, \mathbf{k}_2}^{(A)}(\mathbf{q}, \omega) [z.\text{epsiv};_{\mathbf{k}_2, \mathbf{K}'}^\dagger(\mathbf{q}, \omega)]^{-1}. \quad (\text{A.9})$$

From Eq. (1) we have for positive frequencies

$$z.\text{epsiv};_{\mathbf{k}, \mathbf{K}'}^{(A)}(\mathbf{q}, \omega > 0) = i\pi \frac{4\pi}{|\mathbf{q} + \mathbf{K}| |\mathbf{q} + \mathbf{K}'|} \sum_c \sum_v^{\text{unocc}} \int_{\text{B.Z.}} \frac{d^3 k}{(2\pi)^3} \times \rho_{cv}(\mathbf{k}, \mathbf{q} + \mathbf{K}) \rho_{cv}^*(\mathbf{k}, \mathbf{q} + \mathbf{K}') \delta(\omega - z.\text{epsiv};_c(\mathbf{k}) + z.\text{epsiv};_v(\mathbf{k} - \mathbf{q})) \quad (\text{A.10})$$

This has the interpretation of the applied field causing transitions of electrons from occupied valence orbitals v with momentum $\mathbf{k} - \mathbf{q}$ and energy $z.\text{epsiv};_v(\mathbf{k} - \mathbf{q})$ to unoccupied conduction orbitals c with momentum \mathbf{k} and energy $z.\text{epsiv};_c(\mathbf{k})$. These are the decay particles we are interested in. We then arrive at

$$W_{\mathbf{K}, \mathbf{K}'}^{(A)}(\mathbf{q}, \omega) = \frac{-16\pi^3 i}{|\mathbf{q} + \mathbf{K}| |\mathbf{q} + \mathbf{K}'|} \sum_c \sum_v^{\text{unocc}} \int_{\text{B.Z.}} \frac{d^3 k}{(2\pi)^3} \times \sum_{\mathbf{k}_1, \mathbf{k}_2} \frac{[z.\text{epsiv};_{\mathbf{k}, \mathbf{k}_1}(\mathbf{q}, \omega)]^{-1} [z.\text{epsiv};_{\mathbf{k}_2, \mathbf{K}'}^\dagger(\mathbf{q}, \omega)]^{-1}}{|\mathbf{q} + \mathbf{K}_1| |\mathbf{q} + \mathbf{K}_2|}$$

$$\times \rho_{cv}(\mathbf{k}, \mathbf{q} + \mathbf{K}_1) \rho_{cv}^*(\mathbf{k}, \mathbf{q} + \mathbf{K}_2) \delta(\omega - z.\text{epsiv};_c(\mathbf{k}) + z.\text{epsiv};_v(\mathbf{k} - \mathbf{q})). \quad (\text{A.11})$$

We can immediately see that, up to a normalization factor, the loss function is composed of excitations from c to v and a final momentum of \mathbf{k} with an un-normalized joint distribution function of

$$L_{cv, \mathbf{K}, \mathbf{K}'}(\mathbf{k}; \mathbf{q}, \omega) = -4\pi^2 i \sum_{\mathbf{k}_1, \mathbf{k}_2} \frac{[z.\text{epsiv};_{\mathbf{k}, \mathbf{k}_1}(\mathbf{q}, \omega)]^{-1} [z.\text{epsiv};_{\mathbf{k}_2, \mathbf{K}'}^\dagger(\mathbf{q}, \omega)]^{-1}}{|\mathbf{q} + \mathbf{K}_1| |\mathbf{q} + \mathbf{K}_2|} \times \rho_{cv}(\mathbf{k}, \mathbf{q} + \mathbf{K}_1) \rho_{cv}^*(\mathbf{k}, \mathbf{q} + \mathbf{K}_2) \delta(\omega - z.\text{epsiv};_c(\mathbf{k}) + z.\text{epsiv};_v(\mathbf{k} - \mathbf{q})) \quad (\text{A.12})$$

such that

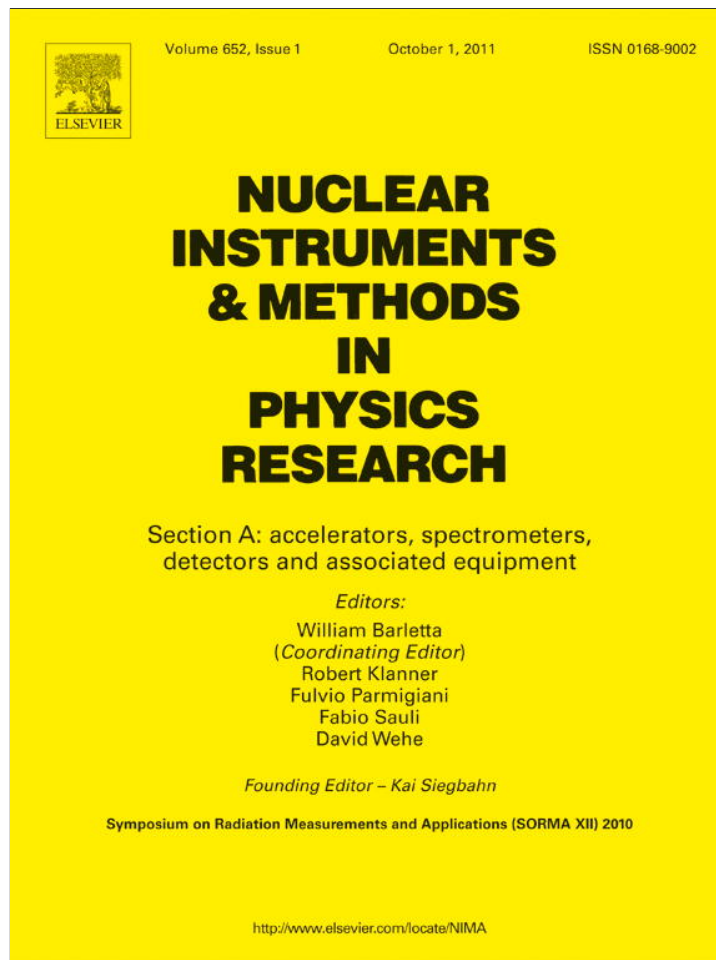
$$W_{\mathbf{K}, \mathbf{K}'}^{(A)}(\mathbf{q}, \omega) = \frac{4\pi}{|\mathbf{q} + \mathbf{K}| |\mathbf{q} + \mathbf{K}'|} \sum_c \sum_v^{\text{unocc}} \int_{\text{B.Z.}} \frac{d^3 k}{(2\pi)^3} L_{cv, \mathbf{K}, \mathbf{K}'}(\mathbf{k}; \mathbf{q}, \omega). \quad (\text{A.13})$$

We may identify the function L as the partial contribution to the loss function due to the given excitation.

References

- [1] MCNP5 User's Manual, LANL Reports LA-UR-03-1987. Available from: http://mcnp-green.lanl.gov/pdf/MCNP5_Manual_Volume_1_LA-UR-03-1987.pdf.
- [2] S. Agostinelli, et al., Nucl. Instrum. Methods A 506 (2003) 250; J. Allison, et al., IEEE Trans. Nucl. Sci. 53 (2006) 270; GEANT4 Physics Reference Manual. Available from: <http://geant4.web.cern.ch/geant4/UserDocumentation/UsersGuides/PhysicsReferenceManual/html/PhysicsReferenceManual.html>.
- [3] J.D. Martínez, R. Mayol, F. Salvat, J. Appl. Phys. 67 (1988) 2955.
- [4] F. Gao, L.W. Campbell, R. Devanathan, Y. Xie, L. Corrales, A.J. Peurrung, W.J. Weber, Nucl. Instrum. Methods A 579 (2007) 292.
- [5] F. Gao, L.W. Campbell, R. Devanathan, Y. Xie, Y. Zhang, A.J. Peurrung, W.J. Weber, Nucl. Instrum. Methods B 255 (2007) 286.
- [6] F.P. Santos, T.H.V.T. Dias, P.J.B.M. Rachinhos, C.A.N. Conde, J. Appl. Phys. 89 (2001) 8202.
- [7] G.W. Fraser, A.F. Abbey, A. Holland, K. McCarthy, A. Owens, A. Wells, Nucl. Instrum. Methods A 350 (1994) 368.
- [8] M. Palumbo, O. Pulci, A. Marini, L. Reining, R. Del Sole, Phys. Rev. B 74 (2006) 235431.
- [9] J.P. Walter, M.L. Cohen, Phys. Rev. B 5 (1972) 3101.
- [10] M.S. Hybertsen, S.G. Louie, Phys. Rev. B 35 (1987) 5585.
- [11] S. Baroni, R. Resta, Phys. Rev. B 33 (1986) 7017.
- [12] J.L.P. Hughes, J.E. Sipe, Phys. Rev. B 53 (1996) 10751.
- [13] T. Boutboul, A. Akkerman, A. Breskin, R. Chechik, J. Appl. Phys. 79 (1996) 6714.
- [14] L. Hedin, Phys. Rev. 139A (1965) 796.
- [15] I. Campillo, J.M. Pitarke, A. Rubio, E. Zarate, P.M. Echenique, Phys. Rev. Lett. 83 (1999) 2230.
- [16] J.A. Soininen, J.J. Rehr, E.L. Shirley, J. Phys.: Condens. Matter 15 (2003) 2573.
- [17] B. Arnaud, S. Lebègue, M. Alouani, Phys. Rev. B 71 (2005) 035308.
- [18] A.P. Sorini, J.J. Kas, J.J. Rehr, M.P. Prange, Z.H. Levine, Phys. Rev. B 74 (2006) 165111.
- [19] R. Mayol, F. Salvat, J. Phys. B: At. Mol. Opt. Phys. 23 (1990) 2117.
- [20] D.E. Cullen, J.H. Hubbell, L. Kissel, EDPL97: The Evaluated Data Library, '97 Version, Report UCRL-50400, vol. 6, rev. 5, 1997.
- [21] F. Gao, Y. Xie, S. Kerisit, L.W. Campbell, W.J. Weber, Nucl. Instrum. Methods Phys. Res. A 652 (2011) 564.
- [22] Z. Wang, Y.-L. Xie, B.D. Cannon, L.W. Campbell, F. Gao, S. Kerisit, J. Appl. Phys. 110 (2011) 064903.
- [23] S. Kerisit, K.M. Rosso, B.D. Cannon, IEEE Trans. Nucl. Sci. 55 (2008) 1251.
- [24] S. Kerisit, K.M. Rosso, B.D. Cannon, F. Gao, Y. Xie, J. Appl. Phys. 105 (2009) 114915.
- [25] S.L. Adler, Phys. Rev. 126 (1962) 413.
- [26] N. Wiser, Phys. Rev. 129 (1963) 62.
- [27] V. Olevano, L. Reining, Phys. Rev. Lett. 86 (2001) 5962.
- [28] J.J. Sakurai, Modern Quantum Mechanics, Addison Wesley, Reading, 1994.
- [29] D. Pines, Elementary Excitations in Solids, Perseus, Reading, 1999.
- [30] J.W. Negele, H. Orland, Quantum Many-Particle Systems, Addison Wesley, Reading, 1988.
- [31] W.G. Aulbur, L. Jönsson, J.W. Wilkins, Solid State Phys. 54 (2000) 1.
- [32] M.S. Chung, T.E. Everhart, Phys. Rev. B 15 (1977) 4699.
- [33] abinit.org and ABINIT code. Available from: <http://www.abinit.org>.
- [34] X. Gonze, J.-M. Beuken, R. Caracas, F. Detraux, M. Fuchs, G.-M. Rignanese, L. Sindic, M. Verstraete, G. Zerah, F. Jollet, M. Torrent, A. Roy, M. Mikami, Ph. Ghosez, J.-Y. Raty, D.C. Allan, Comput. Mater. Sci. 25 (2002) 478.

- [35] X. Gonze, G.-M. Rignanese, M. Verstraete, J.-M. Beuken, Y. Pouillon, R. Caracas, F. Jollet, M. Torrent, G. Zerah, M. Mikami, Ph. Ghosez, M. Veithen, J.-Y. Raty, V. Olevano, F. Bruneval, L. Reining, R. Godby, G. Onida, D.R. Hamann, D.C. Allan, *Z. Kristallogr.* 220 (2005) 558.
- [36] W. Kohn, L.J. Sham, *Phys. Rev.* 140 (1965) A1133.
- [37] N.W. Ashcroft, N.D. Mermin, *Solid State Physics*, Saunders College, Fort Worth, 1976.
- [38] K. Asaumi, *Phys. Rev. B* 29 (1984) 1118.
- [39] T.B. Rymer, P.G. Hambling, *Acta Cryst.* 4 (1951) 565.
- [40] N. Troullier, J.L. Martins, *Phys. Rev. B* 43 (1991) 1993.
- [41] G.A. Baraff, M. Schlüter, *Phys. Rev. B* 30 (1984) 3460.
- [42] F. Gygi, A. Baldereschi, *Phys. Rev. Lett.* 62 (1989) 2160.
- [43] M.S. Hybertsen, S.G. Louie, *Phys. Rev. B* 34 (1986) 5390.
- [44] G. Lehmann, M. Taut, *Phys. Status Solidi B* 54 (1972) 469.
- [45] J.D. Jackson, *Classical Electrodynamics*, Wiley, New York, 1975.
- [46] M. Creuzberg, *Z. Phys.* 196 (1966) 433.
- [47] W.J. Tropf, T.J. Harris, M.E. Thomas, in: R.W. Waynant, M.N. Ediger (Eds.), *Electro-Optics Handbook*, McGraw-Hill, New York, 2004.
- [48] J.E. Eby, K.J. Teegarden, D.B. Dutton, *Phys. Rev.* 116 (1959) 1099.
- [49] J.C. Phillips, *Phys. Rev.* 136 (1964) A1705. Note that when compared to Fig. 11, Table VII appears to have a misprint for the $\text{NaI } I_{15}^{3/2} \rightarrow \Gamma_1$ transition.
- [50] K. Teegarden, G. Baldini, *Phys. Rev.* 155 (1967) 896.
- [51] J.J. Hopfield, J.M. Worlock, *Phys. Rev.* 137 (1965) A1455.
- [52] J.A. Bearden, A.F. Burr, *Rev. Mod. Phys.* 39 (1967) 125.
- [53] T.H. DiStefano, W.E. Spicer, *Phys. Rev. B* 7 (1973) 1554.



This article appeared in a journal published by Elsevier. The attached copy is furnished to the author for internal non-commercial research and education use, including for instruction at the authors institution and sharing with colleagues.

Other uses, including reproduction and distribution, or selling or licensing copies, or posting to personal, institutional or third party websites are prohibited.

In most cases authors are permitted to post their version of the article (e.g. in Word or Tex form) to their personal website or institutional repository. Authors requiring further information regarding Elsevier's archiving and manuscript policies are encouraged to visit:

<http://www.elsevier.com/copyright>



Contents lists available at ScienceDirect

Nuclear Instruments and Methods in
Physics Research Ajournal homepage: www.elsevier.com/locate/nima

Yield, variance and spatial distribution of electron–hole pairs in CsI

F. Gao^{a,*}, Y. Xie^a, S. Kerisit^a, L.W. Campbell^a, W.J. Weber^{b,c}^a Pacific Northwest National Laboratory, Richland, WA 99352, USA^b Department of Materials Science & Engineering, University of Tennessee, Knoxville, TN 37996, USA^c Materials Science and Technology Division, Oak Ridge National Laboratory, Oak Ridge, TN 37831, USA

ARTICLE INFO

Available online 8 September 2010

Keywords:

Monte Carlo simulation
Intrinsic properties
Spatial distribution
Electron–hole pairs
CsI

ABSTRACT

A Monte Carlo (MC) method previously developed has been applied to simulate the interaction of photons, with energies ranging from 50 eV to ~1 MeV, with CsI and the subsequent electron cascades. The MC model has been employed to compute nano-scale spatial distributions of electron–hole pairs and important intrinsic properties, including W , the mean energy per electron–hole pair, and the Fano factor, F . W exhibits discontinuities at the shell edges that follow the photoionization cross-sections and decreases with increase in photon energy (from ~19 to 15 eV), with an asymptotic value of 15.2 eV at high energy. This decrease may contribute to the initial rise in relative light yield with incident energy observed experimentally for CsI, thus suggesting that nonlinearity may be associated with intrinsic properties of the material at low energies. F is calculated to increase with increase in energy and has an asymptotic value of 0.28. A significant number of electron–hole pairs is produced through the different ionization channels of core shells and the corresponding relaxation processes, which may explain why F is larger for CsI than for Si or Ge. Finally, the calculated spatial distributions show that the electron–hole pairs are primarily distributed along fast electron tracks. These spatial distributions constitute important input for large-scale simulations of electron–hole pair transport.

© 2010 Elsevier B.V. All rights reserved.

1. Introduction

The development of new inorganic scintillators is driven by the wide range of interests associated with medical imaging, radiation detector physics and security inspection. Many scintillation materials exhibit a nonlinear behavior of their scintillation response, which degrades the energy resolution achievable with these materials [1]. Although nonlinearity has been investigated for a range of scintillators over the last fifty years [2,3], its physical origin is not yet clearly understood.

Several approaches have been taken to model the light yield nonlinearity of inorganic scintillators. In early works by Dorenbos and co-workers [4,5], the nonlinearity of NaI (Tl) was modeled by combining electron–hole pair tracks calculated with a radiation transport code with a function that described the luminescence efficiency as a function of electron–hole pair density. More recently, Payne et al. [6] presented a model in which the light yield was described as a product of the efficiencies of two competing processes, namely, the recombination of electron–hole pairs and exciton–exciton annihilation. The former was determined based on the Onsager theory, whereas the latter was described using the Birks equation. Payne et al. showed that the

nonlinearity response curves of a wide range of inorganic scintillators could be fitted using this model, based on linear densities obtained with the Bethe–Bloch equation. Finally, a family of phenomenological models was developed by Bizarri et al. [7–9]. These models combined electron–hole pair densities obtained from the Bethe–Bloch equation or energy loss functions with a series of analytical rate equations that described different energy transfer processes. Both radiative and non-radiative processes were considered and these adopted a linear, quadratic or cubic dependence on the electron–hole pair density. The light yield response curves of several model compounds, chosen to represent the spectrum of nonlinear behaviors observed experimentally, were successfully modeled using this approach. In all the models discussed in the above, an important factor that guides the modeling strategy is the hypothesis that nonlinearity is ultimately related to the energy dependence of the density of electron–hole pairs along the ionization track. Therefore, a comprehensive understanding of track structures resulting from the interaction of high-energy particles with inorganic scintillators is crucial to our success in modeling the nonlinear response of these materials.

A Monte Carlo code, Northwest Electron and Gamma Ray Interaction in Matter (NWEGRIM) [10], has been developed to simulate energy cascades resulting from the interaction of electrons and gamma rays with semiconductor and scintillator materials. As described in this paper, important features of this

* Corresponding author. Tel.: +509 371 6490; fax: +509 371 6242.
E-mail address: fei.gao@pnl.gov (F. Gao).

program include its ability to follow the energy cascade down to energies on the order of the band gap and to compute the spatial distribution of electron–hole pairs (i.e., microscopic track structure). This allows for the use of a new approach in which the fate of individual electron–hole pairs is followed using an atomistic kinetic Monte Carlo model. This model was used to evaluate the contribution of an annihilation mechanism between self-trapped excitons (STE) to the scintillation response of pure CsI and LaBr₃(Ce) [11]. This study indicated that STE–STE annihilation could account for the initial rise in relative light yield with increase in incident energy for both materials. However, more remains to be done to fully understand the origins of nonlinearity and account for all experimental observations. For example, experimental findings on the dependence of nonlinearity on the activator concentration [2] and nature [12] have not been fully explained theoretically. It is certain, however, that the success of our modeling approach will be highly dependent upon our ability to compute accurately electron–hole pair spatial distributions.

Therefore, in the present study, NWEGRIM has been extended to simulate electron cascades and the fundamental mechanisms that govern the creation and spatial distribution of electron–hole pairs in CsI for energies ranging from a few eV to MeV. The mean energy to create an electron–hole pair, W , and its intrinsic variance are determined as a function of photon energy. Furthermore, the nano-scale features of the spatial distribution of electron–hole pairs induced by photons and electrons in CsI are also explored.

2. Monte Carlo simulation

The interactions of photons with atoms result in the creation of fast electrons that can directly interact with materials to create electron–hole pairs. The NWEGRIM code follows the collision of each individual particle generated during the energy cascade. The general approach is to calculate the total cross-section at an energy E from the cross-sections of individual processes, from which the mean free path is determined. Then, the particle is advanced by this distance. The individual cross-sections are sampled to determine what interaction has occurred. This procedure is repeated until the particle energy falls below a cut-off energy (\sim band gap of material).

The interaction of a photon with atoms occurs through inner-shell photoionization, the Compton scattering and electron–positron pair production. The cross-sections for these processes were obtained by the LLNL Evaluated Photon Data Library [13], relativistic impulse approximation [14] and the XCOM program [15]. In photoionization and Compton scattering processes, an electron is emitted and the residual excited ion decays through the emission of Auger/Coster–Kronig and fluorescence photons as well as shake-off emission. The possible relative relaxation pathways through these non-radiative and radiative transitions are extracted from the LLNL Evaluated Atomic Data Library [13], while the probabilities of electron shake-off after the creation of an inner-shell vacancy in Cs and I are approximated by averaging probabilities for the rare gases [16].

All the primary and secondary electrons created will further interact with CsI through a number of possible mechanisms, including interband transitions, plasmon excitation, core shell ionizations from K to O shells and electron–phonon interactions, as well as Bremsstrahlung emission. To determine which atomic shell is ionized, the cross-sections of individual inner shells are calculated using an optical-data model of the generalized oscillator strength (GOS) [17]. The generation of each core level vacancy in the simulation is followed by an Auger/Coster–Kronig and shake-off electron cascade. The cross-sections of the

electron–optical phonon interactions are calculated using the theory of Llacer and Garwin [18], while those of the electron–acoustical phonon interactions are evaluated from the model developed by Bradford and Woolf [19]. Based on the GOS method, we have developed a new model to evaluate the electron mean free paths of interband transition and plasmon excitation over a wide energy range (from several eV to a few hundred MeV) in a relativistic kinematics framework, which will be described elsewhere. In this mode, the cross-sections at low energy range (< 100 eV) can be fitted to ab initio calculations. The mean energy loss involved in plasmon excitation by a fast electron is calculated by

$$S_p = -(dE/dx)\lambda_p \quad (1)$$

where dE/dx is the electron stopping power for plasmon formation and λ_p is the mean free path. Energy loss due to plasmon creation is defined as E_{loss} , and the kinetic energy of the incident electron, E'_e , can be calculated by

$$E'_e = E_e - E_{loss} \quad (2)$$

where E_e is the initial kinetic energy of an incident electron. A random sampling algorithm is employed to obtain the energy loss of an incident electron due to an interband transition, as detailed in Ref. [10]. The cross-sections of the Bremsstrahlung process developed by Salvat and Fernández-Varea [20] are employed, and a random sampling approach is used to evaluate the electron energy loss. The angular differential cross-sections for elastic collisions are obtained from partial wave calculations, as described in Ref. [21], which are accurate for kinetic energies less than 2 MeV. We have further developed the NWEGRIM code to include the multiple elastic scattering theory [22], which can be applied to simulate elastic scattering events at high energies. Calculations were carried out for 44 photon energies ranging from 50 eV to 1 MeV, and the number of photon events simulated, N_p , was equal to 10^5 to ensure convergence of both the Fano factor and W value. The primary electrons were followed until their energies were less than the cut-off energy (twice the band gap), and a great number of electron histories were stored for further analysis.

3. Results and discussions

The number of electron–hole pairs and their distribution can be directly determined from the MC simulations. Fig. 1 shows the electron number distributions produced by 200 and 662 keV photons. It can be seen that the electron number distribution is

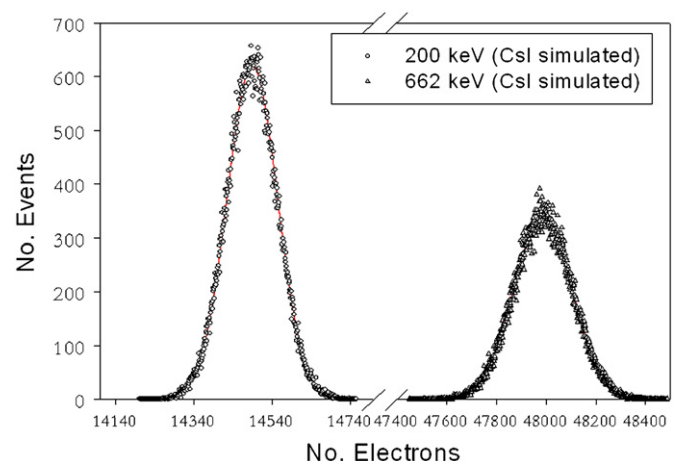


Fig. 1. Electron number distributions for photon energies of 200 and 662 keV.

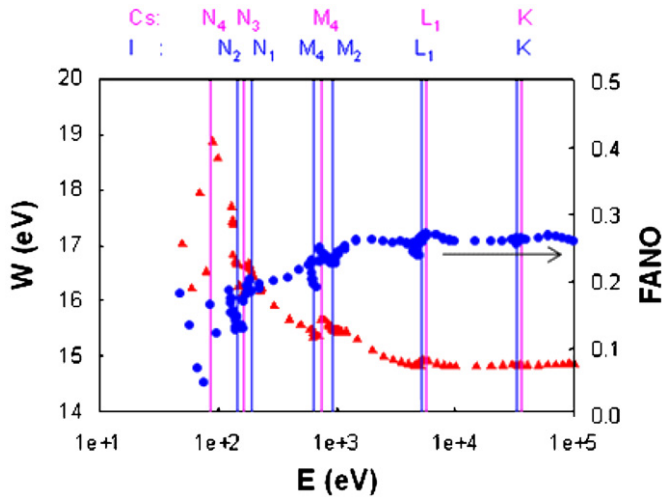


Fig. 2. Variation of the mean value of the electron–hole pair creation energy, W , and Fano factor, F , as a function of photon energy, E .

approximately a Gaussian distribution at these energies, while it appears asymmetric at low energies, particularly for energies less than 1 keV (not shown in Fig.1). The mean electron number is 14,485 and 48,152 for 200 and 662 keV, respectively. Using the electron number distributions, the parameters W and F can be calculated, and the results are shown in Fig. 2, where the shell edges are indicated. At energies lower than 10 keV, W generally decreases with increase in photon energy (from 19 to 15.2 eV), and exhibits a sawtooth variation, as observed previously in Si [10]. The discontinuities at all the shell edges follow the photoionization cross-sections. However, W tends to an asymptotic value of about 15.2 eV at higher energies, in good agreement with experimental values (12–20 eV) in CsI [23].

According to the model proposed by Lempicki and Wojtowicz [24], the measured light yield, L_y , the average number of scintillation photons generated by gamma-ray, can be expressed by

$$L_y = \frac{N_{e-h}}{E} SQ \quad (3)$$

where N_{e-h} is the number of electron–hole pairs created using MC simulations (including energy loss to optical phonons). S stands for transfer efficiency and Q luminescence quantum efficiency, which is often taken to be one. It is reasonable to write Eq. (4) as

$$L_y = SQ/W \quad (4)$$

The calculated value of W is about 15.2 eV per electron–hole pair, for incident energies larger than 10 keV; therefore, taking both S and Q as one, the maximum light yield, which corresponds to every electron–hole pair recombining to emit a photon, can be estimated to be 65,800 ph/MeV. This value is in reasonable agreement with the experimental range of values between 48,000 and 76,000 ph/MeV ([11] and references therein). It is of interest to note that W decreases with increase in energy up to 10 keV, leading to an increase in light yield. This may be correlated to the nonlinearity observed experimentally in CsI, i.e., initial rise in relative light yield with increase in incident energy [11]. Based on Eq. (4), the light yield can be estimated to be 52,600 ph/MeV at low energies and increases to 65,800 ph/MeV at higher energies. The present simulations suggest that the nonlinearity at low energies in CsI may be affected by some intrinsic properties of materials. Considering that exciton–exciton annihilation is an important mechanism, Moses et al. [25] suggested that the Birks equation could be used to describe the

rising part at low incident energies of the nonlinearity curve of inorganic scintillators. Recent computer simulations [11] confirmed that STE–STE annihilation can account for the rising part of the relative light yield curve at low incident energies for both pure CsI and cerium-doped LaBr₃. Therefore, it is likely that both the electron cascade and energy transport stages contribute to the nonlinearity of scintillator materials, but it is not clear to what extent. More work remains to be done to determine the possible contribution of different mechanisms to the nonlinearity of scintillation response.

The Fano factor, $F(E_p)$, increases with increase in photon energy to a value of 0.28 around 10 keV and remains constant at higher energies, as shown in Fig. 2. The initial increase of F with increase in incident energy may also affect the energy resolution of CsI, and represents an important intrinsic property. Similar to the behavior of W , discontinuities also appear at the shell edges. The Fano factor in CsI is generally higher than that in Si and Ge. It is well known that the creation of electron–hole pairs and their distributions at low energy are sensitive to the cross-sections of photoelectric absorption, and thus affect W and the Fano factor. In the present study, a large number of core shell ionization processes has been considered in CsI, which ranges from K to O shells. In Si or Ge, only K, L and M core shells are included. It is likely that the incident photon with an energy larger than a few hundreds of eV is able to create a fast electron and a vacancy at one of the core shells, which leaves the atom in an excited state. The atomic relaxation leads to the Auger electron/fluorescence photon emissions and shake-off electrons. It is possible that these secondary electrons can further result in core shell ionization. The mean number of electron–hole pairs created by photons and their distributions are sensitive to the number of energy loss channels. An increase in the number of energy loss channels could broaden the electron number distributions, leading to an increase in F .

As described in Section 1, the final scintillator yield strongly depends on the density of electronic excitations initially created in the track region. The understanding of nano-scale spatial distribution of electron–hole pairs will provide important information for large-scale simulations of electron–hole pair transport, electron–hole annihilation, and recombination of excited carriers, allowing us to explore the possible origins of nonlinearity. Fig. 3 shows a typical spatial distribution of electron–hole pairs created by a 10 keV incident photon in CsI. The incident photon interacts with a Cs atom by photoelectric absorption, which creates a L shell vacancy and a fast electron with a kinetic energy of 6 keV. This process leads the Cs atom to be in an excited state, and the atomic relaxation process that

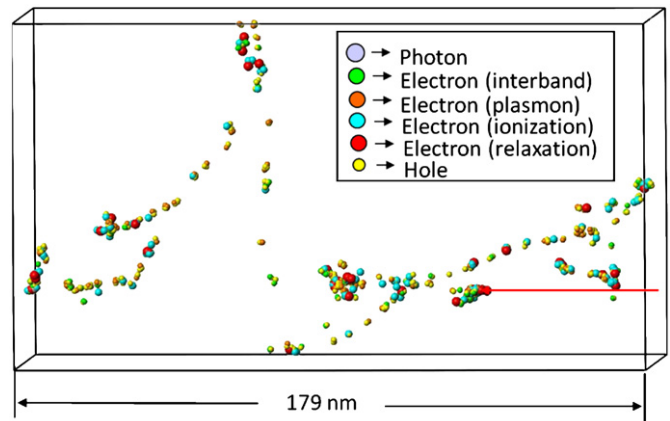


Fig. 3. Simulated spatial distribution of electron–hole pairs for a 10 keV photon event in CsI, where electrons and holes are distinguished by size and color, as indicated in legend.

follows results in the emission of another fast electron with a kinetic energy of about 3.45 keV, together with several low energy electrons. These two fast electrons further interact with the material to generate two tracks, as shown in Fig. 3. It can be seen that most electron–hole pairs are produced by core shell ionization and corresponding atomic relaxation processes. It is of great interest to note that all electron–hole pairs are distributed along the tracks of fast electrons. These electrons are incapable of generating further electron–hole pairs and their kinetic energies are generally less than the cut-off energy for terminating the simulation. However, these electrons are very mobile and can move away from the primary track without significant loss of their energies. Further simulations of thermalization effects on electron–hole pair diffusion are likely to lead to spatial distributions that are more diffuse as a result of electron–phonon scattering.

4. Conclusion

A Monte Carlo method has been extended to simulate various quantum mechanical processes for energy loss of photons and fast electrons and the spatial distribution of electron–hole pairs in CsI over the energy range from 50 eV to ~ 1 MeV. The intrinsic properties calculated are in good agreement with the limited experimental data. The decrease of W with increase in incident photon energy up to 10 keV may affect the initial rise in relative light yield that is experimentally observed for CsI. Also, the initial decrease in F for energies up to 10 keV may affect the energy resolution of CsI at low energies. The increase in the number of ionization channels for energy loss may explain the large Fano factor calculated for CsI, as compared with that in Si and Ge. The nano-scale spatial distributions demonstrate that electron–hole pairs are primarily distributed along fast electron tracks in CsI.

Acknowledgements

This research was supported by the National Nuclear Security Administration, Office of Nuclear Nonproliferation Research and Engineering (NA-22), of the US Department of Energy (DOE).

The computer simulations were performed in part using the Molecular Science Computing Facility in the William R. Wiley Environmental Molecular Sciences Laboratory, a national scientific user facility sponsored by the US DOE's Office of Biological and Environmental Research and located at Pacific Northwest National Laboratory (PNNL). PNNL is a multiprogram national laboratory operated by Battelle for the DOE under Contract DE-AC05-76RL01830.

References

- [1] P. Dorenbos, J.T.M. de Haas, C.W.E. van Eijk, *IEEE Trans. Nucl. Sci.* NS-42 (1995) 2190.
- [2] J.E. Jaffe, D.V. Jordan, A.J. Peurrung, *Nucl. Instr. and Meth. Phys. Res. A* 570 (2007) 72.
- [3] G. Bizarri, et al., *IEEE Trans. Nucl. Sci.* NS-56 (2009) 873.
- [4] P. Dorenbos, M. Marsman, C.W.E. Van Eijk, in: *Proceedings of the International Conference on Inorganic Scintillators and their Applications*, Delft University Press, The Netherlands, 1996, pp. 148–155.
- [5] M. Marsman, P. Dorenbos, C.W.E. Van Eijk, in: *Proceedings of the International Conference on Inorganic Scintillators and their Applications*, Delft University Press, The Netherlands, 1996, pp. 157–158.
- [6] S. Payne, et al., *IEEE Trans. Nucl. Sci.* NS-56 (2009) 2506.
- [7] G. Bizarri, et al., *Phys. Status Solidi (c)* 6 (2009) 97.
- [8] G. Bizarri, et al., *J. Appl. Phys.* 105 (2009) 044507.
- [9] G. Bizarri, et al., *J. Lumin.* 129 (2009) 1790.
- [10] F. Gao, et al., *Nucl. Instr. and Meth. Phys. Res. A* 579 (2007) 292.
- [11] S. Kerisit, et al., *J. Appl. Phys.* 105 (2009) 114915.
- [12] P. Dorenbos, *Phys. Status Solidi (a)* 202 (2005) 195.
- [13] D.E. Cullen, J.H. Hubbell, L. Kissel, *EPDL97 The Evaluated Data Library, '97 Version*, Report UCRL-50400, vol. 6, rev. 5, 1997.
- [14] R. Ribberfors, *Phys. Rev. A* 27 (1983) 3061.
- [15] M.J. Berger, J.H. Hubbell, *XCOM: Photon Cross Section on a Personal Computer*, Report NBSIR 87-3597, National Bureau of Standards, Gaithersburg, MD, 1987.
- [16] T.A. Carlson, C.W. Nestor, *Phys. Rev. A* 8 (1973) 2887.
- [17] R. Mayol, F. Salvat, *J. Phys. B: At. Mol. Opt. Phys.* 72 (1990) 2117.
- [18] J. Llacer, E.L. Garwin, *J. Appl. Phys.* 40 (1969) 2766.
- [19] J.N. Bradford, S. Woolf, *J. Appl. Phys.* 70 (1991) 490.
- [20] F. Salvat, J.M. Fernández-Varea, *Nucl. Instr. and Meth. Phys. Res. B* 63 (1992) 255.
- [21] F. Salvat, R. Mayol, *Comput. Phys. Commun.* 74 (1993) 385.
- [22] E. Benedito, J.M. Fernandez-Varea, F. Salvat, *Nucl. Instr. and Meth. B* 174 (2001) 91.
- [23] S. Sasaki, et al., *Jpn. J. Appl. Phys.* 45 (2006) 6420.
- [24] A. Lempicki, A.J. Wojtowicz, *J. Lumin.* 60&61 (1994) 942.
- [25] W.W. Moses, et al., *IEEE Trans. Nucl. Sci.* NS-55 (2008) 1049.

Formation, stability, and mobility of self-trapped excitations in NaI and NaI_{1-x}Tl_x from first principles

M. P. Prange,¹ R. M. Van Ginhoven,² N. Govind,³ and F. Gao¹¹*Fundamental and Computational Sciences Directorate, Pacific Northwest National Laboratory, Richland, Washington 99352, USA*²*Energy and Environment Directorate, Pacific Northwest National Laboratory, Richland, Washington 99352, USA*³*William R. Wiley Environmental Molecular Sciences Laboratory, Pacific Northwest National Laboratory, Richland, Washington 99352, USA*

(Received 9 August 2012; revised manuscript received 4 February 2013; published 4 March 2013)

We study the formation, mobility, and stability of self-trapped excitons (STE) and self-trapped holes and electrons in NaI and NaI(Tl) using embedded cluster hybrid density functional theory calculations. This method employs an array of classical charges to provide an environment simulating the interior of an ionic solid in which the electronic structure of a modestly sized quantum-mechanical cluster is computed including nonlocal exchange effects which are necessary to describe localized excitations in NaI. In contrast with previous models, we find that both carriers in pure NaI have similar mobilities, with an activation energy of ~ 0.2 eV. We propose an alternate interpretation including a new migration mechanism for the STE. In Tl-doped material excitons preferentially trap at dopants, inducing off-center distortions that have a structure unlike an STE and provide a mechanism for light emission at multiple wavelengths.

DOI: [10.1103/PhysRevB.87.115101](https://doi.org/10.1103/PhysRevB.87.115101)

PACS number(s): 71.35.Cc, 71.35.Aa, 72.20.Ee, 72.20.Jv

I. INTRODUCTION

Recent progress in multiscale modeling of scintillating radiation detectors shows great promise.¹ Such efforts, however, require a *quantitative* understanding of all relevant microscopic processes which can then be correctly parametrized in meso- or macroscale models. While some quantities are accessible by measurement, the picture is often incomplete and sometimes qualitatively incorrect. This paper presents results using first-principles calculations that capture important details of the microscopic physics of NaI that are crucial to understanding and modeling of detector performance.

Thallium-doped NaI is of particular interest because it is widely used and the standard material against which new scintillators are compared.² In scintillation radiation detection, highly energetic radiation causes a cascade of secondary excitations in the crystal. Some of these excitations ultimately relax by the emission of visible light which is measured as a proxy for the energy of the incident radiation. The energy resolution of scintillators is limited by the nonproportionality of light yield to incident energy.³

Despite decades of experimental^{4–8} and theoretical^{5,9–12} study, microscopic understanding of the competing modes of energy transport and conversion in alkali halides is incomplete, and the interaction of energy carriers with dopants is only partially understood. Experimental and theoretical studies show that the luminescence efficiency depends on the spatial distribution of the secondary excitations, with higher densities of excitations producing fewer luminescence photons per unit deposited energy for low excitation energies.^{3,13–15} This falloff of luminescence efficiency at low energies and high excitation densities is common in scintillators but especially pronounced in NaI(Tl). It is attributed to quenching of the secondary excitations by nonradiative processes that leave the energy carried by a pair (or more, for higher order processes) of secondary excitations in the vibrational modes of the scintillator and hence unavailable for luminescence.

We address the formation and diffusion of holes and excitons in pure and Tl-doped NaI, which are the important

secondary excitations for luminescence. Self-trapped holes (STHs) (V_k centers) consist of a missing electron in a valence band and an accompanying strong lattice distortion, and a self-trapped exciton (STE) can be thought of as an STH surrounded by a bound electron. In both cases the lattice relaxation in the pure material resembles the formation of an I_2^- ion within the bulk crystal¹⁶ with two I atoms moving markedly together. Such self-trapped excitations were qualitatively explained theoretically by the 1970s,^{17,18} but improvement of theoretical understanding is ongoing, and a fully detailed description has not yet been achieved.^{19,20}

During a scintillation event in NaI or NaI(Tl), these self-trapped excitations are initially created in a track, the structure of which depends on the particular exciting radiation. After creation, the self-trapped excitations execute diffusive motion until their decay. In the Tl-doped material, the dominant mechanism for light emission is STE capture by a Tl dopant (activator) followed by photon emission by the Tl. In the absence of such activator sites, the dominant process for light emission is direct radiative decay of STEs. The dominant quenching mechanism is STE-STE annihilation, in which two excitons collide and are destroyed. In both cases, light emission involves a single STE and hence depends linearly on the STE density while the quenching mechanism, which requires (at least) a binary collision, depends on higher powers of the excitation density leading to decreased luminescence efficiency at high excitation densities. Meanwhile, STHs and free carriers are also produced in the track. They can combine to form excitons (including STEs) or luminescence photons. Thus, a detailed understanding of scintillator performance in these systems requires understanding of the motion of STEs, free electrons, and STHs in order to predict the time evolution of the populations of each type of excitation and their ultimate fates. Various attempts have been made to describe scintillation efficiency by modeling the time and spatial dependence of secondary excitations using Monte-Carlo approaches, models based on rate equations, or ones based on diffusion equations. These are reviewed in Ref. 13. All these approaches are

limited by the paucity of knowledge regarding the microscopic dynamics of low-energy excitations.

Previously proposed models,^{15,21} based on optical experiments,^{22,23} assumed a highly mobile STE and a slower STH, while we find that in pure NaI both carriers have similar mobilities, with an activation energy of ~ 0.2 eV. We propose an alternate interpretation, in which an electron hops from an STE to an STH at a different site, effectively exchanging the STE and STH. Our calculations suggest this migration mechanism should have a much lower barrier, consistent with measurements. Excitons migrating via this mechanism are likely to exhibit dynamics with different dependencies on temperature and local excitation density than excitons migrating by the conventional hopping mechanism. Importantly for theories of scintillation efficiency, STEs hopping by this mechanism can-not participate directly in STE-STE annihilation, since the destination site for this mechanism must contain an STH. Hence the existence of two different hopping barriers has implications for detector nonproportionality.

As is well known, accurate calculations of localized states in alkali halides are challenging because density functional theory (DFT) using semilocal exchange-correlation potentials often provides a qualitatively incorrect picture [e.g., neither STEs nor STHs are stable compared to undistorted structures in NaI (Ref. 24)]. To circumvent this problem we employ hybrid DFT with nonlocal exchange.

Most previously reported calculations on alkali halide systems (e.g., Refs. 25, 10, and 11) have been performed using some form of pure Hartree Fock (HF) theory. Notable exceptions are Derenzo and Weber²⁶ and Rivas-Silva *et al.*²⁷ who used MP2 and QCISD levels of theory, respectively, to calculate emission energies. These previous works relied on small or symmetry constrained models to improve calculation tractability or to explore a specific proposed geometry. Since confinement effects limit the deformations available, small clusters discourage localized states which involve such distortion or lattice polarization. On the other hand, the use of pure HF, which completely neglects the correlation energy, favors localized states. Hence there is the possibility that these two errors partially cancel leading to qualitatively correct results. This work (with as many as 136 *ab initio* atoms and no constraints on the symmetry of the deformation) is a substantial improvement over previous efforts in this area.^{10,11,25-27}

II. COMPUTATIONAL METHODS

As in past work,^{11,17,18,28,29} we use an embedded cluster method to facilitate tractable calculations. Our calculations include a large ($\sim 10\,000$) array of fixed point charges, located at lattice positions of the undistorted crystal. This array provides an electrostatic potential which closely reproduces the classical Ewald potential of the perfect crystal throughout a central region in the interior of the array. The atoms on surface of the cluster are fixed throughout the calculation, and the interior atoms are allowed to relax. A schematic diagram of a cluster model is shown in Fig. 1.

Within the quantum-mechanical region, the electronic structure was computed by means of hybrid DFT using CRENBL ECP (Ref. 31) basis sets for Na and I and Stuttgart RLC basis sets³² for TI. Unless otherwise stated,

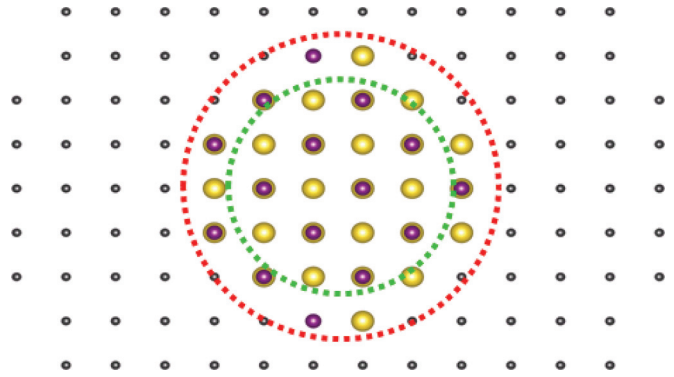


FIG. 1. (Color online) Cutaway view of embedded cluster model of NaI. Classical charges are shown in gray, Na atoms in gold, and I atoms in purple. In this model there are 16 248 charges and 136 atoms. Atoms within the inner circle are allowed to relax during geometry optimization, while those atoms between the circles are held fixed. This image and all images in this paper depicting structures were created using VESTA (Ref. 30).

the cluster models contained 136 quantum-mechanical atoms. The positions of 51 of these were varied in the optimizations. For each Na atom in the cluster two electrons were treated by means of an effective core potential. For each I, 46 electrons were so treated. The calculations presented here are scalar ones that do not include the spin-orbit interaction. The Becke half-and-half³³ (BHH) exchange-correlation potential was used. Unless otherwise stated, calculations were carried out using the NWCHEM code.³⁴

III. RESULTS

A. Pure NaI

To characterize localized excitations we constrained the number of spin-up and spin-down electrons and searched for the nuclear coordinates that minimized the total energy of the cluster model subject to these constraints. The results of such a procedure are the geometry and energy of the lowest energy state of each type: a doublet of charge $+1$ in the case of the STH and a neutral triplet in the STE case. We find that on-center self-trapped holes and excitons are stable in NaI compared to delocalized states, but electrons do not self-trap in pure NaI clusters in our calculations even for pure HF which is known to favor self-trapped states.²⁰

In our models, the two I atoms participating in the STE are separated by 3.36 Å, close to the measured (3.23 Å)³⁵ and theoretical (3.31 Å) isolated I_2^- bond length and far from the I-I separation in the undistorted NaI crystal (4.58 Å). Our isolated I_2^- bond length is in good agreement with other calculations,³⁶ and the actual STE I-I separation is also in agreement with other theoretical results.³⁷ The energy of the STE is calculated to be 5.68 eV above the (singlet) ground state of the undistorted crystal and 0.7 eV below the lowest energy triplet state of the undistorted crystal. The measured excitation energy is 5.61 eV.³⁸ In addition, we calculated an emission energy of 4.27 eV for the STE, in good agreement with the experimentally measured value of 4.207 eV.³⁹ We also find an on-center STH which resembles the STE (3.38 Å I-I separation) with the electron removed.

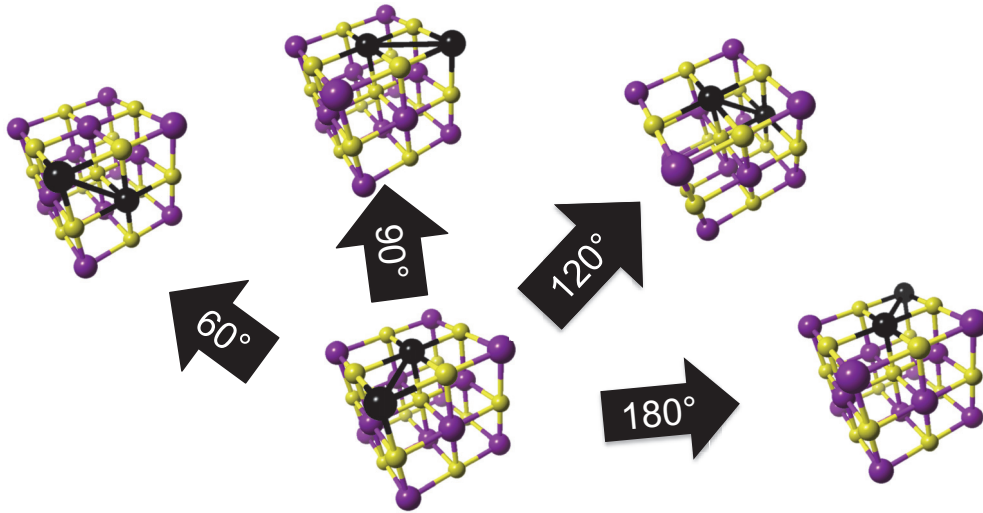


FIG. 2. (Color online) The four near-neighbor hops available to the STE or STH in NaI.

Our calculations estimate the energy of this STH to be 0.50 eV lower than a delocalized hole in the undistorted crystal.

Assuming the conventional picture in which self-trapped excitations migrate via the transfer of lattice distortion and spin density between adjacent lattice sites, we calculated the energy barrier for hopping of the STE and STH in NaI for each of the four possible hop angles between iodine neighbor pairs in the rocksalt structure which are depicted in Fig. 2.

For each hop and type of self-trapped excitation, cluster models were relaxed with the excitation positioned at either end of the jump. The transition state was estimated by relaxing the interior atoms of the cluster except the two I atoms directly participating in the self-trapped excitation (the active halogens) from a starting geometry calculated as the average of the geometries before and after the jump. We have reported this energy difference as the migration barrier in Table I. For all STH jumps, the hole orbital at the transition state is shared among the three halogens involved in the jump. Most of the orbital resides on the central I that participates in the STH before and after the jump, with smaller but significant contributions from the other two iodines involved. Previous work in other alkali halide systems has found similar transition states.⁴⁰ Shluger and co-workers⁴⁰ postulated the existence of a “one-center” self-trapped hole state near the transition state for the 60° STH jump. They found this state to be unstable; we find the same conclusion for our system in the present work. The energy difference between a one-center trapped hole and the STH provides an upper bound for the transition barrier and provides an explanation for the nearly identical

barriers since any of the hops could be accomplished by first transitioning to the one-center state which appears to be adiabatically connected to all the STH states in which the single center participates.

We show the spin density for the relaxed STH and for the transition state of the 120° hop in Fig. 3. In our simulations, the behavior of the hole in the STE hops is very similar to that of the hole in the corresponding STH hops. The STE electron becomes delocalized in the transition state for all hop angles in our clusters.

Popp and Murray⁸ estimated a barrier of 0.18 eV for the 60° STH jump, in reasonable agreement with our value of 0.225 eV. On the other hand, experimental estimates of the STE hopping barrier are much lower. For example, Nagata and co-workers^{22,23} reported 0.07 eV for Tl-doped NaI. The magnitude of this barrier is directly related to the thermally activated mobility of the STE, and our results suggest that the conventional picture of the low-energy kinetics of STEs should be reexamined. In particular, we expect, based on our calculations, the STE and STH to have nearly identical mobilities. The lower barrier ascribed to the STE can be attributed to the migration of electrons hopping from an STE to a nearby STH. Since the geometries of the STH and STE are similar, we expect the barrier for such a hop to be low. In fact the energy gained by relaxing the neutral triplet state starting in the STH geometry (so that the final configuration is an STE) is 0.02 eV. The hopping barrier can be expected to be of the same order of magnitude.

B. Tl impurities

NaI is commonly doped with Tl, which substitutes for Na at a lattice site to create a light-emitting center. The transfer of energy from diffusing self-trapped excitations to these luminescence centers, while believed to play a significant role in scintillator performance, is not well understood. To investigate this process, we simulated Tl impurities in our models. The lowest energy singlet state for our clusters involves only modest displacements around the Tl to accommodate the larger size of the dopant compared to the Na atom it replaces.

TABLE I. Calculated migration barriers for STH and STE in pure NaI.

Hop angle (deg)	STH barrier (eV)	STE barrier (eV)
60	0.225	0.199
90	0.285	0.267
120	0.241	0.274
180	0.223	0.258

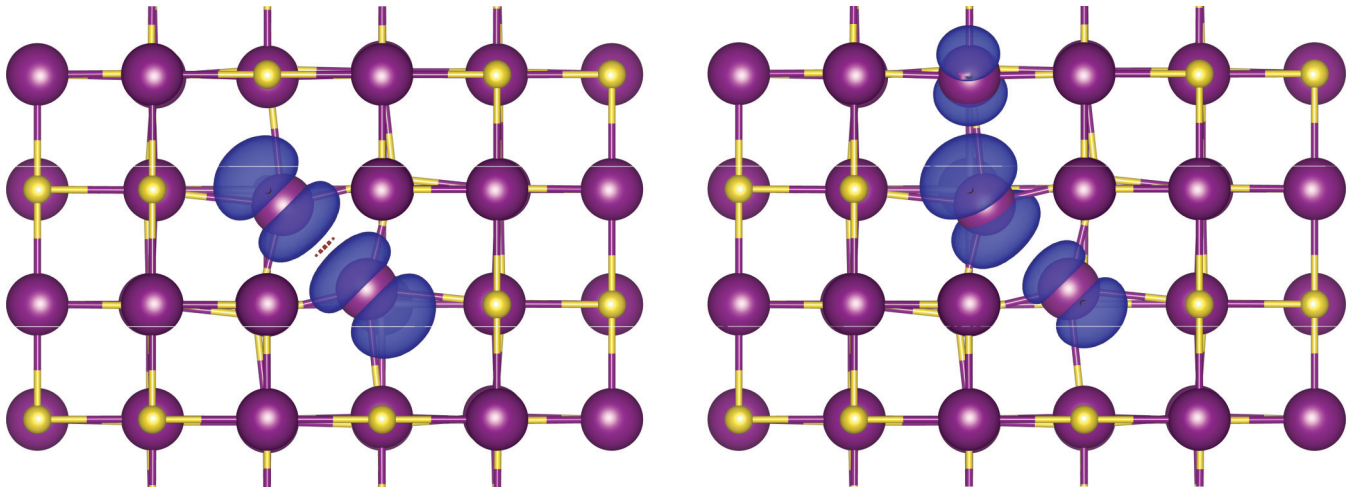


FIG. 3. (Color online) Spin density isosurfaces drawn at 0.001 electrons/bohr³ around an STH (left panel) and the transition state for a 120° STH jump (right panel).

By optimizing the geometry from various starting points and spin populations, we find a rich collection of stable trapped excitations from this state including two distinct neutral triplet excitons as well as a single trapped hole and a trapped electron.

The two nearly degenerate (the energy of the edge configuration is higher by 0.04 eV in our model) triplet excitations are depicted in Fig. 4. We note that, unlike the bulk self-trapped excitations, the TI-trapped excitons are stable in LDA and

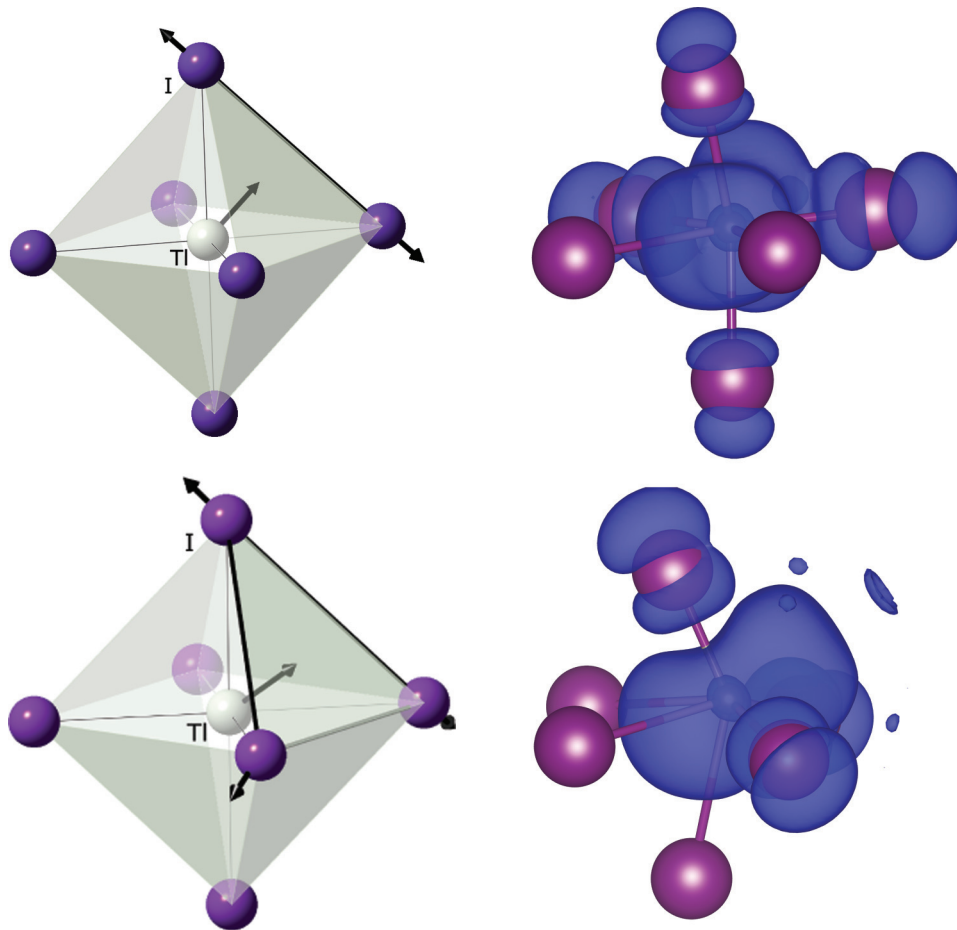


FIG. 4. (Color online) The left column shows schematic diagrams of the displacements relative to a perfect NaI crystal lattice of a TI impurity participating in two different exciton states. The right column shows the optimized coordinates of the coordinating octahedron that holds the TI impurity along with a spin density isosurface drawn at 0.001 electrons/bohr³.

PBE theories, although PBE reverses the relative energies of the two excitons. In bulk NaI, each Na cation is octahedrally coordinated by I anions. The TI in the singlet ground state sits similarly in the center of a nearly regular octahedron with I at each vertex. The relaxations accompanying the trapping of the triplet states involve the movement of the TI towards either an edge or face of the octahedron which expands to accommodate the TI. In both cases the spin density associated with the triplet exciton is localized on the TI and the accommodating I atoms (cf. Fig. 4). The orbitals involved in the excitons have s character around the TI and p character around the I atoms. Calculations of the barrier between the two TI-trapped excitons were done using cluster models. Additionally, we used the nudged elastic band method as implemented in the SEQUEST code^{41,42} to estimate the barrier. Both LDA⁴³ and PBE⁴⁴ functionals were used. These calculations all indicate that the barrier is very low and that the TI can rattle around nearly freely in the octahedron formed by the nearest iodines.

We found these TI-trapped triplet states to be stable compared to a (bulk) STE near a singlet TI by ~ 0.25 eV and hence expect diffusing STEs to be trapped when they encounter TI impurities. Even though the excited states are essentially degenerate, the excitation depicted in Fig. 4(a) has a luminescence energy of 3.46 eV, while the excitation depicted in (b) has a luminescence energy of 2.85 eV due to the slope of the ground-state potential energy surface between the excited state geometries. These calculated transition energies compare well with low-temperature experiments on NaI(TI)³⁹ finding bands centered at 3.76 and 2.95 eV. In other doped alkali halide systems these A_T and A_X emissions have similar structure.^{45,46}

The off-site displacement of the TI center is due to broken symmetry on the excited state potential energy surface induced by the presence of an electron with p orbital character. We expect the same type of distortion to occur for the triplet exciton, the trapped electron (TI⁰), and the singlet excited state (TI*).

We propose that the localized triplet states depicted in Fig. 4 play a role in the transfer of energy from free, diffusing STEs to fixed luminescence centers by capturing the spin density associated with the STE and thereby destroying the STE. The distortion around the TI, which cannot migrate, replaces the

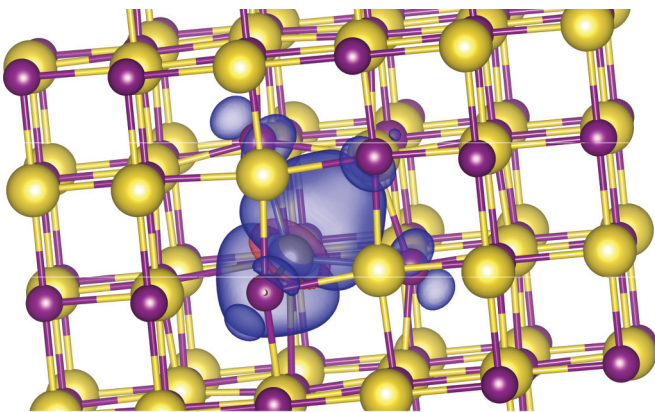


FIG. 5. (Color online) Spin density isosurface drawn at 0.0005 electrons/bohr³ in a 136-atom cluster containing a TI⁰.

TABLE II. Bond lengths and relaxation energies (energy difference between positively charged clusters in undistorted and fully relaxed geometries) for the STH in pure NaI for several cluster models of different sizes. BHH xc was used for these calculations, so the first line of this table and Table IV are identical. The bond lengths are in Å and the energies in eV.

Cluster size	Bond length	Relaxation energy
48	3.383	0.50
80	3.371	0.69
136	3.357	0.72

STE. We have succeeded in relaxing a lattice STE in a layer adjacent to a TI impurity's surrounding octahedron, hence we estimate the radius for capture of a diffusing STE by a TI impurity to be of the order of the lattice constant.

Finally, we have found a shallow but stable minimum in which an electron is localized on a TI impurity (i.e., a TI⁰). The relaxation around this state resembles the exciton in which the octahedron edge lengthens to accommodate the displacement of the TI (the top row of Fig. 4). This TI⁰ state is only 0.1 eV lower in energy than a delocalized electron in the relaxed singlet (TI⁺) geometry. The spin density of the TI⁰ state is depicted in Fig. 5.

IV. DISCUSSION

To explore the dependence of the physics of self-trapped excitations on cluster size and exchange-correlation treatment, we varied each approximation in baseline calculations of the STH. Table II shows the bond length of the I₂⁻ in the STH and the relaxation energy (energy gained by allowing the I₂⁻ to form in a positively charged cluster) for three cluster sizes. In Table III we show various energy differences in neutral cluster models of the same size as those used in Table II. We list the energy difference between the lowest unoccupied orbital (LUMO) and the highest occupied orbital (HOMO) of the singlet configuration at the relaxed singlet (i.e., bulklike ground state) geometry. We also list the excitation energy which is computed as the difference between the total energy of the relaxed triplet (i.e., STE) geometry and the total energy of the relaxed singlet (ground state). Finally we list luminescence energies which were calculated as the difference between the triplet and singlet potential energy surfaces at the relaxed triplet (STE) geometry. From these convergence studies, we estimate the errors due to finite cluster size in energies are ~ 0.1 eV and in bond lengths are ~ 0.05 Å.

TABLE III. Calculated energy differences (in eV) for neutral cluster models of different sizes. We show singlet HOMO-LUMO gaps and excitation and luminescence energies for the STE.

Cluster size	HOMO-LUMO	Excitation	Luminescence
48	7.39	5.74	4.49
80	7.23	5.57	4.17
136	7.16	5.68	4.27
Experiment		5.61 (Ref. 38)	4.207 (Ref. 39)

TABLE IV. Bond length, 60° migration barriers, and relaxation energies (energy difference between positively charged clusters in undistorted and fully relaxed geometries) for the STH in pure NaI for several xc functionals which are described further in the text. All calculations in this table used identical 48-atom models. The bond lengths are in Å and the energies in eV.

Functional	60° barrier	Bond length	Relaxation energy
BHH	0.225	3.383	0.50
HF	0.193	3.370	1.55
B3LYP	0.150	3.383	-0.04
Becke 0.325 and 0.625	0.140	3.423	0.18

In Table IV we present the 60° migration barrier, bond length, and relaxation energy for the STH computed with several exchange-correlation (xc) functionals but otherwise identical cluster models. In addition to BHH (Ref. 33) (used for all other results in this paper), results obtained using B3LYP,⁴⁷ HF, and a modified BHH in which the fraction of HF exchange is reduced from 1/2 to 0.325 are tabulated. The bond length is rather insensitive to xc treatment, but, surprisingly, the migration barrier is smaller in the HF theory than in the BHH one. The relaxation energy, however, is monotonic in the fraction of HF exchange included in the otherwise semilocal functional. In fact, the STH, while locally stable, is higher in energy than the undistorted structure in the B3LYP theory. Based on these calculations it is our opinion that in the case of ionic solids such as the alkali halides, the uncertainty in the calculated energies due to the exchange-correlation treatment is larger than that due to finite cluster size effects.

V. CONCLUSION

We have studied trapped excitations in NaI with *ab initio* hybrid DFT using large systems. We find an on-center STE and STH in the pure material and excitons trapped on TI impurities in NaI(Tl). Our calculations are in very good agreement with available experimental data and largely consistent with the conventional picture of scintillation in NaI except for the STE hopping mobility, for which we find a much higher barrier (close to that for the STH) in our calculations. We suggest further work to validate the barriers and energy levels published here as well as a theoretical description of other microscopic properties outside the scope of this paper, such as STE-STE annihilation, and STE radiative and nonradiative decay lifetimes. It is also our hope that models of scintillation efficiency, parametrized with *ab initio* results such as the ones presented here and including both STE migration mechanisms be constructed and tested.

ACKNOWLEDGMENTS

This research was supported by the National Nuclear Security Administration, Office of Nuclear Nonproliferation Research and Engineering (NA-22), of the U.S. Department of Energy (DOE). A portion of this research was performed using EMSL, a national scientific user facility sponsored by the Department of Energy's Office of Biological and Environmental Research and located at Pacific Northwest National Laboratory. Additionally, a portion of the research was performed using PNNL Institutional Computing at Pacific Northwest National Laboratory.

¹Z. Wang, Y. Xie, B. D. Cannon, L. W. Campbell, F. Gao, and S. Kerisit, *J. Appl. Phys.* **110**, 064903 (2011).

²G. F. Knoll, *Radiation Detection and Measurement*, 3rd ed. (Wiley, New York, 2000).

³R. Devanathan, L. R. Corrales, F. Gao, and W. Weber, *Nucl. Instrum. Methods Phys. Res. A* **565**, 637 (2006).

⁴J. C. Phillips, *Phys. Rev.* **136**, A1705 (1964).

⁵R. T. Williams, K. S. Song, W. L. Faust, and C. H. Leung, *Phys. Rev. B* **33**, 7232 (1986).

⁶K. Teegarden and G. Baldini, *Phys. Rev.* **155**, 896 (1967).

⁷J. E. Eby, K. J. Teegarden, and D. B. Dutton, *Phys. Rev.* **116**, 1099 (1959).

⁸R. Popp and R. Murray, *J. Phys. Chem. Solids* **33**, 601 (1972).

⁹C. H. Leung and K. S. Song, *J. Phys. C* **12**, 3921 (1979).

¹⁰A. L. Shluger, N. Itoh, V. E. Puchin, and E. N. Heifets, *Phys. Rev. B* **44**, 1499 (1991).

¹¹V. E. Puchin, A. L. Shluger, K. Tanimura, and N. Itoh, *Phys. Rev. B* **47**, 6226 (1993).

¹²C.-R. Fu, L.-F. Chen, and K. S. Song, *J. Phys.: Condens. Matter* **11**, 5517 (1999).

¹³W. Moses, G. Bizarri, R. T. Williams, S. Payne, A. Vasil'ev, J. Singh, Q. Li, J. Grim, and W. Choong, *IEEE Trans. Nucl. Sci.* **59**, 2038 (2012).

¹⁴R. B. Murray and A. Meyer, *Phys. Rev.* **122**, 815 (1961).

¹⁵S. Payne, N. Cherepy, G. Hull, J. Valentine, W. Moses, and W.-S. Choong, *IEEE Trans. Nucl. Sci.* **56**, 2506 (2009).

¹⁶R. T. Williams and K. S. Song, *J. Phys. Chem. Solids* **51**, 679 (1990).

¹⁷A. M. Stoneham, *J. Phys. C* **7**, 2476 (1974).

¹⁸K. S. Song, A. M. Stoneham, and A. H. Harker, *J. Phys. C* **8**, 1125 (1975).

¹⁹N. Itoh and A. M. Stoneham, *Materials Modification by Electronic Excitation* (Cambridge University Press, Cambridge, UK, 2001).

²⁰A. M. Stoneham, *Modell. Simul. Mater. Sci. Eng.* **17**, 084009 (2009).

²¹S. Kerisit, K. M. Rosso, B. D. Cannon, F. Gao, and Y. Xie, *J. Appl. Phys.* **105**, 114915 (2009).

²²S. Nagata, K. Fujiwara, and H. Nishimura, *J. Lumin.* **47**, 147 (1990).

²³H. Nishimura and S. Nagata, *J. Lumin.* **40-41**, 429 (1988).

²⁴J. L. Gavartin, P. V. Sushko, and A. L. Shluger, *Phys. Rev. B* **67**, 035108 (2003).

²⁵R. C. Baetzold and K. S. Song, *J. Phys.: Condens. Matter* **3**, 2499 (1991).

²⁶S. E. Derenzo and M. J. Weber, *Nucl. Instrum. Methods Phys. Res. A* **422**, 111 (1999).

²⁷J. F. Rivas-Silva, L. Rodríguez-Merino, M. Berrondo, and A. Flores-Riveros, *Int. J. Quantum Chem.* **77**, 785 (2000).

²⁸P. V. Sushko, A. L. Shluger, and C. A. Catlow, *Surf. Sci.* **450**, 153 (2000).

²⁹N. Govind, P. Sushko, W. Hess, M. Valiev, and K. Kowalski, *Chem. Phys. Lett.* **470**, 353 (2009).

- ³⁰K. Momma and F. Izumi, *J. Appl. Crystallogr.* **44**, 1272 (2011).
- ³¹L. F. Pacios and P. A. Christiansen, *J. Chem. Phys.* **82**, 2664 (1985).
- ³²F. Weigend and R. Ahlrichs, *Phys. Chem. Chem. Phys.* **7**, 3297 (2005).
- ³³A. D. Becke, *J. Chem. Phys.* **98**, 1372 (1993).
- ³⁴M. Valiev, E. Bylaska, N. Govind, K. Kowalski, T. Straatsma, H. V. Dam, D. Wang, J. Nieplocha, E. Apra, T. Windus *et al.*, *Comput. Phys. Commun.* **181**, 1477 (2010).
- ³⁵E. C. M. Chen and W. E. Wentworth, *J. Phys. Chem.* **89**, 4099 (1985).
- ³⁶A. Md Asaduzzaman and G. Schreckenbach, *Theor. Chem. Acc.* **122**, 119 (2009).
- ³⁷P. E. Cade, A. M. Stoneham, and P. W. Tasker, *Phys. Rev. B* **30**, 4621 (1984).
- ³⁸A. Song and R. T. Williams, *Self-Trapped Excitons*, Springer Series in Solid-State Sciences (Springer, New York, 1996).
- ³⁹P. A. Rodnyi, *Physical Processes in Scintillators*, 1st ed. (CRC Press, Boca Raton, 1997).
- ⁴⁰A. L. Shluger, L. N. Kantorovich, E. N. Heifets, E. K. Shidlovskaya, and R. W. Grimes, *J. Phys.: Condens. Matter* **4**, 7417 (1992).
- ⁴¹A. E. Mattsson, P. A. Schultz, M. P. Desjarlais, T. R. Mattsson, and K. Leung, *Modell. Simul. Mater. Sci. Eng.* **13**, R1 (2005).
- ⁴²P. A. Schultz, SEQQUEST code, <http://dft.sandia.gov/Quest>.
- ⁴³J. P. Perdew and A. Zunger, *Phys. Rev. B* **23**, 5048 (1981).
- ⁴⁴D. R. Hamann, *Phys. Rev. B* **40**, 2980 (1989).
- ⁴⁵A. Fukuda, *Phys. Rev. B* **1**, 4161 (1970).
- ⁴⁶L. S. Dang, Y. M. d'Aubigné, R. Romestain, and A. Fukuda, *Solid State Commun.* **26**, 413 (1978).
- ⁴⁷A. D. Becke, *J. Chem. Phys.* **98**, 5648 (1993).

Off-center Tl and Na dopant centers in CsI

R M Van Ginhoven¹ and P A Schultz²

¹ Pacific Northwest National Laboratory, Richland, WA 99352, USA

² Sandia National Laboratories, Albuquerque, NM, USA

E-mail: Renee.VanGinhoven@pnnl.gov and paschul@sandia.gov

Received 19 June 2013, in final form 28 August 2013

Published 6 November 2013

Online at stacks.iop.org/JPhysCM/25/495504

Abstract

We use density functional theory calculations to characterize the electronic and structural properties of the Tl and Na dopant centers in CsI. We find that the Tl and Na centers can accept one or two electrons and couple to long-range relaxations in the surrounding crystal lattice to distort strongly off-center to multiple distinct minima, even without a triplet excitation. The long-range distortions are a mechanism to couple to phonon modes in the crystal, and are expected to play an important role in the phonon-assisted transport of polarons in activated CsI and subsequent light emission in this scintillator.

(Some figures may appear in colour only in the online journal)

1. Introduction

There has been considerable interest in recent years in the development of new materials and optimization of current materials for use as scintillating radiation detectors. Signal production in scintillating detectors involves conversion of cascade energy into optical emission. This is a relatively slow process involving transport of carriers to luminescent centers, in competition with other processes that dissipate a portion of the initial energy. Prediction of the performance of new or improved materials requires an understanding of these transport processes. Cesium iodide doped with thallium or sodium (CsI:Tl, CsI:Na), is widely used as an effective scintillating material. Despite many careful studies over several decades [1], the mechanisms for energy transport and light emission, and the role of the dopant atoms in this material are not well understood. Previous cluster-based *ab initio* calculations of Tl in CsI and NaI clusters have demonstrated the need for relatively large systems to adequately describe the surrounding lattice response, but only examined symmetric lattice distortions [2].

We use density functional theory (DFT) to investigate the electronic and structural properties of Na and Tl dopants in CsI, along with related intrinsic defects, to elucidate the behavior of these dopants. It is well established that standard DFT using semilocal exchange–correlation potentials does not correctly describe the expected energy carriers in the pure

alkali halides, either self-trapped holes, also known as V_k centers, or self-trapped excitons (STE) [3, 4]. However, we are not attempting to model the STE or V_k center. For defects with well-localized electronic states, such as the vacancy and dopant impurity point defects we investigate here, we expect a semilocal description to provide a fully adequate and decisive description of the defect structure and behavior.

In addition to having a stable neutral state and a localized triplet excitation, a defect-trapped exciton (DTE), we find that each dopant center can accept one or two electrons. All of the charge states of substitutional Tl and Na distort off-center, and couple to surprisingly long-range distortions in the surrounding crystal lattice. Three symmetry-distinct distortions are found, into the 001-face, into the 110-edge, and along the 111-bond directions, and are stable even without having trapped a local triplet excitation (exciton). These distortions involve long-range lattice deformations that would naturally couple to phonon modes, and include local structural deformations that would facilitate capture and transport of excitons. This provides a novel mechanism to explain the emission behavior activated by the dopants.

2. Computational methods

The density functional supercell calculations for CsI:Tl were performed with the periodic pseudopotential SEQQUEST code [5]. The spin-polarized local-density approximation

(LDA) calculations used the form parameterized by Perdew and Zunger [6] and the generalized gradient functional used was formulated by Perdew *et al* [7]. Carefully optimized [8] norm-conserving pseudopotentials [9] (PP) were used for all atoms: the cesium PP included its semicore $5p^6$ electrons among the valence electrons along with a non-linear core correction [10] ($R_{nlc} = 2.5$ bohr), and the [core] $5p^6 6s^{0.1}$ atom used a hardened d-potential ($R_l = 1.4$) for its local potential; an otherwise standard $s^2 p^5$ iodine PP used a hardened $l = 3$ ($R_l = 1.2$) potential for the local potential as the optimal $l = 2$ potential ($R_l = 1.57$) proved too soft for good transferability; and the $5d^{10}$ shell of thallium was placed in the valence and used as the local potential, while its p-potential was tuned ($R_l = 1.57$) for better transferability. The double-zeta plus polarization basis sets were constructed of contracted Gaussian functions.

We used the local moment countercharge method to solve the Poisson equation for charged supercells [11] and extrapolated to bulk asymptotic limits using the finite defect supercell model [12]. Bulk screening energy outside the supercell [12] was evaluated using the experimental static dielectric constant [13], 5.65, and an internal screening depth of 1.8 bohr (~ 0.9 Å). The numerical results are not highly sensitive to these values, and the convergence of results extrapolated from different sized supercells confirms the accuracy of this approach.

The defect calculations were performed with the supercell fixed at the theoretical equilibrium lattice parameter: 4.417 Å for LDA and 4.680 Å for PBE, the experimental lattice constant is 4.567 Å [13]. The measured bulk modulus for B2 structure CsI is 12.6 GPa [14]. Our computed LDA bulk modulus is 16.6 GPa, slightly stiffer than experiment, and the PBE value is 9.7 GPa, slightly softer than experiment, like the lattice constant, bracketing the experimental value as LDA and PBE usually do. Supercells ranged from $3 \times 3 \times 3$ (54-site) to $6 \times 6 \times 6$ (432-site) scaled versions of the primitive 2-atom cell of the CsI B2 structure, and used 3^3 grids for sampling the Brillouin zone in the 54-site cell and 2^3 k -grids for the larger cells. The atomic configurations were energy-relaxed to within 1 meV of a local minimum, with forces on atoms less than 0.01 eV Å⁻¹. Supercell size tests (with LDA) indicated that 54-site and 128-site failed to adequately contain the extensive strain fields around the defects, while 250-site results were well-converged compared to 432-site results. Results reported in this paper are extrapolated from 250-site supercell calculations. Formation energies are quoted in the Cs-rich limit, i.e., the bulk bcc Cs and CsI define the atomic reference chemical potentials. In this context, the computed formation energy of the neutral Cs vacancy is 3.74 (4.22) eV and of the I vacancy, 0.50 (0.54) eV using PBE (LDA). The heat of formation of B2 structure CsI, from bulk bcc Cs and the I₂ molecule elemental references are computed to be 3.71 eV in LDA and 3.42 eV in PBE. These heats of formation, using the conventions outlined by Zhang and Northrup [15] to compute defect formation energies, can be used to convert the defect formation energies from one limit (Cs-rich) to another (I-rich).

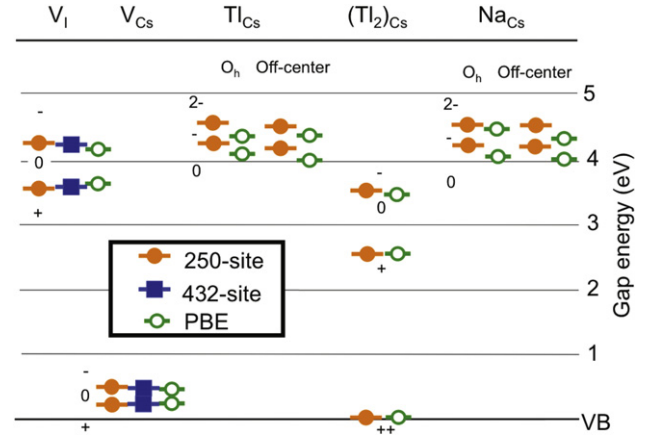


Figure 1. Defect levels in CsI. LDA and GGA (PBE) are both shown, results are the same within error of the techniques. Results are converged at 250 atoms.

3. Results

Calculations were performed for a purposefully selected set of defects, two intrinsic defects, the Cs vacancy V_{Cs} and the I vacancy V_I , and then for the dopant atoms Tl and Na, both known to substitute on the Cs site: Tl_{Cs} and Na_{Cs} . In Tl-doped CsI, the Tl dimer substitutional, $(Tl_2)_{Cs}$, is a common defect, and was also included in this series of calculations. Furthermore, this dimer proves especially important to set a useful limit on the position of the valence band edge. An extensive search was undertaken to find all the stable charge states and determine their optimum structure. The resulting defect level diagram, summarizing the positions of the ground state charge transitions within the CsI band gap, is presented in figure 1.

The doubly ionized Tl dimer center state is only barely in the band gap in the DFT calculations, both LDA and PBE, and, in the absence of a more definitive marker to locate the band edge on this diagram, its $(+/++)$ transition is adopted as the valence band edge (VBE). The VBE cannot be directly computed in the same total energy calculations used to obtain the defect level energies, but we can use this defect, cleanly identified as a local defect state, and therefore in the band gap, as the upper bound of the position of the VBE. As we shall see later, this choice is likely overly conservative.

The V_{Cs} has charge transitions only slightly above the $(Tl_2)_{Cs}$ $(+/++)$ transition, near the VBE, and the V_I has levels high in the gap. The near-perfect agreement between the levels extrapolated from the 250-site cells and from the 432-site cells, depicted in figure 1 for the vacancies, confirms the convergence of these defect level calculations to the infinitely dilute bulk limit. The LDA and PBE calculations agree closely with each other, finding the same charge states and similar ground state structures for all the defects. The computed levels for all defects are, reassuringly, not sensitive to the choice of density functional, lending greater confidence to the analysis of the results [8].

The measured band gap is reported to be 6.1–6.4 eV [16–18]. Our computed defect levels span a range of almost

5 eV, exceeding the Kohn–Sham (eigenvalue) gap for CsI for LDA and PBE in these calculations, which is 3.80 and 3.58 eV, respectively.

The calculation of localized defect levels can be used to identify possible dopants, and defects that may compete with desired emitters for hole or electron trapping. For example, from figure 1 we can deduce that the iodine vacancy or the negatively charged $(\text{I}_2)_{\text{Cs}}$ may compete with the luminescent Tl or Na dopants, while the cesium vacancy certainly will not.

3.1. Intrinsic defects

The V_{I} is a commonly occurring defect that plays an important role in energy losses [19], and interferes with light output. We find that this defect can trap either a hole or an electron, with 0, 1 or 2 electrons in the vacancy for the $V_{\text{I}}(+)$, $V_{\text{I}}(0)$ and $V_{\text{I}}(-)$ charge states of the defect (see figure 1). The neutral V_{I} , commonly known as the F-center, takes a symmetric O_{h} structure in spin-polarized calculations, as do both the ionized $V_{\text{I}}(+)$ and the $V_{\text{I}}(-)$, the latter commonly known as the F' -center. Our calculations predict the ionization level for the F-center, the $(0/+)$ transition in figure 1, to be 3.5 eV above the Tl dimer $(+ / + +)$ transition, our assumed VBE. The ionization level of the F' -center, the $(- / 0)$ transition, is predicted to be 0.8 eV above the F-center ionization, in excellent agreement with the experimental separation of 0.8 eV [20]. This close agreement lends confidence to the calculations, but should be considered in light of large quoted uncertainties in the experimental analysis of ~ 0.5 eV.

Locating the experimental levels relative to a band edge is less definitive, as this defect level position in the gap is not measured directly. The position of the F-center level is deduced through a combination of different experimental analyses, that starts with the photoexcitation of the F-center electron into vacuum, then derives the distance of the conduction band edge (CBE) from the vacuum via measurements of the electron affinity of bulk CsI, and then also includes the size of the band gap. The F-center electron and F' -center electron have vacuum ionization energies quoted as 2.2 and 1.4 eV, respectively, with large uncertainty in the latter [20]. The vacuum to CBE distance is quoted to be 0.3 eV [20, 18] to as large as 0.7 eV [21]. The band gap also adds about 0.2 eV uncertainty. The experimental analyses suggest an ionization level for the F-center of roughly or a little less than 4 eV above the VBE [21, 20, 22]. Our calculation predicts this level is 3.5 eV, or greater, above the VBE, in rather good agreement with this experimental analysis, considering the uncertainties in the experimental analysis. Given that the band gap is explicitly contained within the experimental assessment of this level, this implies that the effective band gap seen by the semilocal DFT calculations is within ~ 0.5 eV of experiment.

The low defect formation energy of the V_{I} is consistent with the easy formation of F-centers [19, 23]. The formation energy of $V_{\text{I}}(+)$ is reduced linearly with the distance of the Fermi level below the F-center transition, where the $V_{\text{I}}(+)$ formation energy exactly matches the formation energy of $V_{\text{I}}(0)$. Taken together, the splitting of the V_{I} donor states,

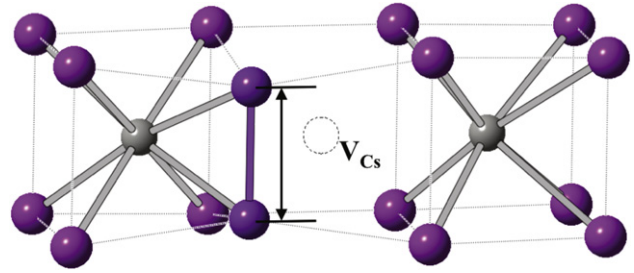


Figure 2. Local minimum with a V_k -like distortion adjacent to a Cs vacancy (V_{Cs}). Iodine is shown in dark gray (violet), Cs is light gray (silver). The iodine–iodine distance indicated by the arrow is decreased from the bulk crystal distance of 4.68–3.45 Å.

the implicit agreement with experimental band gap, and the correct physical description of the formation of iodine vacancies, these results indicate that the semilocal LDA and PBE functionals are performing accurately for the ground state defects in CsI.

The V_{Cs} may also trap either a hole or an electron. In LDA, the defect remains in a symmetric structure for each charge level. The relatively high formation energy, near 4 eV, is consistent with this not being a common defect in CsI. However, the V_{Cs} exhibits another interesting feature in the calculations. Using spin-polarized PBE we found a second minimum for the neutral doublet state in which a pair of iodine atoms adjacent to the vacancy dimerize, resembling a V_k center geometry [3]. This minima is a shallow metastable state 0.18 eV higher than the symmetric configuration. That a V_k -like center is found at all without the use of hybrid functionals implies that this defect is a significant trap with the ability to strongly localize holes at sites in the iodine sublattice adjacent to the vacancy. This $V_k + V_{\text{Cs}}$ configuration is shown in figure 2.

3.2. Dopants

Both the Tl and Na dopant centers, in addition to having a stable neutral state, can trap one or two electrons. In addition to these ground state structures, both the LDA and the PBE find a neutral triplet DTE to be stable for the Tl and Na dopants. These trap levels are high in the gap, roughly at or above the V_{I} defect levels. While each charge state has a metastable symmetric on-site configuration, they all have lower-energy off-site distortions, with minima in three distinct directions: toward the 001-face, toward the 110-edge and a shallower minimum directly toward the nearest-neighbor iodine in the 111-direction. These distortions had been predicted for Tl-trapped excited states in CsCl:Tl, CsBr:Tl, and CsI:Tl [24–26]. Our calculations confirm the presence of these distortions in the triplet DTE, but we find that these distortions already exist in the ground state, including for the neutral defect.

The magnitudes of these displacements are summarized in table 1. The distortion is small in the neutral defect (e.g. the Tl^+), reminiscent of a soft-mode ferroelectric phase transition seen in dilated III crystals [27]. This state has no localized

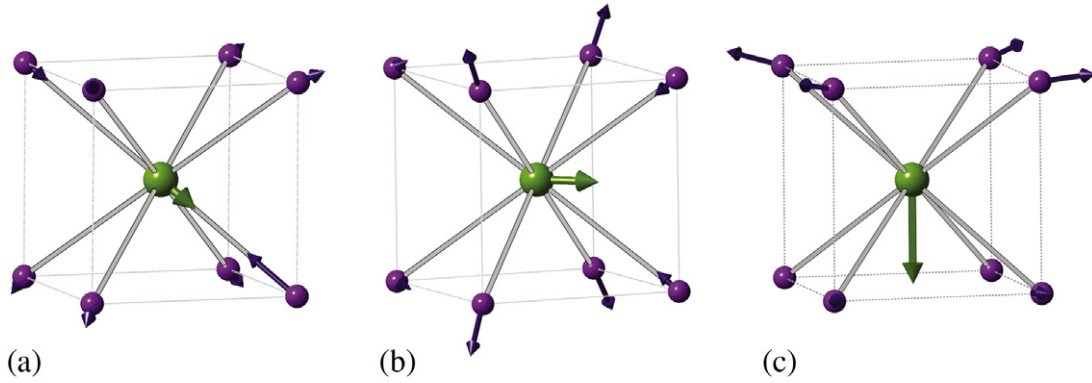


Figure 3. The three off-center structures for the Tl^0 center and nearest-neighbor shell of iodine. Tl is shown as light gray (green), I is dark gray (violet). For visual clarity, the arrows are exaggerated by a factor of 2 for the Tl displacement, and by a factor of 10 for the I displacement. The Tl^0 is displaced along (a) 100, (b) 110 or 111 directions. The displacements are with respect to the symmetric Tl^0 structure.

Table 1. Displacement parameters in lattice units for Tl in CsI(Tl) for LDA and PBE in the neutral (Tl^+) state, with 1 (Tl^0) and 2 (Tl^-) trapped electrons, and in the neutral triplet state.

Direction		Tl^+	Tl^0	Tl^-	Triplet
100	LDA	0.01	0.19	0.21	0.31
	PBE	0.11	0.23	0.23	0.36
110	LDA	0.01	0.11	0.13	0.10
	PBE	0.10	0.15	0.14	0.16
111	LDA	0.01	0.03	0.07	0.02
	PBE	0.09	0.08	0.07	0.08

Table 2. Calculated and measured triplet luminescence energy (E_{lum}) for the Tl center in CsI, eV (nm).

Geometry	LDA (this work)		Experiment [30]	
	E_{lum}	Peak assignment	Peak assignment	E_{lum}
100	2.90 (427)	A'_X		2.25 (560)
110	3.38 (367)	A'_T		2.55 (490)
111	3.49 (355)	A_T		3.09 (400)
O_h	3.55 (349)	A_X		3.31 (370)

electrons in the gap, yet already exhibits a distinct distortion. The distortion is larger in PBE, perhaps because of larger lattice constant and softer bulk modulus in PBE, relative to the LDA, are more accommodating to an off-site distortion. The distortion becomes larger in magnitude as localized electrons are trapped at the center. The displacement for the Tl^0 (single trapped electron) center is significant, about 1 Å, about halfway to the face of the cube formed by the nearest-neighbor iodine ions. The localization exhibited here demonstrates that the semilocal functionals, unlike for the STE and V_k center, are not afflicted with a localization problem for these ground state defects.

The structures of the off-center dopants are only found if the surrounding lattice is allowed to relax; distorting the dopant off-site from a symmetric structure causes the dopant to return to the central site. The displacement is accompanied by significant long-range distortions in the lattice, involving the coordinated movement of over 100 atoms. The nature of the distortions for the dopant and nearby atoms is depicted in figure 3. The displacement field around the distorted dopant has pairing distortion reminiscent of incipient V_k centers. This dimerizing distortion is strongest and most apparent in the neighbors of the 110-distorted dopant center shown in figure 3(b), but this tendency extends deep into the surrounding lattice.

In the neutral singlet ground state, the distorted configurations have energies within 0.02 eV of each other. For dopants with trapped electrons or in the triplet state results for

LDA show that the off-center minima are 0.02–0.06 eV lower than central position, all within 0.04 eV, in the order 111 > 110 > 100 (100 is lowest-energy position). For PBE, these energy differences are slightly enhanced. Despite requiring the concerted motion of over 100 atoms, barriers between these states are also low, ~ 0.01 eV, close to the resolution of the current methods, for hops directly between off-center positions. The low barriers between the local minima are consistent with previous predictions from both theory and experimental work [24, 28] for energy transfer between the different excited state emissions assigned directly to the Tl. This result means that dopant atoms may vibrate nearly freely about the cage, except at very low temperatures, as was found for Tl in NaI:Tl [29]. It also implies that the position of the dopant is very strongly affected by local phonon modes or any local distortions.

3.2.1. Off-center Tl and calculated emission energies.

The current results yield four possible Tl-related emission energies, based on the four possible positions of the Tl center in the triplet state. These energies, which we calculated as the difference between the triplet and singlet potential energy surfaces at the relaxed triplet (DTE) geometry, are listed in table 2, along with measured emission energies and suggested assignment based on polarization data [30]. The current results suggest emission from an interconnected potential energy surface of the several configurations of the Tl center. The calculated energies correspond roughly to the observed peaks, but this picture is not complete.

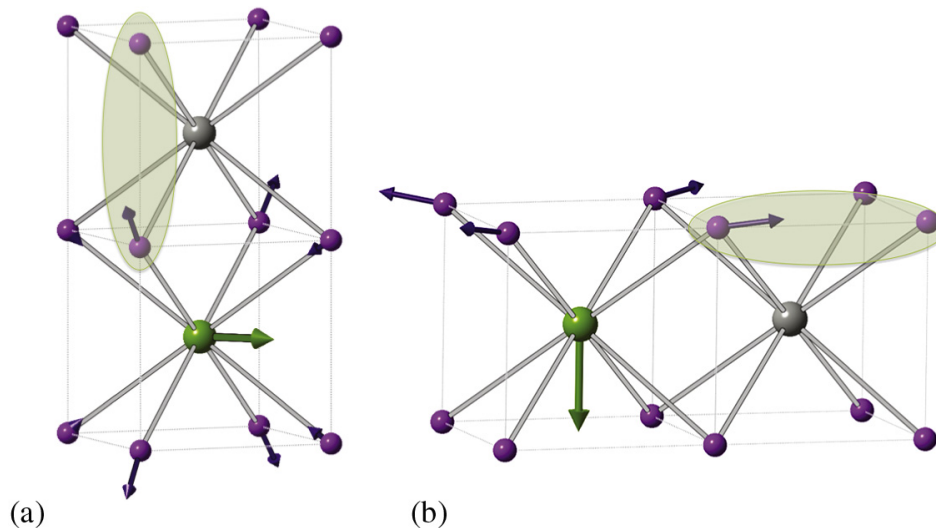


Figure 4. Possible V_k center placements adjacent to 110 (a) and 100 (b) off-center Tl centers. Tl is shown as light gray (green), I is dark gray (violet), Cs is silver.

Interpretation of experimental measurements has led to the assignment of the UV peaks to relaxed excited states of the Tl center, and the visible emission peaks to tunneling recombination between the Tl atom and a nearby V_k center [31, 32]. The two visible peaks, (A'_X and A'_T) are also postulated to be due to the interaction of a Tl and a perturbed STE either adjacent to the Tl, or offset by one unit cell [33].

Through examination of the distortions in the iodine sublattice in our results, we are able to identify several likely locations for a perturbed V_k center. We note that especially for the 110 distorted Tl, we see nearby distortions of the I lattice that resemble incipient V_k centers even in the ground state. Proposed adjacent perturbed V_k centers for the 110 and 100 Tl displacements are shown in figure 4. There was no obvious candidate for the 111 distortion. Localization of an STE or V_k on one of these iodine pairs should lower the energy of the 100 and 110 states, resulting in lower calculated emission energy, more in line with the experimental values. Quantitative investigation of the localized V_k center and STE, beyond the scope of this work, will require simulation methods with more explicit treatment of exchange, such as hybrid functionals [29, 3].

Finally, we note that the distortion field of the iodine sublattice resembles an array of incipient V_k centers, and therefore may be expected to interact with the transport of energy carriers near Tl or Na dopants. This indicates that transport and emission characteristics related to the off-center distortion of the dopant center will be strongly tied to phonon modes of the crystal.

Acknowledgments

This project is supported by Office of Nuclear Nonproliferation Research and Engineering (NA22), the US Department of Energy. The research was performed in part using EMSL, a national scientific user facility sponsored by the Department of Energy's Office of Biological and Environmental Research

and located at Pacific Northwest National Laboratory. Sandia National Laboratories is a multi-program laboratory managed and operated by Sandia Corporation, a wholly owned subsidiary of Lockheed Martin Corporation, for the US Department of Energy's National Nuclear Security Administration under Contract DE-AC04-94AL85000.

References

- [1] Nikl M 2000 Wide band gap scintillation materials: progress in the technology and material understanding *Phys. Status Solidi* **178** 595
- [2] Aguado A, Ayuela A, Lopez J M and Alonso J A 1998 Lattice distortions around a Tl^+ impurity in NaI: Tl^+ and CsI: Tl^+ scintillators: an *ab initio* study involving large clusters *Phys. Rev. B* **58** 11964
- [3] Van Ginhoven R M, Jaffe J E, Kerisit S and Rosso K M 2010 Trapping of polarons and excitons in scintillators: CsI, LaCl₃, and LaBr₃ *IEEE Trans. Nucl. Sci.* **57** 2303–8
- [4] Derenzo S E and Weber M J 1997 *Ab initio* cluster calculations of hole transport and activator excitation in CsI:Tl and CsI:Na *IEEE CNF, Nuclear Science Symp.* vol 1, p 164
- [5] Schultz P A 1982 SeqQuest code unpublished (See <http://dft.sandia.gov/Quest>)
- [6] Perdew J P and Zunger A 1981 Self-interaction correction for density-functional approximations for many-electron systems *Phys. Rev. B* **23** 5048
- [7] Perdew J P, Burke K and Ernzerhof M 1996 Generalized gradient approximation made simple *Phys. Rev. Lett.* **77** 3865
- [8] Mattsson A E, Schultz P A, Mattsson T R, Leung K and Desjarlais M P 2005 Designing meaningful density functional theory calculations in material science—a primer *Modelling Simul. Mater. Sci. Eng.* **13** R1
- [9] Hamann D R 1989 Generalized norm-conserving pseudopotentials *Phys. Rev. B* **40** 2980
- [10] Louie S G, Froyen S and Cohen M L 1982 Nonlinear ionic pseudopotentials in spin-density-functional calculations *Phys. Rev. B* **26** 1738
- [11] Schultz P A 2000 Charged local defects in extended systems *Phys. Rev. Lett.* **84** 1942
- [12] Schultz P A 2006 Theory of defect levels and the 'band gap problem' in silicon *Phys. Rev. Lett.* **96** 246401

- [13] Bührer W and Hälgl W 1971 Crystal dynamics of cesium iodide *Phys. Status Solidi b* **46** 679
- [14] Chang Z P and Barsch G R 1967 Nonlinear pressure dependence of elastic constants and fourth-order elastic constants of cesium halides *Phys. Rev. Lett.* **19** 1381
- [15] Zhang S B and Northrup J E 1991 Chemical potential dependence of defect formation energies in GaAs: application to Ga self-diffusion *Phys. Rev. Lett.* **67** 2339
- [16] Eby J E, Teegarden K J and Dutton D B 1959 Ultraviolet absorption of alkali halides *Phys. Rev.* **116** 1099–105
- [17] Teegarden K and Baldini G 1967 Optical absorption spectra of the alkali halides at 10 K *Phys. Rev.* **155** 896–907
- [18] DiStefano T H and Spicer W E 1973 Photoemission from CsI: experiment *Phys. Rev. B* **7** 1554
- [19] Popov A I and Balanzat E 2000 F centre production in CsI and CsI-Tl crystals under Kr ion irradiation at 15 K *Nucl. Instrum. Methods B* **166/167** 545–9
- [20] Sarkas H W, Kidder L H and Bowen K H 1995 Photoelectron spectroscopy of color centers in negatively charged cesium iodide nanocrystals *J. Chem. Phys.* **102** 57–66
- [21] Chowdhury M A H, Watts S J, Imrie D C, McKemey A K and Holmes-Siedle A G 1999 Studies of radiation tolerance and optical absorption bands of CsI(Tl) crystals *Nucl. Instrum. Methods A* **432** 147–56
- [22] Galiy P V, Mel'nyk O Ya and Tsvetkova O V 2005 Excitonic ionizations of the electron centres in caesium iodide crystal and exoemission of electrons *J. Lumin.* **112** 105–8
- [23] Song K S and Williams R T 1996 *Self-Trapped Excitons (Springer Series in Solid-State Sciences vol 105)* (New York: Springer)
- [24] Pazzi G P, Nikl M, Bacci M, Mihokova E, Hlinka J, Fabeni P and Salvini L 1994 Influence of Ti^{+} concentration on emission and decay kinetics of CsI:Ti⁺ single crystals *J. Lumin.* **60/61** 527–30
- [25] Zazubovich S G 1970 Jahn–Teller effect and partially covalent bond as causes of low symmetry of Ga^{+} , In^{+} , and Tl^{+} centers in CsCl-type alkali halides *Phys. Status Solidi B* **38** 119
- [26] Bacci M, Mihoková E and Polák K 1997 Coexistence of Jahn–Teller distortions in an O_h symmetry: a general view including the spin–orbit interaction *Phys. Rev. B* **55** 14257
- [27] Du M-H and Singh D J 2010 Enhanced Born charge and proximity to ferroelectricity in thallium halides *Phys. Rev. B* **81** 144114
- [28] Nikl M, Hlinka J, Mihokova E, Polak K, Fabeni P and Pazzi G P 1993 Decay kinetics of CsI:Tl luminescence excited in the A absorption band *Phil. Mag. B* **67** 627–49
- [29] Prange M P, Van Ginhoven R M, Govind N and Gao F 2013 Formation, stability and mobility of self-trapped excitations in NaI and NaI(Tl) *Phys. Rev. B* **87** 115101
- [30] Nagirnyi V, Stolovich A, Zazubovich S, Zepelin V, Mihokova E, Nikl M, Pazzi G P and Salvini L 1995 Peculiarities of the triplet relaxed excited-state structure and luminescence of a CsI:Tl crystal *J. Phys.: Condens. Matter* **7** 3637–53
- [31] Fu C-R, Chen L-Fu and Song K S 1999 Self-trapped excitons in pure and Na- and Tl-doped caesium halides and the recombination luminescence *J. Phys.: Condens. Matter* **11** 5517–32
- [32] Mihokova E, Nagirnyi V, Nikl M, Stolovich A, Pazzi G P, Zazubovich S and Zepelin V 1996 Relaxed excited state structure and luminescence of thallium-doped caesium chloride and bromide *J. Phys.: Condens. Matter* **8** 4301–14
- [33] Nagirnyi V, Zazubovich S, Zepelin V, Nikl M and Pazzi G P 1994 A new model for the visible emission of the CsI:Tl crystal *Chem. Phys. Lett.* **227** 533–8

Suppression of nonradiative recombination in ionic insulators by defects: Role of fast electron trapping in Tl-doped CsI

Junhyeok Bang,¹ Z. Wang,² F. Gao,² S. Meng,³ and S. B. Zhang¹

¹*Department of Physics, Applied Physics, and Astronomy, Rensselaer Polytechnic Institute, Troy, New York 12180, USA*

²*Pacific Northwest National Laboratory, MS K8-93, P.O. Box 999, Richland, Washington 99352, USA*

³*Beijing National Laboratory for Condensed-Matter Physics and Institute of Physics, Chinese Academy of Sciences, Beijing 100190, China*

(Received 4 September 2012; revised manuscript received 9 April 2013; published 23 May 2013)

In semiconductors, defects often assist nonradiative relaxation. However, Tl doping can significantly suppress the nonradiative relaxation in alkali halides to increase scintillation efficiency. Without the Tl, it is known that the creation of Frenkel pairs at self-trapped excitons, assisted by excited electron and hole relaxations, is the reason for the nonradiative relaxation. Here we show by first-principles calculation that Tl doping introduces Tl p states inside the band gap to trap the excited electrons. The trapping is highly effective to within several picoseconds, as revealed by time-dependent density functional theory calculations. It alters the nonradiative relaxation process to result in a noticeable increase in the relaxation barrier from 0.3 to 0.63 eV, which reduces the nonradiative relaxation by roughly a factor of 10^5 at room temperature.

DOI: [10.1103/PhysRevB.87.205206](https://doi.org/10.1103/PhysRevB.87.205206)

PACS number(s): 71.55.-i, 71.38.Ht, 72.20.Jv, 78.55.Fv

I. INTRODUCTION

Nonradiative recombination (NRR) of excited carriers is one of the most fundamental phenomena in semiconductors and insulators. NRR can quench luminescence and limit photovoltaic device efficiency. Therefore, understanding NRR also has practical importance.¹⁻³ However, NRR is often complex involving excited carriers. This leads to difficulties in theoretical analysis and identification of its microscopic origin. As such, key knowledge on NRR is often lacking.

In semiconductors, defects are viewed as the cause for NRR.^{4,5} However, in alkali halides counterexamples exist. For example, in scintillation material CsI, which is widely used as a high-energy particle detector,^{6,7} a minute amount of Tl doping can significantly suppress NRR and increase light emission efficiency.^{8,9} This hints that certain types of defects may improve the efficiency of an optoelectric device. Although there have been considerable efforts to understand the role of Tl,¹⁰⁻¹⁶ the underlying mechanism for the NRR suppression is still unclear. Physical processes in which a dopant reduces rather than increases the NRR is critically important to material research, as it offers clues not only for improved scintillation but also for better LED, laser, photovoltaic, and spintronic devices.

In this work, we present a state-of-the-art treatment of the problem, which includes both hybrid functional calculations for the self-trapped hole (STH) and the self-trapped exciton (STE) and, separately, time-dependent density functional theory (TDDFT) calculations for explicit electron relaxation dynamics. Our study reveals two effects of the Tl: First, there exists a large binding between substitutional Tl and STE of 0.88 eV, therefore an STE is bound to Tl until it undergoes a radiative relaxation or NRR. Second, Tl increases the NRR barrier of the trapped STE significantly to prevent the NRR from happening. It is believed that NRR is caused by the creation and migration of Frenkel pairs. Without the Tl, excited electrons at the conduction band minimum (CBM) and holes at the valence band maximum (VBM) assist the creation of the Frenkel pairs through a strong electron-phonon coupling. With the Tl, however, the excited electron is transferred

to the Tl p states within several picoseconds. As a result, the carrier-assisted Frenkel-pair formation paths are blocked, leading to significantly enhanced scintillation efficiency.

II. METHODS

Our structural optimization is based on the spin-polarized density functional theory (DFT) with the hybrid PBE0 functional,¹⁷ as implemented in the VASP code.¹⁸ Projected augmented wave potentials¹⁹ are used for ionic pseudopotentials. Wave functions are expanded in a plane-wave basis with an energy cutoff of 290 eV. We use a $5 \times 3 \times 3$ supercell that contains 90 atoms with the [100] direction as the long axis to facilitate the study of interstitial diffusion. Γ point is used for the Brillouin zone integration. Tests with different cell size and k -point sampling suggest that the total energy is converged to within 0.01 eV. The ionic coordinates are fully relaxed until the residual forces are <0.03 eV/Å. To mimic electronic excitation, for pure CsI, we perform constrained DFT calculations in which we remove one electron from the VBM and place it at the CBM. For Tl-doped CsI, we place the excited electron at the Tl level. This is a valid approach because our calculation shows that the electron at the CBM instantaneously transfers to the Tl level. To calculate the energy barrier with nudged elastic band along with hybrid functional is currently difficult. Instead, we generated nine atomic configurations between the initial and final states and then relaxed all the atoms in each configuration except for the two diffusing iodine atoms.

A key to the determination of enhanced scintillation is the time required for electron trapping. The recent development of *ab initio* molecular dynamics (MD) coupled with TDDFT²⁰ makes this possible. Here, we use the TDDFT formalism implemented in the SIESTA code,^{21,22} with norm-conserving Troullier-Martins pseudopotentials,²³ the Perdew-Burke-Ernzerhof (PBE) exchange-correlation functional,²⁴ and a double- ζ polarized local basis set. The real-space grid is equivalent to a plane-wave cutoff energy of 200 Ry. The time step is 24 attoseconds. We use the Ehrenfest approximation

for ion motion. The supercell for defect contains 54 atoms. To prepare for TDDFT input, we perform electron-ground-state MD simulation at room temperature (RT = 300 K) and then constrained DFT with one electron in the CBM.

III. RESULTS: NONRADIATIVE RECOMBINATION PATHS IN UNDOPED CsI

Scintillation is a fundamental physical phenomenon for energetic particle interaction with solids. When a high-energy particle enters a scintillator material, the energy of the particle is transferred to the surroundings by generating electron and hole pairs. In most alkali halide scintillators, the hole can be localized by lattice distortion, leading to the formation of STH. In CsI, the distortion is the bonding between two adjacent iodine atoms [see Fig. 1(a)], to lower the system energy by 0.31 eV relative to undistorted CsI with delocalized hole. The charge contour plot in Fig. 1(a) reveals that the STH state inside the band gap [see Fig. 2(a)] is an antibonding state. An excited electron in the conduction band can bind to the STH to form an STE. The trapped electron is, on the other hand, delocalized over the supercell. Accordingly, the energy lowering of 0.32 eV due to the STE formation is only 0.01 eV larger than that of the STH [see Table I and Fig. 3(a)]. Not only does the STE itself emit light by radiative recombination, but the diffusion of the STH and STE can also lead to the transfer of their energy to other luminescence centers.^{25–29}

The STE can also undergo NRR through Frenkel-pair defect formation and diffusion.^{30–32} Figures 1(b)–1(d) show the evolution of the atomic structure during the NRR. First, two adjacent I atoms move along the [100] direction in such a way that the two share one anion lattice site, forming a dumbbell (DB) structure (I_i^{DB}). This leaves behind an I vacancy (V_i). We denote this vacancy-interstitial pair as $(V_i-I_i^{DB})^{first}$. As the I_i diffuses further away along the [100] direction, it can form additional metastable Frenkel pairs such as the one in Fig. 1(c): $(V_i-I_i^{TR})^{first}$ with one triple-I-atom chain (TR), as well as the

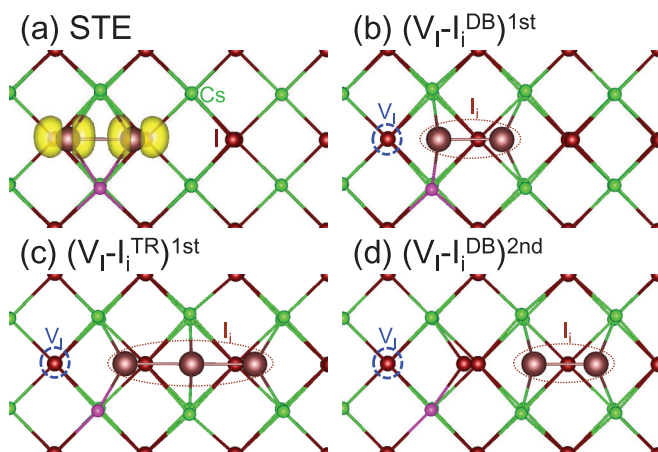


FIG. 1. (Color online) Atomic structures during the I_i diffusion: (a) STE, (b) $(V_i-I_i^{DB})^{first}$, (c) $(V_i-I_i^{TR})^{first}$, and (d) $(V_i-I_i^{DB})^{second}$, where first and second denote the I_i position relative to the V_i . Blue dashed circles denote the V_i 's; brown dotted ellipses denote the I_i 's. For TI-doped CsI, the TI atom replaces the pink Cs atom. In (a), the real-space charge of the STH state [see Fig. 2(a)] is shown by the yellow contours. DB and TR are defined in the text.

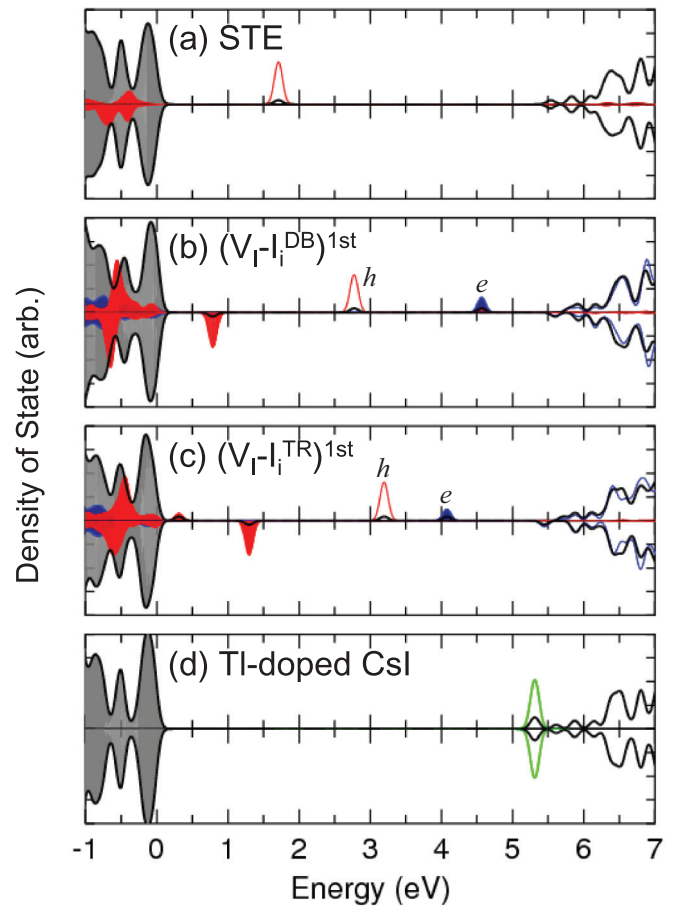


FIG. 2. (Color online) Density of states (DOS) of (a) STE, (b) $(V_i-I_i^{DB})^{first}$, (c) $(V_i-I_i^{TR})^{first}$, and (d) TI-doped CsI. The occupied states are shaded. Red, blue, and green lines denote the projected DOS onto the p states of the I interstitial, the s states of the Cs nearest neighbors to V_i , and the p states of the TI. All the projected DOS are scaled by a factor of 20 with respect to the total DOS.

one in Fig. 1(d): $(V_i-I_i^{DB})^{second}$ with an I DB structure. As the process goes on, the I_i eventually encounters a V_i and recombines, leaving their energy to the lattice as heat.

Figure 3(a) shows the energy landscape along the NRR path in Fig. 1: From STE to $(V_i-I_i^{DB})^{first}$, the energy is increased to 0.19 eV; from $(V_i-I_i^{DB})^{first}$ to $(V_i-I_i^{TR})^{first}$, the energy is further increased to 0.29 eV. After that, the total energy is nearly flat. The total diffusion barrier for this NRR path [from 1(a) to 1(d) in Fig. 3(a)] is $E_b = 0.30$ eV. The fact that E_b is slightly smaller than the delocalization barrier, 0.37 eV, of the STE [from 1(a) to No STE in Fig. 3(a)] suggests that it prefers NRR over delocalization. By using the rate equation $r = f \exp(-E_b/kT)$ and the optical vibration frequency $f = 2 \times 10^{12} \text{ s}^{-1}$ for CsI,³³ we estimate the NRR relaxation time at RT to be 50 ns. This value is on the same order of magnitude with the radiation decay time in CsI.^{8,34}

IV. RESULTS: THE EFFECTS OF TI DOPING

Because of the large binding of 0.88 eV between TI and STE, TI doping can significantly affect the formation of STE. A previous study²⁶ suggested that STE is mobile at RT with a

TABLE I. Energy change at different atomic configurations along the NRR path. Results for CsI with one hole are calculated at the same atomic structures of CsI with one $e-h$ pair to show the effects of the excited electron. The energy is given in unit of eV.

	No self-trapping	Self-trapping	$(V_1-I_i)^{DB}_{\text{first}}$	$(V_1-I_i)^{TR}_{\text{first}}$	$(V_1-I_i)^{DB}_{\text{second}}$
One $e-h$ pair	0.32	STE: 0.0	0.19	0.29	0.29
One hole	0.31	STH: 0.0	0.68	1.15	1.27

barrier as little as 0.15 eV. Thus, STE can be easily trapped at TI sites, in agreement with experiment.^{13,16} Figure 3(b) further shows that TI doping reduces the STE formation barrier [from No STE to 1(a) in Fig. 3(b)] to <0.01 eV. Hence, most STE exist as TI-STE pairs.

TI doping slows down the NRR by increasing the formation energy of Frenkel pairs. We can understand this by examining the evolution of the density of states in Fig. 2 in accordance with that of atomic structures in Fig. 1. Here, we focus on the hole (h) and electron (e) levels marked in Fig. 2, which belong to I_i and V_i , respectively. Going from Fig. 2(a) to Fig. 2(c), the hole level increases; the electron level decreases to enter the band gap. The reason for the change can be attributed to wave-function overlap between e and h , giving rise to level repulsion. As the I_i diffuses away from the V_i , however, the repulsion vanishes. Note that the higher the hole level, the more stable the hole. Thus, throughout the diffusion process in Fig. 1 both the excited electron and hole lower their energies, driving the diffusion forward.

If we remove the excited electron from the system, however, the energy of the Frenkel pairs increases significantly (see Table I). This is precisely what TI does to slow down and deter NRR. Figure 2(d) shows that the unoccupied p levels of the TI are below CBM, so the electron in the CBM can be transferred to TI. Whether such a process is important or not, however, depends on the time required for the transfer. If the time is longer than 50 ns, which is the NRR relaxation time in CsI, then excited carriers will decay nonradiatively. To estimate the electron transfer rate, we performed TDDFT calculations within the PBE functional. Strictly speaking, one may not use PBE here because semilocal functional may not describe charge transfer correctly. Currently, it is still not possible to carry out TDDFT-MD beyond the PBE, such as using a

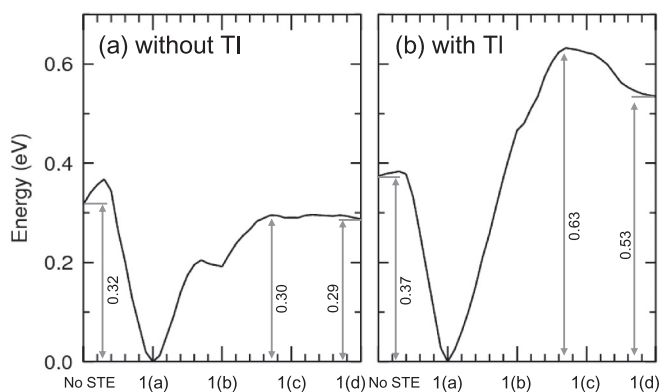


FIG. 3. Total energy landscape along the NRR path for (a) undoped CsI and (b) TI-doped CsI. The labels in the horizontal axes indicate atomic structures for STE diffusion given in Fig. 1.

nonlocal hybrid functional. This issue should be considered in future studies.

Figure 4(a) shows the time evolution of the energy levels for the excited electron in the CBM and the three empty TI p states.³⁵ The electron level decreases rapidly towards the TI p levels, which indicates that electron transfer from the CBM to the TI p levels has taken place. Accompanied with this electron transfer, ion kinetic energy increases [see Fig. 4(b)]. This is a strong indication that the transfer is mediated by electron-phonon coupling. As a measure of the transfer, Fig. 4(c) shows the change of the amount of electrons in the TI p levels, defined as $\Delta\rho_{\text{TI}}(t) = \sum_{i=1}^3 [\rho_{\text{TI},i}^{(e)}(t) - \rho_{\text{TI},i}^{(g)}]$ where $\rho_{\text{TI},i}^{(e)}$ and $\rho_{\text{TI},i}^{(g)}$ are the amount of electrons in the TI p_i states, $|\text{TI}, p_i\rangle$, for the excited and ground states, respectively. $\Delta\rho_{\text{TI}}(t=0)$ should be zero if the supercell size is sufficiently large; due to the relatively small cell size and the fact that $|\text{CBM}\rangle$ and $|\text{TI}, p_i\rangle$ are coupled states, however, $\Delta\rho_{\text{TI}}(t=0) = 0.3$ electrons in our simulation. Despite this, the qualitative result, e.g., $\Delta\rho_{\text{TI}}(t)$ increases with time, is not affected. In only 150 fs, $\Delta\rho_{\text{TI}}$ is increased to 0.43 electrons.

Upon excitation, the excited electron stays in the CBM for ~ 20 fs before significant transfer is noticed in Fig 4(c). This initial waiting is also observed in other materials such as TiO_2 .³⁶ Beyond the initial waiting time t_i , the time evolution of the electron transfer can be modeled by³⁶ $\Delta\rho_{\text{TI}}(t) = A(1 - \exp[-(t/\tau)])$, where τ is the decay time. As mentioned earlier,

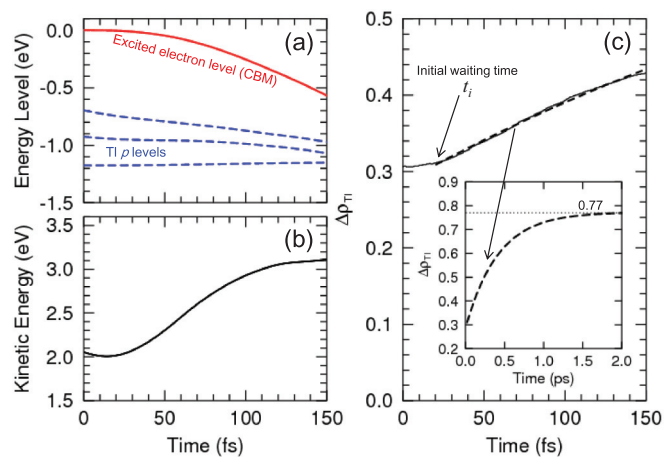


FIG. 4. (Color online) Time evolutions of (a) energy levels, (b) ion kinetic energy, and (c) electron transfer to TI p levels, $\Delta\rho_{\text{TI}}$. In (a), red and blue lines are the excited electron level and the empty TI p levels, respectively. In (c), the solid line is the TDDFT result, whereas the dashed line is a fitted result using Eq. (1). t_i is the initial waiting time. The dashed line in the inset in (b) is the same fitting but plotted at a longer time scale. It converges to 0.77 electrons within 2 ps.

$\Delta\rho_{\text{TI}}(t=0)$ is not zero due to finite cell size; here we modify the above equation to

$$\Delta\rho_{\text{TI}}(t) = A \left(1 - \exp\left[-\frac{t}{\tau}\right] \right) + 0.3. \quad (1)$$

Figure 4(c) shows that Eq. (1) with $A = 0.47$, $t_i = 20$ fs, and $\tau = 413$ fs fits the TDDFT results reasonably well. The inset in Fig. 4(c) shows that within 2 ps, about 0.77 electrons are transferred to TI. We can qualitatively understand the amount of electron transfer as follows: In the Ehrenfest dynamics, the excited electron state evolves into a superposed state between $|\text{CBM}\rangle$ and $|\text{TI}, p_i\rangle$,

$$|\varphi\rangle = a|\text{CBM}\rangle + b_1|\text{TI}, p_1\rangle + b_2|\text{TI}, p_2\rangle + b_3|\text{TI}, p_3\rangle \quad (2)$$

with approximately the same energy. If we assume $|a|^2 = |b_1|^2 = |b_2|^2 = |b_3|^2 = 1/4$, we get $\Delta\rho_{\text{TI}} = 3/4 = 0.75$ electrons. Note that this discussion considers only a single TI. If we take into account the coupling of the delocalized $|\text{CB}\rangle$ with multiple (n) TI atoms nearby, the amount of the electron transfer in the first 2 ps will increase to $\Delta\rho_{\text{TI}} = 1 - 1/(3n + 1)$, which approaches 1 in the limit $n \rightarrow \infty$. This suggests that the excited electron transfer from CBM to TI is considerably faster than the NRR in CsI by at least several orders of magnitude.

To calculate the NRR barrier for TI-doped CsI, we use PBE0 but with an excited electron in the TI p state as shown in Fig. 3(b). The energy difference between STE and $(V_i^{\text{DB}})^{\text{second}}$ increases to ~ 0.54 eV, which is 0.25 eV higher than that for undoped CsI. One can estimate the reduction in the NRR rate by $R = \exp(\Delta E_b/kT)$. Using $\Delta E_b = 0.63 - 0.30 = 0.33$ eV and $kT = 0.026$ eV, we obtain $R = 3 \times 10^5$ at RT. The corresponding NRR time is roughly 1 ms, which is enough to significantly increase light output.

V. IMPLICATION TO SEMICONDUCTORS

Note that the mechanism to deter NRR (discussed above) is not limited to only alkali halides or to ionic insulators. For

example, carrier trapping by BO_2 complexes in Si has been proposed as the main reason for NRR in B-doped Czochralski Si (Cz-Si) solar cell materials.³⁷ What is intriguing for this system is the lack of deep levels similar to CsI; electrons and holes that are temporarily trapped at near band-edge BO_2 states assist the NRR.³⁸ It is thus conceivable that one may reduce carrier trapping in Cz-Si by introducing impurities that are capable of taking the carriers away from BO_2 .

VI. SUMMARY

Hybrid functional study, coupled with TDDFT, reveals the effect of impurity doping on excited carrier relaxation in ionic insulators. Application to TI-doped CsI explains the experimentally observed significant increase of scintillation efficiency. The role of the impurity in suppressing NRR is unveiled in terms of the efficient transfer of excited electrons to impurity gap states. Our results suggest that defects/impurities not only can accelerate NRR as often observed,^{4,5,38} but can also be used to suppress certain NRRs, provided that the NRR does not involve deep levels as in the Shockley-Read-Hall regime.^{4,5} In other words, our understanding of the physics to deter NRR goes beyond just the improvement of current scintillator technology, but for educated defect engineering to suppress NRR in other optoelectronic materials.

ACKNOWLEDGMENTS

This work was supported by the National Nuclear Security Administration, Office of Nuclear Nonproliferation Research and Engineering (NA-22), of the US Department of Energy and by the Computational Center for Nanotechnology Innovations at RPI. F.G. and Z.G.W. acknowledge the use of the supercomputers in the Environmental Molecular Sciences Laboratory, a national scientific user facility sponsored by the US Department of Energy's Office of Biological and Environmental Research. S.M. is grateful for support from NSFC (Grants No. 11074287 and No. 11222431) and MOST (2012CB921403).

¹A. M. Stoneham, *Rep. Prog. Phys.* **44**, 1251 (1981).

²C. Deibel, T. Strobel, and V. Dyakonov, *Adv. Mater.* **22**, 4097 (2010).

³D. Hertel, S. Setayesh, H.-G. Nothofer, U. Scherf, K. Müllen, and H. Bässler, *Adv. Mater.* **13**, 65 (2001).

⁴W. Shockley and W. T. Read, *Phys. Rev.* **87**, 835 (1952).

⁵R. N. Hall, *Phys. Rev.* **87**, 387 (1952).

⁶M. Nikl, *Phys. Status Solidi A* **178**, 595 (2000).

⁷N. Yasui, Y. Ohashi, T. Kobayashi, and T. Den, *Adv. Mater.* **24**, 5464 (2012).

⁸P. Schotanus, R. Kamermans, and P. Dorenbos, *IEEE Trans. Nucl. Sci.* **37**, 177 (1990).

⁹M. M. Hamada, F. E. Costa, M. C. C. Pereira, and S. Kubota, *IEEE Trans. Nucl. Sci.* **48**, 1148 (2001).

¹⁰Z. Wang, Y. Xie, B. D. Cannon, L. W. Campbell, F. Gao, and S. Kerisit, *J. Appl. Phys.* **110**, 064903 (2011).

¹¹S. Kerisit, K. M. Rosso, and B. D. Cannon, *IEEE Trans. Nucl. Sci.* **55**, 1251 (2008).

¹²S. Kerisit, K. M. Rosso, B. D. Cannon, F. Gao, and Y. Xie, *J. Appl. Phys.* **105**, 114915 (2009).

¹³S. Zazubovich, *Radiat. Meas.* **33**, 699 (2001).

¹⁴J. M. Spaeth, W. Meise, and K. S. Song, *J. Phys.: Condens. Matter* **6**, 3999 (1994).

¹⁵V. Nagirnyi, A. Stolovich, S. Zazubovich, V. Zepelin, E. Mihokova, M. Nikl, G. P. Pazzi, and L. Salvini, *J. Phys.: Condens. Matter* **7**, 3637 (1995).

¹⁶V. Babin, P. Fabeni, K. Kalder, M. Nikl, G. P. Pazzi, and S. Zazubovich, *Radiat. Meas.* **29**, 333 (1998).

¹⁷J. P. Perdew, M. Emzerhof, and K. Burke, *J. Chem. Phys.* **105**, 9982 (1996).

¹⁸G. Kresse and J. Furthmüller, *Comput. Mater. Sci.* **6**, 15 (1996).

¹⁹P. E. Blochl, *Phys. Rev. B* **50**, 17953 (1994).

- ²⁰E. Runge and E. K. U. Gross, *Phys. Rev. Lett.* **52**, 997 (1984).
- ²¹J. M. Soler, E. Artacho, J. D. Gale, A. García, J. Junquera, P. Ordejón, and D. Sánchez-Portal, *J. Phys.: Condens. Matter* **14**, 2745 (2002).
- ²²S. Meng and E. Kaxiras, *J. Chem. Phys.* **129**, 054110 (2008).
- ²³N. Troullier and J. L. Martins, *Phys. Rev. B* **43**, 1993 (1991).
- ²⁴J. P. Perdew, K. Burke, and M. Ernzerhof, *Phys. Rev. Lett.* **77**, 3865 (1996).
- ²⁵R. M. V. Ginhoven, J. E. Jaffe, S. Kerisit, and K. M. Rosso, *IEEE Trans. Nucl. Sci.* **57**, 2303 (2010).
- ²⁶S. E. Derenzo and M. J. Weber, *Nucl. Instrum. Methods Phys. Res., Sect. A* **422**, 111 (1999).
- ²⁷G. Blasse, *Chem. Mater.* **6**, 1465 (1994).
- ²⁸M. Nikl, *Meas. Sci. Technol.* **17**, R37 (2006).
- ²⁹G. Bizarri, *J. Cryst. Growth* **312**, 1213 (2010).
- ³⁰A. I. Popov, E. A. Kotomin, and J. Maier, *Nucl. Instrum. Methods Phys. Res., Sect. B* **268**, 3084 (2010).
- ³¹N. Itoh, *Adv. Phys.* **31**, 491 (1982).
- ³²N. Itoh, A. M. Stoneham, and A. H. Harker, *J. Phys. C* **10**, 4197 (1977).
- ³³J. F. Vetelino, K. V. Namjoshi, and S. S. Mitra, *Phys. Rev. B* **7**, 4001 (1973).
- ³⁴C. Amsler, D. Grögler, W. Joffrain, D. Lindelöf, M. Marchesotti, P. Niederberger, H. Pruys, C. Regenfus, P. Riedler, and A. Rotondi, *Nucl. Instrum. Methods Phys. Res., Sect. A* **480**, 494 (2002).
- ³⁵TDDFT results in Fig. 4(a) reflect the splitting and lowering of the T1 p states due to symmetry breaking by the MD.
- ³⁶W. R. Duncan and O. V. Prezhdo, *Annu. Rev. Phys. Chem.* **58**, 143 (2007).
- ³⁷J. Schmidt and K. Bothe, *Phys. Rev. B* **69**, 024107 (2004).
- ³⁸M.-H. Du, H. M. Branz, R. S. Crandall, and S. B. Zhang, *Phys. Rev. Lett.* **97**, 256602 (2006).

Computer simulation of electron thermalization in CsI and CsI(Tl)

Zhiguo Wang,^{1,a)} YuLong Xie,² Bret D. Cannon,³ Luke W. Campbell,³ Fei Gao,¹ and Sebastien Kerisit^{1,a)}¹Fundamental and Computational Sciences Directorate, Pacific Northwest National Laboratory, Richland, Washington 99352, USA²Energy and Environment Directorate, Pacific Northwest National Laboratory, Richland, Washington 99352, USA³National Security Directorate, Pacific Northwest National Laboratory, Richland, Washington 99352, USA

(Received 26 May 2011; accepted 21 July 2011; published online 19 September 2011)

A Monte Carlo (MC) model was developed and implemented to simulate the thermalization of electrons in inorganic scintillator materials. The model incorporates electron scattering with both longitudinal optical and acoustic phonons. In this paper, the MC model was applied to simulate electron thermalization in CsI, both pure and doped with a range of thallium concentrations. The inclusion of internal electric fields was shown to increase the fraction of recombined electron-hole pairs and to broaden the thermalization distance and thermalization time distributions. The MC simulations indicate that electron thermalization, following γ -ray excitation, takes place within approximately 10 ps in CsI and that electrons can travel distances up to several hundreds of nanometers. Electron thermalization was studied for a range of incident γ -ray energies using electron-hole pair spatial distributions generated by the MC code NWEGRIM (NorthWest Electron and Gamma Ray Interaction in Matter). These simulations revealed that the partition of thermalized electrons between different species (e.g., recombined with self-trapped holes or trapped at thallium sites) vary with the incident energy. Implications for the phenomenon of nonlinearity in scintillator light yield are discussed. © 2011 American Institute of Physics. [doi:10.1063/1.3632969]

I. INTRODUCTION

Inorganic scintillators offer numerous advantages as radiation detection materials, and in particular for γ -ray spectroscopy, including high light yields, fast response, large active areas, and room-temperature operation.¹ Consequently, inorganic scintillators are widely used in nuclear and high-energy physics, nuclear medicine and medical imaging, geological exploration and many other fields. An ideal scintillator would produce a number of scintillation photons that is a linear function of the energy of the incident radiation. However, many inorganic scintillators display some degree of light yield nonlinearity (also often referred to as “nonproportionality”) following γ -ray excitation.² Nonlinearity is one of the main sources that degrade the intrinsic energy resolution of inorganic scintillators.^{3,4} Therefore, nonlinearity has received much attention from research groups that work to improve existing, and develop new, radiation detection materials. However, in spite of substantial efforts by several groups to elucidate the physical processes that give rise to nonlinearity, this phenomenon is not completely understood.

The chain of processes that begins with the interaction of an incident γ -quantum with a scintillator material and terminates with the emission of low-energy photons will be referred to as the scintillation process hereafter. The scintillation process can be divided into three stages. In the first stage, which will be referred to as the electron cascade, a track of electron-hole pairs is produced following the absorp-

tion of an incident γ -ray. In the second stage, the hot electrons and holes undergo thermalization to the edges of the band gap. In the third and last stage, light is emitted either via the recombination of electron-hole pairs at lattice sites or through energy transfer to luminescence centers, which then relax radiatively. It has been proposed that nonlinearity originates from the last stage of the scintillation process and is due to (1) nonradiative processes that depend nonlinearly on the ionization density and (2) the fact that the ionization density is energy dependent.^{2,5–11} An accurate description of the electron-hole pair density along the ionization track is therefore crucial to successfully evaluating how hypothesized processes may contribute to nonlinearity.

Several theoretical models have been developed to gain insight into the nonlinear response of inorganic scintillators. Early work focused on explaining the variations in scintillation efficiency as a function of stopping power, or specific energy loss, in an attempt to put the response of inorganic scintillators to different exciting particles on a common footing. For example, the model of Murray and Meyer⁸ described the behavior of the scintillation efficiency of NaI(Tl) as a result of increasing electron-hole pair recombination with increasing stopping power followed by saturation of activator sites at high stopping powers. Hill and Collinson^{12,13} later noted that the model of Murray and Meyer failed for low electron energies and found improved agreement with experimental scintillation efficiencies when including an additional process, namely, exciton emission followed by Tl absorption.

More recently, theoretical models of nonlinearity have focused on the response to γ -ray excitation. Payne *et al.*¹⁴ developed a model that describes the light yield of a range of

^{a)}Authors to whom correspondence should be addressed. Electronic addresses: sebastien.kerisit@pnl.gov and zhiguo.wang@pnl.gov.

inorganic scintillators as a product of the efficiencies of electron-hole pair recombination and exciton-exciton annihilation. Bizarri *et al.*^{15–17} developed a series of phenomenological models to calculate the light yield response curves of several model compounds on the basis of electron-hole pair densities obtained from the Bethe-Bloch equation or energy loss functions and radiative and nonradiative processes with linear, quadratic, or cubic dependence on the electron-hole pair density. However, it is difficult to experimentally measure the rate constants for these processes. Williams *et al.*^{10,11} investigated the role of carrier diffusion on carrier quenching and consequently on nonlinearity. They used a finite-element model that included diffusion, drift, Auger quenching, and dipole-dipole quenching processes and represented the electron-hole pair track as a cylinder with a Gaussian radial profile. Their modeling results indicate that the large difference between the band mobilities of electrons and holes in activated alkali halides can lead to an increase in the fraction of independent carriers at low stopping powers, which translates into a diminished relative light yield at high incident energies. All the models above have highlighted the importance of the electron-hole pair density along the ionization track and its variations with incident γ -ray energy. However, most models developed to date make use of idealized geometries and density profiles for representing ionization tracks. In this work, we employ electron-hole pair spatial distributions produced by the Monte Carlo (MC) code NWEGRIM (Northwest Electron and Gamma Ray Interaction in Matter), which determines the fate of individual electron-hole pairs down to energies on the order of the band gap and can compute the microscopic track structure.

Electron-hole pair spatial distributions generated by NWEGRIM were used in a previous publication⁵ to study the scintillation mechanisms in two major scintillators (CsI and LaBr₃) using a kinetic Monte Carlo model.^{5,18} The simulations showed that the annihilation between self-trapped excitons (STE) can account for the initial rise in relative light yield with increasing incident energy for both scintillators. However, the effect of the thermalization stage on the spatial distribution of electron-hole pairs was omitted in that study. The thermalization process is likely to make the spatial distributions more diffuse through electron-phonon interactions and could thus affect the light output. In this work, we develop a MC program to simulate the thermalization process and to determine how it affects the spatial distribution of electron-hole pairs.

We concentrate on pure and thallium-doped CsI for several reasons: CsI is one of the most widely used scintillators because of its high light yield ($\sim 65\,000$ ph/MeV); its nonlinear response has been well determined experimentally;^{19–22} and we used CsI as a model system in previous work.^{5,18}

II. COMPUTATIONAL METHODS

A. Thermalization process

A Monte Carlo algorithm was implemented in a computer program to calculate the trajectories of low-energy electrons due to interactions with longitudinal optical (LO) and acoustic (A) phonons and thus simulate the thermaliza-

tion of electrons generated following γ -ray excitation in alkali halides. As mentioned above, we initially focus our work on pure and thallium-doped CsI. The approach used to model electron-phonon interactions is described in Sec. II C. In addition, we hypothesize that, as the electrons thermalize via interaction with lattice phonons, they are also influenced by the electric field due to all the other electrons and holes generated during the energy cascade. Therefore, a treatment of the internal electric fields (IEF) was included to account for their effect on the electron trajectories. Simulations were performed with and without IEF to evaluate this hypothesis as described in Sec. III. The method employed to compute the internal electric fields is reported in Sec. II D. Moreover, the thermalization program requires a set of initial positions for the electrons and holes as well as a set of initial kinetic energies and directions of motion for the electrons. These were calculated with NWEGRIM as described in Sec. II B. The MC program is executed using the following algorithm.

- (1) The holes are assumed to self trap instantaneously and to be immobile and, therefore, were fixed at their initial positions throughout the simulations.
- (2) At each simulation step, one electron undergoes one of four electron-phonon interactions, namely, LO phonon emission, LO phonon absorption, A phonon emission, or A phonon absorption. An electron-phonon interaction is selected with a probability proportional to its scattering rate,

$$\sum_{j=1}^{i-1} \frac{\tau_j}{\Gamma} < x_1 \leq \sum_{j=1}^i \frac{\tau_j}{\Gamma} \quad (1)$$

where i is the electron-phonon interaction label, τ_j is the scattering rate of the j th process, x_1 is a random number in the range $0 < x_1 \leq 1$ determined using a random number generator, and Γ is the sum of all the scattering rates

$$\Gamma = \sum_{j=1}^{4N} \tau_j \quad (2)$$

where N is the total number of electrons. The scattering rates for phonon emission and absorption are calculated using the approach described in Sec. II C. In addition, all electrons undergo one electron-phonon interaction before the simulation begins to determine their position following the last electron-hole pair creation event calculated by NWEGRIM.

- (3) The kinetic energy, E_i , of the selected electron is modified by the characteristic LO or A phonon energy. Additionally, the step length, δ_i , and scattering angle, θ_i , of the selected electron are used to determine its new position. The step length is obtained from the scattering rates as follows:²³

$$\delta_i = -\frac{1}{\sqrt{m^*/2E_i} \sum_{j=1}^4 \tau_j} \ln x_2 \quad (3)$$

where x_2 is a random number in the range $0 < x_2 \leq 1$ and the scattering rate sum is over all four possible

electron-phonon interactions. The approach used to calculate τ and θ is described in Sec. II C. In addition, time is incremented using the following formula:

$$\Delta t = -\frac{\ln x_3}{\Gamma} \quad (4)$$

where x_3 is a random number in the range $0 < x_3 \leq 1$.

- (4) The new position and energy of the selected electron are used to evaluate whether it has recombined with a hole, has trapped at a thallium site, or has stopped. Two conditions are evaluated to determine if an electron has recombined with a hole: (a) if the electrostatic interaction energy between this electron and the nearest hole is higher than the electron kinetic energy, the electron is considered to have recombined with the nearest hole. The electrostatic interaction energy, E^S , is calculated as follows,

$$E^S = \frac{q_e q_h}{4\pi\epsilon\epsilon_0 r} \quad (5)$$

where q_e and q_h are the electric charges of the electron and hole, respectively, ϵ is the material's dielectric constant, ϵ_0 is the vacuum permittivity, and r is the electron-hole distance; and (b) if the distance between this electron and the nearest hole is less than 3.685 Å, the electron is also considered to have recombined with the nearest hole. The value of 3.685 Å is used to account for the fact that a self-trapped hole has a finite spatial extent. In CsI, a self-trapped hole is localized on two neighboring iodide ions, which thus form an I_2^- molecular ion. Plane-wave-pseudopotential density functional theory calculations of Van Ginhoven *et al.*²⁴ predicted the distance between two I ions of the I_2^- molecular ion to be 3.25 Å. Using an ionic radius of Γ of 2.06 Å, the molecular radius of I_2^- was taken to be $3.25/2 + 2.06 = 3.685$ Å. The probability for an electron within the self-trapped hole's molecular radius to be captured is likely to be dependent on the electron energy. However, as this probability is not known, we make the simplifying assumption that it is 1 for the purpose of this work.

For the simulations of Tl-doped CsI, the electron is trapped at a thallium site if

$$x_4 \leq P_{trap}(E) \quad (6)$$

where x_4 is a random number in the range $0 < x_4 \leq 1$ and the energy-dependent probability for electron capture is that introduced by Ganachaud *et al.*²⁵

$$P_{trap}(E) = \frac{\delta}{a} \times f(Tl) e^{-\gamma E} \quad (7)$$

where E is the electron energy, δ is the step length determined in Eq. (3), a is the lattice constant of CsI (0.457 nm), $f(Tl)$ is the fraction of unit cells occupied by a thallium atom. The constant γ limits the energy domain concerned by this process. There is no direct method to determine γ and, therefore, γ will be varied to determine its effects on electron thermalization. Finally, if the energy of the electron becomes less than the material's

electron affinity (0.1 eV for CsI), the thermalization process for this electron is considered to be stopped. The four possible states of an electron, i.e., free, recombined, stopped, and trapped, will be referred to as electron populations.

- (5) Every 10^{-16} s, the positions and kinetic energies of all the electrons are modified due to the effect of internal electric fields, as described in Sec. II D. A test is performed as in (4) for determining the fate of each electron.

B. Electron cascade: Electron-hole pair generation

The spatial distributions of electron-hole pairs generated by γ -ray excitation were computed with NWEGRIM. Details of the methodology used by NWEGRIM can be found in previous publications.^{26–28} Starting with an incident γ -ray photon, a primary electron-hole pair is generated through inner-shell photoionization or Compton scattering. Interband transitions, plasmon excitations, core shell ionizations, electron-phonon interactions, and Bremsstrahlung emissions are then considered as mechanisms that lead to the energy loss of a fast electron. After an ionization event, Auger/Coster-Kronig and shake-off electron cascades are followed until the vacancy reaches the outermost shell. The primary and secondary electrons are all followed until their energies are less than a cutoff energy of twice the band-gap energy. All the energies used in NWEGRIM are with respect to the valence band maximum. When an electron-hole pair is created, all the deposited energy is assigned to the emitted electron and the hole is assumed to have an energy of zero. Fig. 1 shows the kinetic energy distribution of the hot electrons at the end of the energy cascade. The electron kinetic energies distribute within one band gap (6.1 eV). There are two main peaks located at approximately 4.6 and 6.1 eV, which are due to plasmon decay and electron-phonon interactions, respectively. A single characteristic plasmon excitation energy is used in NWEGRIM, which therefore leads to the large spike in the energy distribution. Although electron-phonon interactions do not create electron-hole pairs, energy loss to phonons can bring the energy of some electrons below the energy cutoff, which leads to the peak at high kinetic energies.

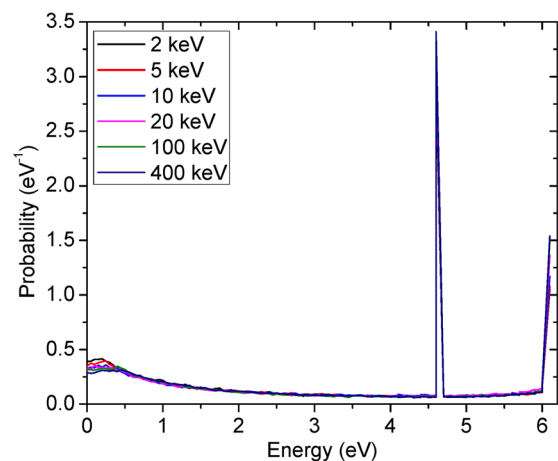


FIG. 1. (Color online) Kinetic energy distribution of the hot electrons at the end of the energy cascade.

We made one modification to NWEGRIM in the version used in this work with respect to that used in a previous publication,⁵ namely, if an energy loss mechanism selected by the MC algorithm leads to either the emitted electron energy or the scattered electron energy to fall below the band gap energy, the process is ignored and a new process is selected instead. Using the modified version of NWEGRIM, updated electron-hole pair yields (number of electron-hole pairs per MeV) and β parameters (mean energy per electron-hole pair normalized to the band-gap energy) were calculated, as shown in Table I. The yields of approximately 83 000 electron-hole pairs per MeV predicted by the new version of NWEGRIM are higher than those obtained previously⁵ (~ 65 000 electron-hole pair per MeV). As discussed in detail in a previous publication,⁵ published light yields for pure and TI-doped CsI range between 48 000 and 76 000 ph/MeV,^{29–36} with the exception of the absolute light yields reported by Moszyński *et al.*^{22,37} of 107 000 and 124 000 ph/MeV for nominally pure CsI samples. Because the electron-hole pair yields will decrease due to nonradiative processes, the fact that the calculated yields are higher than the experimental light yields is consistent with experimental measurements (not considering the two values of the light yield obtained by Moszyński *et al.* for pure CsI at liquid nitrogen temperature).

C. Thermalization of hot electrons: electron-phonon interactions

The scattering rates, scattering angles, and inverse mean free paths for emission and absorption of LO phonons are calculated using the formulation of Llacer and Garwin.³⁸ For the interaction between electrons and acoustical phonons, the description of Sparks *et al.*³⁹ was used together with the correction introduced by Bradford and Woolf.⁴⁰ This correction is used to correct the unphysical increase of the acoustic inverse mean free path (MFP) for energies higher than the first Brillouin zone energy (i.e., approximately 2 eV for CsI). A correction factor of $\{1/[1 + (q^2/\alpha^2)]\}^2$ is added into the integrand of the acoustic inverse MFP expression, where q is the phonon momentum and α is the screening correction parameter. A value of α of 24.3 nm^{-1} was used in this work. This value was determined by Boutboul *et al.*⁴¹ as the value required to make the corrected acoustic MFP converge to that of the elastic scattering at 20 eV. The formulae used for calculating inverse mean free paths, scattering rates, and

TABLE I. Number of electron-hole pairs per MeV generated using NWEGRIM code and the corresponding β parameters (mean energy per e-h pair normalized to the band gap (6.1 eV)).

Incident energy (keV)	Number of simulations	Number of e-h pairs per MeV	β
2	400	83 906	1.936
5	200	83 903	1.936
10	100	83 001	1.957
20	50	82 885	1.960
100	10	83 309	1.950
400	5	82 857	1.961

scattering angles are shown in supporting information.⁴² This formulation uses a series of parameters; their values and origins are shown in Table S1.⁴² Fig. 2 shows the scattering rates thus obtained for CsI.

D. Internal electric fields

The influence of internal electric fields on the electron trajectories was calculated using the classical equations of dynamics

$$\frac{d}{dt}[m^*v_i] = -eE_i^F \quad (8)$$

where m^* is the electron effective mass, v_i the velocity of electron i , and E_i^F , the electric field at the position of electron i , is defined as

$$E_i^F = \sum_{\substack{j=1 \\ j \neq i}}^{N_t} \frac{1}{4\pi\epsilon_0\epsilon} \frac{q_j}{r_{ij}^2} \hat{r}_{ij} \quad (9)$$

where N_t is the number of electrons and holes, q_j the charge of particle j , r_{ij} the distance between particles i and j , and \hat{r}_{ij} the unit vector. For the purpose of this work, we make the simplifying assumption that the electron effective mass is not dependent on its energy. Equation (8) needs to be discretized using a time step Δt . We evaluated the effect of Δt on the electron populations obtained for a 2-keV incident γ -ray considering solely the electron trajectories due to internal electric field and using time steps of value 10^{-15} , 10^{-16} , and 10^{-17} s, as shown in Fig. S1.⁴² The differences in electron populations between 10^{-16} and 10^{-17} s are small, indicating that $\Delta t = 10^{-16}$ s is short enough a time step to guarantee the convergence of the results and, therefore, we used $\Delta t = 10^{-16}$ s in the present simulations. We note that Eq. (9) breaks down for very short particle-particle interactions on the order of the size of the ions. Therefore, electron-electron electrostatic interactions between two electrons separated by a distance shorter than the Cs-I distance (3.9577 Å) were omitted.

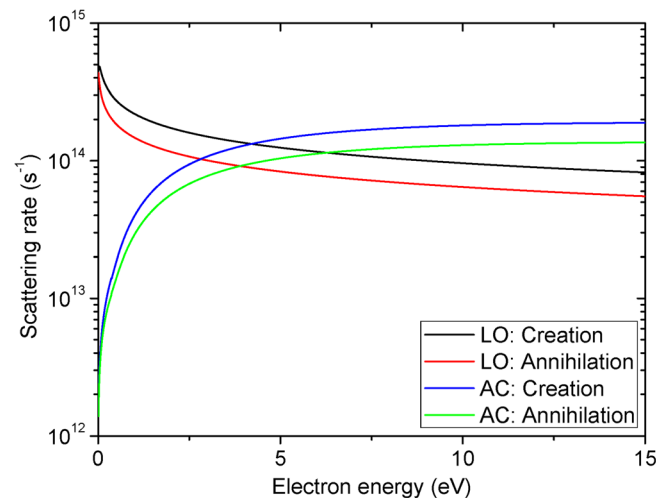


FIG. 2. (Color online) Scattering rate of electron-phonon interactions as a function of electron energy.

III. RESULTS AND DISCUSSION

A. Pure CsI

We first investigated the effects of internal electric fields on the thermalization of hot electrons by carrying out Monte Carlo simulations with and without IEF. Fig. 3 shows the calculated fractions of free, recombined, and stopped electrons as a function of time for a 2-keV incident γ -ray. This figure indicates that there are three main differences between the cases with and without IEF. First, the fraction of recombined electrons is larger when IEF are included. Indeed, when IEF are included, the attractive electrostatic interaction between electrons and holes increases the likelihood for recombination. Second, the fraction of stopped electrons increases more quickly initially with IEF, which suggests that, on average, the presence of IEF slows down the hot electrons. However, because the fraction of recombined electrons is greater with IEF, the fraction of stopped electrons is eventually higher without IEF. Third, there is a bump in the fraction of free and stopped electrons at ~ 6 ps for the case without IEF. As explained in more detail later, this is due to the electrons created as a result of plasmon excitation. Interestingly, the fraction of recombined electrons increases very quickly and reaches a maximum within 2.0 ps. Approximately, 23% of the electrons recombined during the first simulation step and this percentage increases, within 2.0 ps, to 41% and 34% with and without IEF, respectively. The time-scale for electron-hole pair recombination predicted in these simulations is consistent with the self-trapped exciton formation time obtained experimentally for other alkali halides.^{43,44} Qualitatively, the electron populations obtained for the other γ -ray incident energies considered in this work (5, 10, 20, 100, and 400 keV) show the same trends with time, as shown in Fig. S2.⁴² Quantitatively, Fig. 4 shows that the fraction of recombined electrons decreases with increasing incident energy, with and without IEF. The increased stopping power at low incident energies generates high electron-hole pair densities at these energies, which leads to an increased probability for electron-hole pair recombination.

Figs. 5(a) and 5(b) show the thermalization distance and time distributions, respectively, for a 2-keV incident γ -ray.

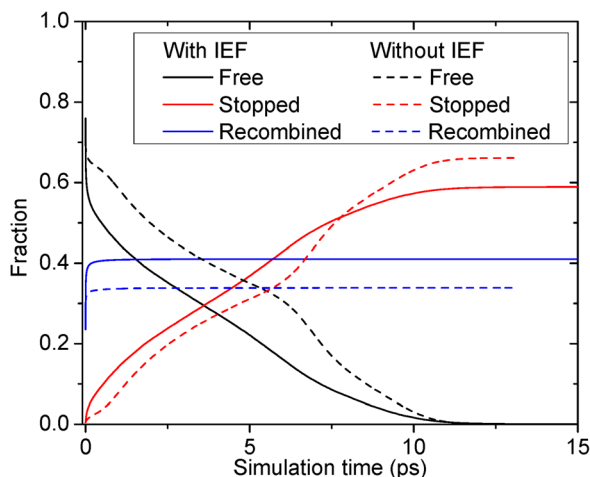


FIG. 3. (Color online) Fractions of free, recombined, and stopped electrons as a function of time for a 2-keV incident γ -ray.

Each distribution is decomposed based upon the processes by which the secondary electrons were created. As noted before, electron-phonon interactions cannot create electron-hole pairs but energy loss to phonons can bring the energy of some electrons below the energy cutoff. Therefore, the trace labeled “phonon” in Figs. 5(a) and 5(b) corresponds to electrons whose last energy loss process was interaction with phonons. The thermalization distance is defined as the distance between the final and initial positions of an electron. Fig. 5(a) shows two peaks in the thermalization distance distribution located at 0 and 60 nm for the case without IEF. The first peak indicates that the initial energy of some electrons is smaller than the electron affinity and they are therefore stopped instantaneously. The main peak shifts to a distance of ~ 10 nm, when IEF are included, but the distribution still shows a long tail, which extends up to ~ 1000 nm. The decomposition of the thermalization distance distribution shows that each contribution is broadened when IEF are included. This effect is due to the fact that electrons can both lose and gain energy due to interactions with the IEF and therefore will span a wider range of kinetic energies than when IEF are not included, which results in broader distance distributions.

We note that a shorter thermalization length of 3 nm was estimated by Bizarri *et al.*¹⁷ However, no explanation or reference was given in that paper to justify this estimate. This value was then used by Williams *et al.*⁴⁵ as the initial track radius in their model of band diffusion in thermal equilibrium. The MC results obtained without internal electric fields are consistent with an analytical calculation carried out by Andrey Vasil'ev (personal communication). The analytical calculation considered the interaction of an electron with LO phonons and resulted in a diffusion length of 100 nm for an electron with initial kinetic energy of 1 eV at room temperature in CsI (Andrey Vasil'ev-personal communication). Akkerman and co-workers have published a series of theoretical studies^{41,46,47} on the ultraviolet- and x-ray-induced electron emission from CsI and other alkali halides, in which the same formulation as used in this work was employed to

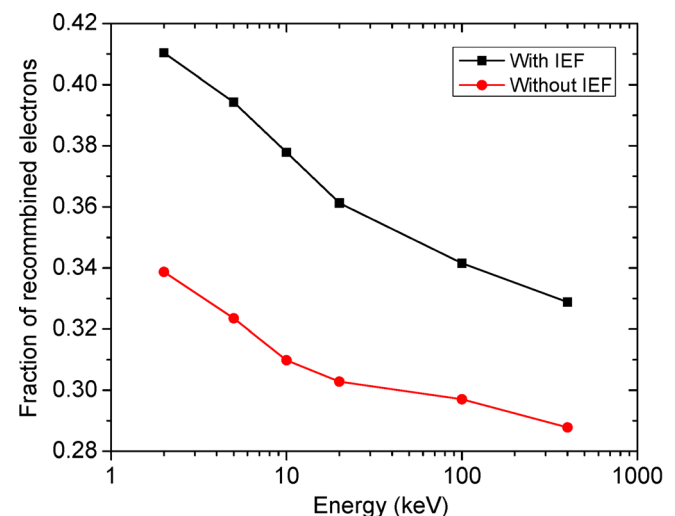


FIG. 4. (Color online) Changes of fraction of recombined electrons with incident γ -ray energy.

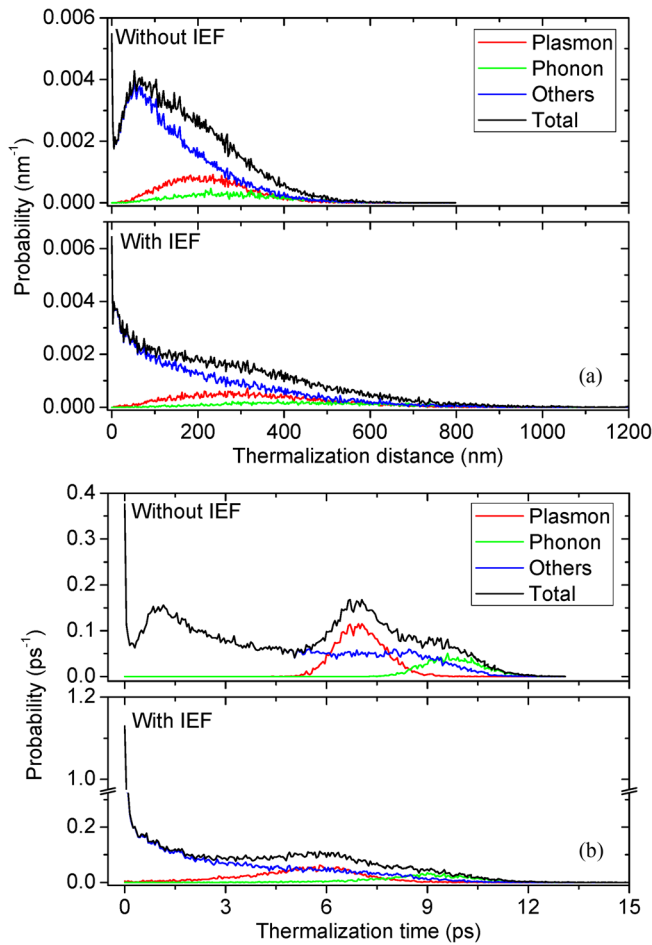


FIG. 5. (Color online) (a) Thermalization distance and (b) time distributions for a 2-keV incident γ -ray.

describe electron-phonon interactions. Their calculated results agreed well with several experimental measurements such as the quantum efficiency of a CsI photocathode as a function of its thickness⁴⁶ and the ultraviolet-induced photoelectron escape length from CsI films as a function of photon wavelength.

As can be seen from Fig. 5(b), the thermalization time distribution is more structured in the absence of IEF with four peaks located at 0, 1.00, 6.75, and 9.5 ps. The peaks at 6.75 and 9.5 ps correspond to the electrons generated through plasmon excitation and those that reached the energy cutoff after electron-phonon interactions, respectively. The peaks also shift to the left and broaden when IEF were included. This effect is due to the same reason described above in the discussion of the thermalization distance distributions. Thermalization times of approximately 10 ps or less are in accord with the time scale reported in a review by Weber¹ and a paper by Williams *et al.*¹¹ We did not find any significant energy dependence on the thermalization time and thermalization distance distributions, as shown in Fig. S3.⁴²

Figs. 6(a) and 6(b) show the spatial distributions of electrons after thermalization, without and with IEF, respectively, for a 20-keV incident γ -ray. As can be seen from these figures, the spatial distributions appear more diffuse when IEF are included. As discussed above, when IEF are considered, attractive electron-hole interactions result in a greater fraction

of recombined electrons. In addition, repulsive electron-electron interactions lead to longer thermalization distances. These two observations make the spatial distributions appear more diffuse in the presence of IEF. This is confirmed by the distribution of nearest electron-hole distances shown in Fig. 7. The distribution obtained without IEF shows two peaks centered at ~ 5 and ~ 60 nm. These two peaks also appear in the case with IEF. However, the intensity of the two peaks decreases and the distribution shows a long tail with distances up to 1000 nm. Figs. 6(c) and 6(d) also show the spatial tracks obtained after thermalization with IEF for 2- and 400-keV incident γ -ray energies, respectively. Additionally, two final electron-hole pair distributions (obtained with IEF) are given, in xyz format, in supplementary material⁴² for each of the six incident γ -ray energies considered in this work.

Current models of electron-hole pair transport generally make use of cylinder-shaped tracks with homogeneous excitation densities.^{11,17} However, an important finding of this work, illustrated in Fig. 6, is that electron-hole pair spatial distributions are highly complex. Indeed, the track formed by the immobile holes is not linear and can also be branched and the distribution of electrons, both along and away from the track of immobile holes, is not homogeneous.

In conclusion, IEF affect the electron thermalization process in several ways: (a) the fraction of recombined electrons is increased when IEF are considered, (b) the IEF affect the trajectory of the hot electrons, and (c) the thermalization distance and thermalization time distributions are broadened and shifted to the left. Therefore, we will only consider the case where IEF are included for the remainder of this work. Our simulations indicate that electron thermalization in γ -ray-irradiated CsI takes place within approximately 10 ps,

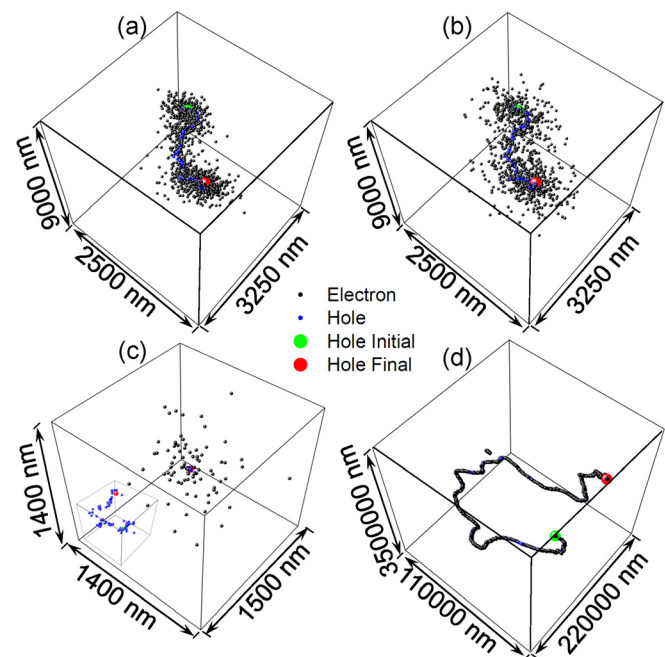


FIG. 6. (Color online) Spatial distributions of electrons and holes after thermalization (a) without and (b) with IEF for a 20-keV incident γ -ray and spatial distributions of electrons and holes after thermalization with IEF for (c) 2-keV (the insert shows a close-up of the holes only, the side length of the cube is 200 nm), and (d) 400-keV incident γ -ray energies.

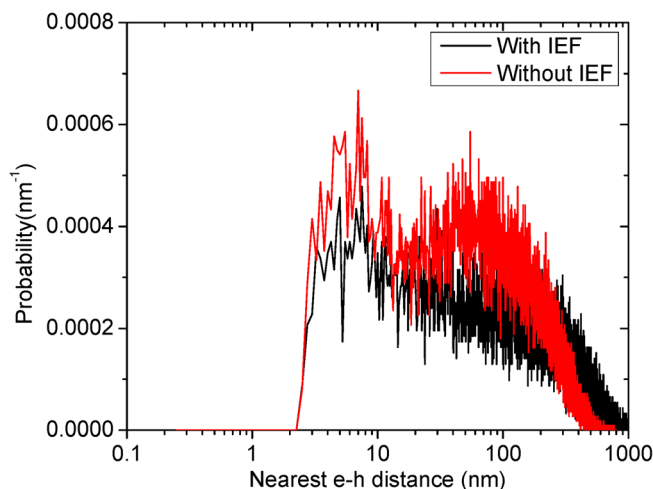


FIG. 7. (Color online) Distribution of nearest electron-hole distances for a 20-keV incident γ -ray.

that the electrons can travel distances up to several hundreds of nanometers, and that the fraction of recombined electron-hole pairs is energy dependent.

B. Tl-doped CsI

For use as a radiation detection material, CsI is commonly doped with thallium with dopant concentrations generally in the vicinity of 0.1 mol %.⁴⁸ Therefore, in this section, we investigate the effects of doping CsI with thallium on the electron thermalization process. Thallium ions act as electron traps with trapping probability set by Eq. (7). The variable γ in Eq. (7) limits the energy domain concerned by this process. There is currently no direct approach to determine the value of γ ; therefore, we evaluate, initially, the

effect of γ on the electron populations. We chose for the different values of γ multiples of 0.56, whereby a value of 0.56 translates to a factor of 10^{-3} at the cutoff energy of two band gaps ($\exp(-0.56 \times 2 \times 6.1) \sim 10^{-3}$). The larger is the multiple, the steeper the exponential factor and, therefore, the more limited the energy domain.

Fig. 8 shows the effect of γ on the proportion of each electron population (free, stopped, Tl-trapped, and recombined). The value of γ has no effect on the fraction of recombined electrons since the recombination process occurs during the very early stages of thermalization (within 2.0 ps). The fraction of Tl-trapped electrons increases with decreasing γ since a lower value of γ means that Tl sites are more attractive over a wider electron energy range. However, a large change in γ translates into a modest change in the fraction of Tl-trapped electrons. Indeed, the fraction of trapped electrons increases from 0.33 to 0.50 as γ decreases from 0.56×3.0 to 0.56×0.5 . Similarly, although the fraction of stopped electrons drops significantly when introducing Tl compared to pure CsI, it does not vary significantly with γ . For example, the fraction of stopped electrons decreases from 0.26 to 0.10 as γ decreases from 0.56×3.0 to 0.56×0.5 . Fig. 7 also shows that the difference between 0.56×1.0 and 0.56×0.5 is very small.

When a thallium ion traps an electron it becomes Tl^0 . Given that our approach for determining whether an electron has been trapped at a Tl site does not treat Tl sites explicitly, we first investigated whether this approach led to local Tl^0 concentrations that exceeded the Tl concentration, which would indicate local saturation of the Tl sites. Fig. 9 shows the distributions of Tl^0 sites, obtained with different γ values and for a Tl concentration of 0.1 mol %, as a function of the distance from the geometric center of the Tl^0 sites. The geometric center is defined as

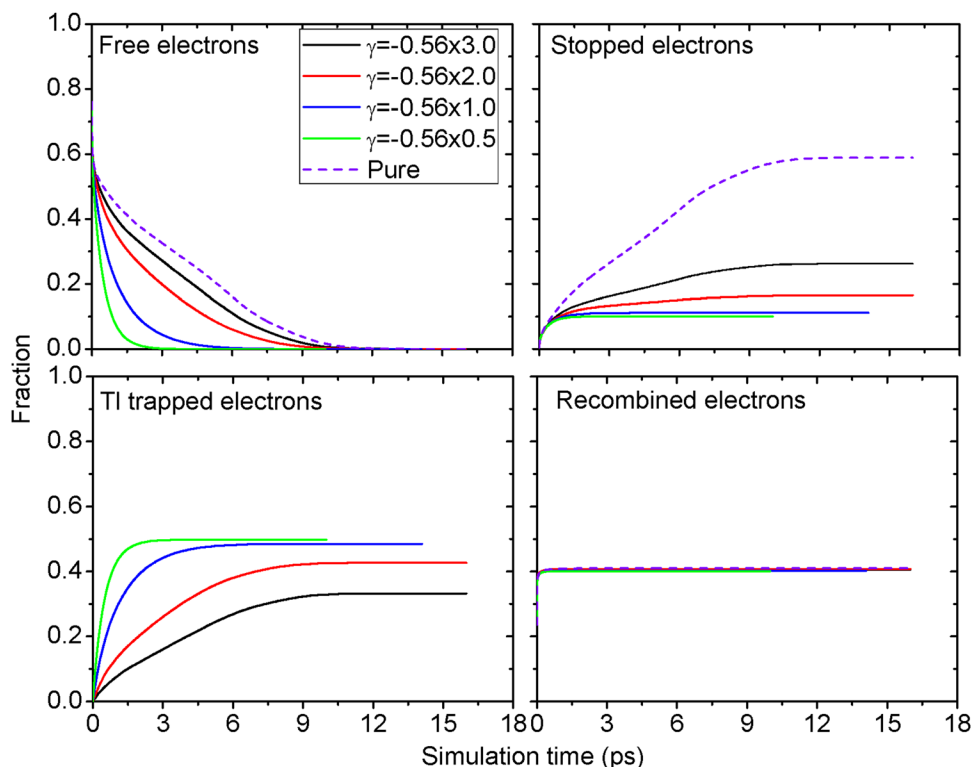


FIG. 8. (Color online) Effect of γ on the proportion of each electron population (free, stopped, Tl-trapped and recombined) for a 2-keV incident γ -ray.

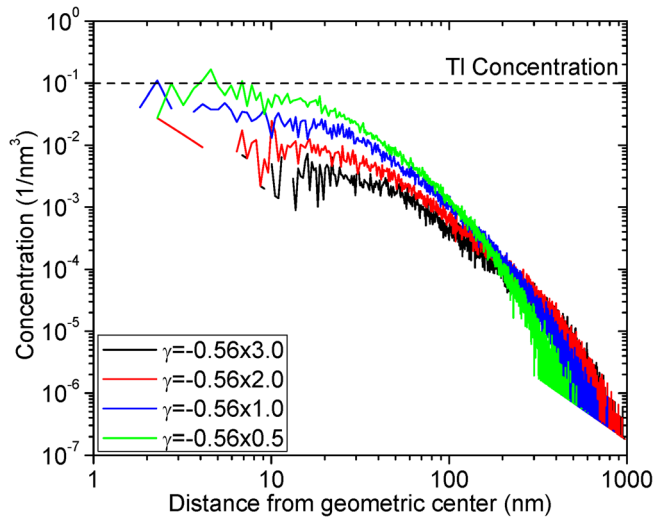


FIG. 9. (Color online) Spatial distributions of Tl^0 sites obtained with different γ values for a Tl concentration of 0.1 mol % and a 2-keV incident γ -ray energy.

$$x_c = \sum_{i=1}^N x_i / N \quad (10)$$

where x_i is the x coordinate of site i and N is the number of electrons trapped by Tl sites. y_c and z_c are defined in the same way. The concentration of Tl^0 sites between radii r_1 and r_2 can be calculated by

$$\frac{4N_i}{3\pi(r_2^3 - r_1^3)} \quad (11)$$

where N_i is the number of Tl^0 sites between radii r_1 and r_2 . The dashed line in Fig. 9 denotes the Tl concentration. Any density above the Tl concentration line would indicate that

the Tl sites are saturated in that region. Fig. 9 shows that no saturation occurs except for a narrow range of distances for $\gamma = 0.56 \times 0.5$. Therefore, based on Figs. 8 and 9, a γ value of 0.56 was selected to carry out the following simulations of electron thermalization in Tl-doped CsI.

We then investigated the effects of the Tl concentration on the thermalization process. Fig. 10 shows the electron populations as a function of time for Tl concentrations ranging from 0.001 to 0.1 mol % and a γ -ray incident energy of 2 keV. Again, as recombination occurs very early, the Tl concentration has no effect on the fraction of recombined electrons. As expected, the fraction of Tl-trapped electrons increases with increasing Tl concentration. Additional calculations were performed to determine the fraction of Tl-trapped electrons for Tl concentrations up to 1.0 mol %, as shown in Fig. 11. The fraction of Tl-trapped electrons shows an asymptotic behavior as a function of Tl concentration and this trend is not incident energy dependent as indicated by the comparing simulations performed for γ -ray incident energies of 2 keV and 20 keV. Since Tl is the primary radiative center in Tl-doped CsI, the fraction of Tl-trapped electrons is related to the intensity of photon emission. Therefore, our results are consistent with experimental observations,⁴⁹⁻⁵¹ which indicate that the light yield initially increases with increasing Tl concentration and eventually saturates at high concentrations.

Fig. 12 shows the effects of the Tl concentration on the thermalization time and distance distributions. Low Tl concentrations of 0.001 or 0.01 mol % show thermalization time and distance distributions that differ only slightly from the pure case, whereas, for Tl concentrations of 0.05 mol % and above, the thermalization time and distance distributions decay much more sharply. For example, the thermalization distance and time distributions extend to approximately 1200 nm and 15 ps, respectively, for a Tl

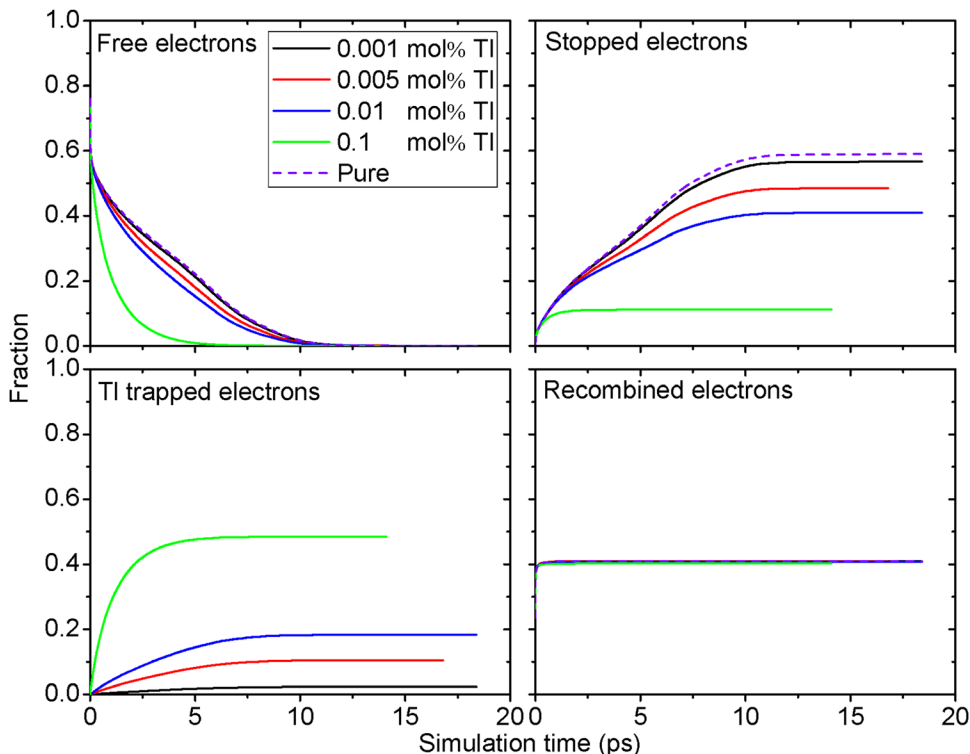


FIG. 10. (Color online) Effect of the Tl concentration on the electron populations as a function of time for a 2-keV incident γ -ray.

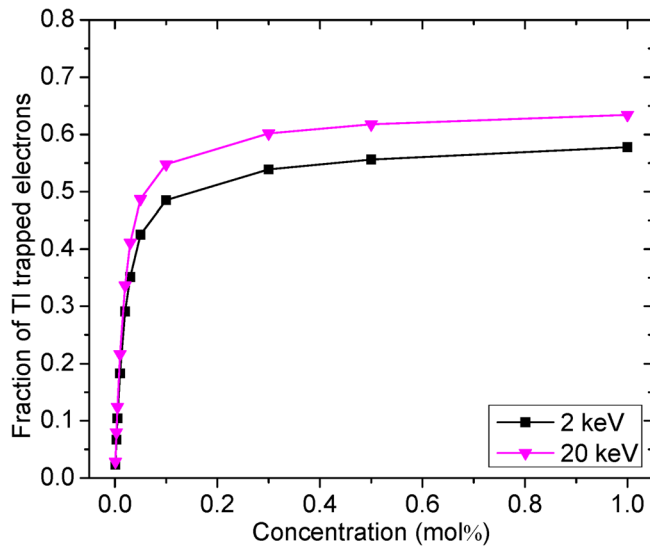


FIG. 11. (Color online) Fractions of Tl-trapped electrons as a function of Tl concentration.

concentration of 0.001 mol % and these values decrease to 400 nm and 5 ps, respectively, when the Tl concentration increases to 0.1 mol %.

Fig. 13 shows the changes in the fractions of stopped, recombined, and Tl-trapped electrons as a function of γ -ray incident energy for a Tl concentration of 0.1 mol %. The fraction of Tl-trapped electrons increases with increasing incident energy to the detriment of the fraction of recombined electrons, while the fraction of stopped electrons remains practically constant. Syntfeld-Kazuch *et al.*⁵² fitted scintillation decay curves of Tl-doped CsI excited with incident γ -ray energies ranging from 6 to 662 keV with a three-exponential function with time constants τ_1 , τ_2 , and τ_3 , referred to as the fast, slow, and tail components, respectively. Syntfeld-Kazuch *et al.* found that the intensity of the fast component decreased with increasing incident energy, whereas those of the slow and tail components increased, albeit only slightly for the slow component. The fast component, with an average time constant of 730 ± 30 ns is gener-

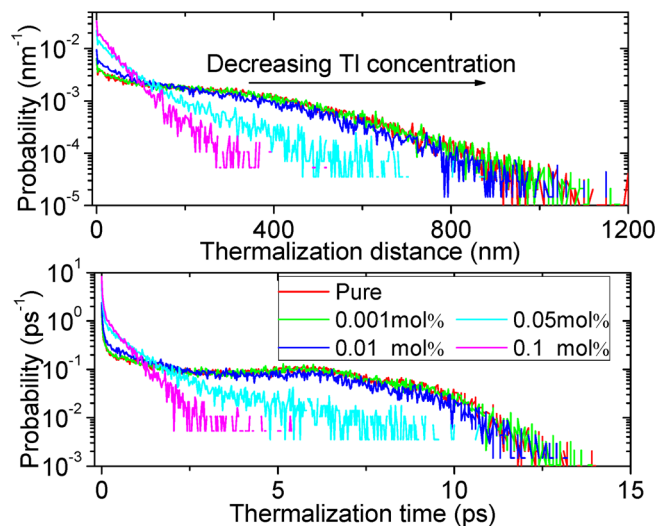


FIG. 12. (Color online) Effect of the Tl concentration on the thermalization time and distance distributions for a 2-keV incident γ -ray.

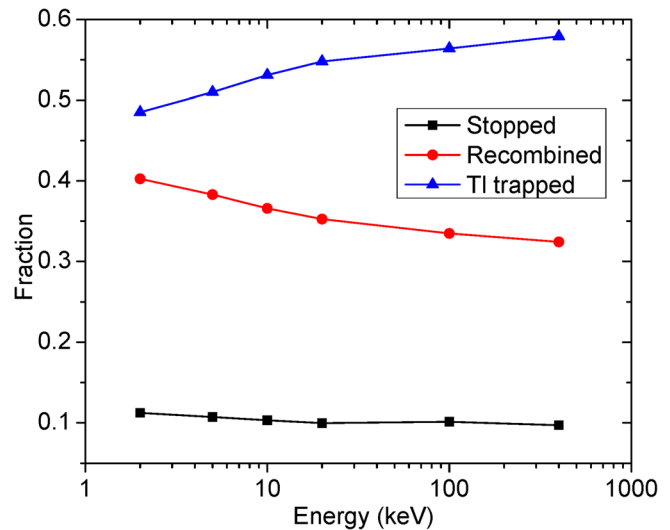


FIG. 13. (Color online) Changes in the fractions of stopped, recombined, and Tl-trapped electrons as a function of γ -ray incident energy for a Tl concentration of 0.1 mol %.

ally assigned to the prompt creation of a thallium excited state, either via nonthermal capture of an electron and a hole at the same Tl site or via exciton capture.^{50,53} Therefore, our model prediction of the decrease of the fraction of recombined electron-hole pairs (i.e., decrease in the relative number of excitons created) is consistent with the intensities of the fast component derived experimentally by Syntfeld-Kazuch *et al.* as a function of incident energy. The slow and tail components correspond to binary processes, which therefore involve the formation of a Tl^0 species. Again, our model prediction of the increase of the fraction of Tl-trapped electrons is consistent with the increasing intensities of the slow and tail components obtained by Syntfeld-Kazuch *et al.* with increasing incident energy.

IV. CONCLUSIONS

In conclusion, we have investigated the thermalization process of electrons in CsI and CsI(Tl) using Monte Carlo simulations. We found that internal electric fields can affect the electron thermalization process by increasing the likelihood for electron-hole pair recombination and by broadening the thermalization time and distance distributions. Importantly, the MC simulations indicate that electron thermalization in γ -ray-irradiated CsI takes place within approximately 10 ps and that, although a sizeable fraction of final electron-hole distances are within 10 nm, electrons can travel distances up to several hundreds of nanometers.

Doping CsI with thallium can affect the thermalization process as electrons can be trapped at Tl^+ sites to form Tl^0 species. Our results show that the thermalization time and distances diminish as the thallium concentration increases. The MC calculations show that the fraction of Tl^0 sites displays an asymptotic behavior with increasing thallium concentration, in agreement with experimental observations of the Tl concentration dependence of the light yield of CsI(Tl).

Finally, making use of the ionization tracks computed with NWEGRIM allowed us to determine the effects of the

γ -ray incident energy on the thermalization process. Such effects are important as they can point towards possible root causes for the phenomenon of nonlinearity observed for CsI and other inorganic scintillator materials. The MC calculations indicate that, for both pure and TI-doped CsI, the fraction of recombined electron-hole pairs diminishes with increasing incident energies. This result suggests that the number of STE decreases with increasing incident energy and that, therefore, the effect of STE-STE annihilation should diminish at high incident energies, in agreement with the conclusion reached in previous work.⁵

ACKNOWLEDGMENTS

The authors would like to acknowledge Professors A. Akkerman and A.N. Vasil'ev for insightful discussions. This research was supported by the National Nuclear Security Administration, Office of Nuclear Nonproliferation Research and Engineering (NA-22), of the U.S. Department of Energy (DOE).

- ¹M. J. Weber, *J. Lumin.* **100**, 35 (2002).
- ²J. E. Jaffe, D. V. Jordan, and A. J. Peurrung, *Nucl. Instrum. Methods A* **570**, 72 (2007).
- ³M. Moszyński, *Nucl. Instrum. Methods Phys. Res. A* **505**, 101 (2003).
- ⁴M. Moszyński, J. Zalipska, M. Balcerzyk, M. Kapusta, W. Mengesha, and J. D. Valentine, *Nucl. Instrum. Methods Phys. Res. A* **484**, 259 (2002).
- ⁵S. Kerisit, K. M. Rosso, B. D. Cannon, F. Gao, and Y. Xie, *J. Appl. Phys.* **105**, 114915 (2009).
- ⁶P. Dorenbos, J. T. M. de Haas, and C. W. E. van Eijk, *IEEE Trans. Nucl. Sci.* **42**, 2190 (1995).
- ⁷W. W. Moses, S. A. Payne, W.-S. Choong, G. Hull, and B. W. Reutter, *IEEE Trans. Nucl. Sci.* **55**, 1049 (2008).
- ⁸R. B. Murray and A. Meyer, *Phys. Rev.* **122**, 815 (1961).
- ⁹R. T. Williams, K. B. Ucer, J. Q. Grim, K. C. Lipke, L. M. Trefilova, and W. W. Moses, *IEEE Trans. Nucl. Sci.* **57**, 1187 (2010).
- ¹⁰R. T. Williams, J. Q. Grim, Q. Li, K. B. Ucer, and W. W. Moses, *Phys. Status Solidi B* **248**, 426 (2011).
- ¹¹R. T. Williams, Q. Li, J. Q. Grim, K. B. Ucer, G. Bizarri, and W. W. Moses, *Proc. SPIE* **7805**, 78050K (2010).
- ¹²R. Hill, *Br. J. Appl. Phys.* **17**, 1385 (1966).
- ¹³R. Hill and A. J. L. Collinson, *Br. J. Appl. Phys.* **17**, 1377 (1966).
- ¹⁴S. A. Payne, N. J. Cherepy, G. Hull, J. D. Valentine, W. W. Moses, and W.-S. Choong, *IEEE Trans. Nucl. Sci.* **56**, 2506 (2009).
- ¹⁵G. Bizarri, W. W. Moses, J. Singh, A. N. Vasil'ev, and R. T. Williams, *Phys. Status Solidi. C* **6**, 97 (2009).
- ¹⁶G. Bizarri, W. W. Moses, J. Singh, A. N. Vasil'ev, and R. T. Williams, *J. Lumin.* **129**, 1790 (2009).
- ¹⁷G. Bizarri, W. W. Moses, J. Singh, A. N. Vasil'ev, and R. T. Williams, *J. Appl. Phys.* **105**, 044507 (2009).
- ¹⁸S. Kerisit, K. M. Rosso, and B. D. Cannon, *IEEE Trans. Nucl. Sci.* **55**, 1251 (2008).
- ¹⁹D. W. Aitken, B. L. Beron, G. Yenicay, and H. R. Zulliger, *IEEE Trans. Nucl. Sci.* **14**, 468 (1967).
- ²⁰W. Mengesha, T. D. Taulbee, B. D. Rooney, and J. D. Valentine, *IEEE Trans. Nucl. Sci.* **45**, 456 (1998).
- ²¹M. Moszyński, A. Nassalski, A. Syntfeld-Kazuch, Ł. Swiderski, and T. Szcześniak, *IEEE Trans. Nucl. Sci.* **55**, 1062 (2008).
- ²²M. Moszyński, M. Balcerzyk, W. Czarnacki, M. Kapusta, W. Klamra, P. Schotanus, A. Syntfeld, M. Szawlowski, and V. Kozlov, *Nucl. Instrum. Methods A* **537**, 357 (2005).
- ²³R. Shimizu and D. Ze-Jun, *Rep. Prog. Phys.* **55**, 487 (1992).
- ²⁴R. M. Van Ginhoven, J. E. Jaffe, S. Kerisit, and K. M. Rosso, *IEEE Trans. Nucl. Sci.* **57**, 2303 (2010).
- ²⁵J. P. Ganachaud, C. Attard, and R. Renoud, *Phys. Status Solidi B* **199**, 175 (1997).
- ²⁶F. Gao, L. W. Campbell, R. Devanathan, Y. Xie, L. R. Corrales, A. J. Peurrung, and W. J. Weber, *Nucl. Instrum. Methods A* **579**, 292 (2007).
- ²⁷F. Gao, L. W. Campbell, R. Devanathan, Y. Xie, Y. Zhang, A. J. Peurrung, and W. J. Weber, *Nucl. Instrum. Methods B* **255**, 286 (2007).
- ²⁸F. Gao, L. W. Campbell, Y. Xie, R. Devanathan, A. J. Peurrung, and W. J. Weber, *IEEE Trans. Nucl. Sci.* **55**, 1079 (2008).
- ²⁹C. Amsler, D. Grögler, W. Joffrain, D. Lindelöf, M. Marchesotti, P. Niederberger, H. Pruys, C. Regenfus, P. Riedler, and A. Rotondi, *Nucl. Instrum. Methods A* **480**, 494 (2002).
- ³⁰E. Sakai, *IEEE Trans. Nucl. Sci.* **34**, 418 (1987).
- ³¹I. Holl, E. Lorenz, and G. Mageras, *IEEE Trans. Nucl. Sci.* **35**, 105 (1988).
- ³²J. D. Valentine, W. W. Moses, S. E. Derenzo, D. K. Wehe, and G. F. Knoll, *Nucl. Instrum. Methods A* **325**, 147 (1993).
- ³³J. T. M. de Haas, P. Dorenbos, and C. W. E. Van Eijk, *Nucl. Instrum. Methods A* **537**, 97 (2005).
- ³⁴M. Moszyński, M. Kapusta, M. Mayhugh, D. Wolski, and S. O. Flyckt, *IEEE Trans. Nucl. Sci.* **44**, 1052 (1997).
- ³⁵S. Sasaki, H. Tawara, K. Saito, M. Miyajima, and E. Shibamura, *Jpn. J. Appl. Phys.* **45**, 6420 (2006).
- ³⁶J. D. Valentine, D. K. Wehe, G. F. Knoll, and C. E. Moss, *IEEE Trans. Nucl. Sci.* **40**, 1267 (1993).
- ³⁷M. Moszyński, W. Czarnacki, W. Klamra, M. Szawlowski, P. Schotanus, and M. Kapusta, *Nucl. Instrum. Methods A* **504**, 307 (2003).
- ³⁸J. Llacer and E. L. Garwin, *J. Appl. Phys.* **40**, 2766 (1969).
- ³⁹M. Sparks, D. L. Mills, R. Warren, T. Holstein, A. A. Maradudin, L. J. Sham, E. Loh, Jr., and D. F. King, *Phys. Rev. B* **24**, 3519 (1981).
- ⁴⁰J. N. Bradford and S. Woolf, *J. Appl. Phys.* **70**, 490 (1991).
- ⁴¹T. Boutboul, A. Akkerman, A. Gibrekhterman, A. Breskin, and R. Chechik, *J. Appl. Phys.* **86**, 5841 (1999).
- ⁴²See supplementary material at <http://dx.doi.org/10.1063/1.3632969> for the formulation and parameters employed to model electron thermalization, electron population plots obtained for a series of integration time steps and incident γ -ray energies, and thermalization time and distance distributions obtained for different incident γ -ray energies and for two thermalized electron-hole pair distributions in xyz format for each incident γ -ray energy.
- ⁴³R. T. Williams, J. N. Bradford, and W. L. Faust, *Phys. Rev. B* **18**, 7038 (1978).
- ⁴⁴P. Martin, S. Guizard, P. Daguzan, G. Petite, P. D'Oliveira, P. Meynadier, and M. Perdrix, *Phys. Rev. B* **55**, 5799 (1997).
- ⁴⁵R. T. Williams, Q. Li, J. Q. Grim, K. B. Ucer, G. A. Bizarri, and W. W. Moses, in *Hard X-Ray, Gamma-Ray, and Neutron Detector Physics XII*; Vol. 7805, edited by A. Burger, L. A. Franks, and R. B. James (SPIE-International Society Optical Engineering, Bellingham, 2010).
- ⁴⁶A. Akkerman, T. Boutboul, A. Breskin, R. Chechik, and A. Gibrekhterman, *J. Appl. Phys.* **76**, 4656 (1994).
- ⁴⁷T. Boutboul, A. Akkerman, A. Breskin, and R. Chechik, *J. Appl. Phys.* **84**, 2890 (1998).
- ⁴⁸F. Benrachi, B. Chambon, B. Cheynis, D. Drain, C. Pastor, D. Seghier, K. Zaid, A. Giorni, D. Heuer, A. Lleres, C. Morand, P. Stassi, and J. B. Viano, *Nucl. Instrum. Methods Phys. Res. A* **281**, 137 (1989).
- ⁴⁹R. Gwin and R. B. Murray, *Phys. Rev.* **131**, 501 (1963).
- ⁵⁰M. M. Hamada, F. E. Costa, M. C. C. Pereira, and S. Kubota, *IEEE Trans. Nucl. Sci.* **48**, 1148 (2001).
- ⁵¹P. Schotanus, R. Kamermans, and P. Dorenbos, *IEEE Trans. Nucl. Sci.* **37**, 177 (1990).
- ⁵²A. Syntfeld-Kazuch, M. Moszyński, Ł. Swiderski, W. Klamra, and A. Nassalski, *IEEE Trans. Nucl. Sci.* **55**, 1246 (2008).
- ⁵³H. B. Dietrich and R. B. Murray, *J. Lumin.* **5**, 155 (1972).

Monte Carlo simulations of electron thermalization in alkali iodide and alkaline-earth fluoride scintillators

Zhiguo Wang, YuLong Xie, Luke W. Campbell, Fei Gao, and Sebastien Kerisit

Citation: *J. Appl. Phys.* **112**, 014906 (2012); doi: 10.1063/1.4736088

View online: <http://dx.doi.org/10.1063/1.4736088>

View Table of Contents: <http://jap.aip.org/resource/1/JAPIAU/v112/i1>

Published by the [American Institute of Physics](#).

Related Articles

Monte Carlo code G3sim for simulation of plastic scintillator detectors with wavelength shifter fiber readout
[Rev. Sci. Instrum.](#) **83**, 043301 (2012)

X-ray detection capability of a BaCl₂ single crystal scintillator
[J. Appl. Phys.](#) **111**, 024906 (2012)

A new detector for mass spectrometry: Direct detection of low energy ions using a multi-pixel photon counter
[Rev. Sci. Instrum.](#) **83**, 013304 (2012)

Comment on "Securing special nuclear material: Recent advances in neutron detection and their role in nonproliferation" [*J. Appl. Phys.* **108**, 111101 (2010)]
[J. Appl. Phys.](#) **111**, 016104 (2012)

Comment on "Securing special nuclear material: Recent advances in neutron detection and their role in nonproliferation" [*J. Appl. Phys.* **108**, 111101 (2010)]
[App. Phys. Rev.](#) **2012**, 1 (2012)

Additional information on *J. Appl. Phys.*

Journal Homepage: <http://jap.aip.org/>

Journal Information: http://jap.aip.org/about/about_the_journal

Top downloads: http://jap.aip.org/features/most_downloaded

Information for Authors: <http://jap.aip.org/authors>

ADVERTISEMENT

AIP Advances

Special Topic Section:
PHYSICS OF CANCER

Why cancer? Why physics? [View Articles Now](#)

Monte Carlo simulations of electron thermalization in alkali iodide and alkaline-earth fluoride scintillators

Zhiguo Wang,^{1,a)} YuLong Xie,² Luke W. Campbell,³ Fei Gao,¹ and Sebastien Kerisit^{1,a)}

¹*Fundamental and Computational Sciences Directorate, Pacific Northwest National Laboratory, Richland, Washington 99352, USA*

²*Energy and Environment Directorate, Pacific Northwest National Laboratory, Richland, Washington 99352, USA*

³*National Security Directorate, Pacific Northwest National Laboratory, Richland, Washington 99352, USA*

(Received 3 February 2012; accepted 9 June 2012; published online 11 July 2012)

A Monte Carlo model of electron thermalization in inorganic scintillators, which was developed and applied to CsI in a previous publication [Wang *et al.*, *J. Appl. Phys.* **110**, 064903 (2011)], is extended to another material of the alkali halide class, NaI, and to two materials from the alkaline-earth halide class, CaF₂ and BaF₂. This model includes electron scattering with both longitudinal optical (LO) and acoustic phonons as well as the effects of internal electric fields. For the four pure materials, a significant fraction of the electrons recombine with self-trapped holes and the thermalization distance distributions of the electrons that do not recombine peak between approximately 25 and 50 nm and extend up to a few hundreds of nanometers. The thermalization time distributions of CaF₂, BaF₂, NaI, and CsI extend to approximately 0.5, 1, 2, and 7 ps, respectively. The simulations show that the LO phonon energy is a key factor that affects the electron thermalization process. Indeed, the higher the LO phonon energy is, the shorter the thermalization time and distance are. The thermalization time and distance distributions show no dependence on the incident γ -ray energy. The four materials also show different extents of electron-hole pair recombination due mostly to differences in their electron mean free paths (MFPs), LO phonon energies, initial densities of electron-hole pairs, and static dielectric constants. The effect of thallium doping is also investigated for CsI and NaI as these materials are often doped with activators. Comparison between CsI and NaI shows that both the larger size of Cs⁺ relative to Na⁺, i.e., the greater atomic density of NaI, and the longer electron mean free path in NaI compared to CsI contribute to an increased probability for electron trapping at Tl sites in NaI versus CsI. © 2012 American Institute of Physics. [<http://dx.doi.org/10.1063/1.4736088>]

I. INTRODUCTION

Inorganic scintillators are widely used as radiation detection materials for nuclear non-proliferation, medical imaging, geological exploration, and many other applications. For γ -ray spectroscopy, the achievable energy resolution is one of the most important characteristics of a scintillator material. There is, therefore, a continuous interest in the development of new scintillator materials with improved energy resolution. The energy resolution achievable with a given scintillator material is principally dependent on the efficiency of conversion of electron-hole pairs into scintillation light. However, for most scintillator materials, it has been observed that the efficiency of this process, and therefore ultimately the material's light yield per unit of incident energy, depends on the energy of the incident radiation. As a result, many inorganic scintillators display some degree of light yield nonlinearity (also often referred to as "nonproportionality") following γ -ray excitation,¹ which degrades their achievable energy resolution.

Scintillation in inorganic scintillators is commonly divided into the following three steps: (1) the electron cascade,

that is, the production of electron-hole pairs, (2) thermalization, whereby the electrons and holes thermalize to the bottom of the conduction band and the top of the valence band, respectively, and (3) radiative emission either via the recombination of electron-hole pairs at lattice sites or through energy transfer to luminescence centers. Nonlinearity is believed to stem from the fact that the density of electron-hole pairs is energy dependent and that nonradiative processes depend nonlinearly on the density of electron-hole pairs.^{1–10} However, the physical processes that give rise to nonlinearity and how each of the three steps described above contribute to nonlinearity are not fully understood. Consequently, a realistic description of the electron-hole pair density along the ionization track as a function of incident energy is required to accurately determine the processes that contribute to nonlinearity.

A Monte Carlo (MC) code developed at the Pacific Northwest National Laboratory (PNNL), NWEGRIM (northwest electron and gamma ray interaction in matter),^{11–14} has been designed to calculate the fate of individual electron-hole pairs down to energies on the order of the band gap and can, therefore, compute the microscopic structure of ionization tracks. Electron-hole pair spatial distributions calculated by NWEGRIM were used previously to study a hypothesized process that may give rise to nonlinearity, namely, annihilation between

^{a)}Authors to whom correspondence should be addressed. Electronic addresses: sebastien.kerisit@pnnl.gov and zhiguo.wang@pnnl.gov.

self-trapped excitons (STEs), in two scintillator materials (CsI and LaBr_3) using a kinetic Monte Carlo (KMC) model.^{2,15} Comparison of experimental and calculated relative light yields as a function of incident energy indicated that this process could indeed account for the initial rise in relative light yield with increasing incident energy for both materials. However, the thermalization step mentioned above was not included in that study. Therefore, a MC program that simulates electron-phonon interactions and uses the electron-hole pair spatial distributions generated by NWEGRIM was implemented and applied to pure and Tl-doped CsI.¹⁶ These simulations predicted that, in CsI, electron thermalization takes place within approximately 10 ps following γ -ray excitation and that the electron thermalization distance distributions peak at a few tens of nanometers and can extend up to several hundreds of nanometers.

Since the discovery of NaI(Tl) as a scintillation crystal in 1948,¹⁷ many compounds have been developed as scintillator materials. In addition, there are large variations in the properties of these materials thus allowing one to choose a material that is optimum for a particular application. As a result, several scintillator materials from different scintillator classes (e.g., alkali halides, alkaline-earth halides, oxides, silicates) are currently in use. It is, therefore, important to evaluate to what extent the thermalization process varies among materials of a same class and among different classes of scintillators. In the present work, we further develop the MC model of electron thermalization and apply it to another material of the alkali halide class, NaI, and to two materials from the alkaline-earth halide class, CaF_2 and BaF_2 . The results obtained with these three materials will be compared with those obtained with CsI. It should be noted that the thermalization calculations in CsI were repeated in this work as a few parameters were modified from previously reported calculations;¹⁶ however, these modifications only caused minor quantitative changes and, therefore, did not affect the conclusions of the previous findings.

NaI(Tl) and CsI(Tl) are important and common scintillation materials due to their high detection efficiency and spectral resolution. The light yields of CaF_2 and BaF_2 are rather low compared to those of NaI(Tl) and CsI(Tl); however, BaF_2 is a fast scintillator, which can be used in situations where fast scintillating is required¹⁸ and CaF_2 , which is commonly doped with Eu, has many attractive properties as it is non-toxic, non-hygroscopic, and relatively inert.¹⁹ Finally, it should be noted that one important common character of these materials is that they all show light yield nonlinearity.

II. COMPUTATIONAL METHODS

A. Thermalization process

In this section, we give a brief description of the MC algorithm used to model the thermalization process; a detailed discussion of the thermalization model is given in our previous publication.¹⁶ Spatial distributions of electron-hole pairs generated by γ -ray excitation, as computed by NWEGRIM, were used as input to the simulations. The reader is referred to previous publications^{11–14} for details of the methodology used by NWEGRIM. Six incident γ -ray energies were considered in this work: 2, 5, 10, 20, 100, and 400 keV, and the numbers of simulations, for each incident energy, were 400, 200, 100, 50, 10, and 5, respectively.

The kinetic energies of the electrons at the end of the electron cascade, as calculated by NWEGRIM, were used as input to the simulations. The holes are assumed to self trap instantaneously and to be immobile after the electron cascade. Fig. 1 shows the kinetic energy distributions of the electrons at the end of the electron cascade for 2-keV incident γ -rays and for the four materials of interest. The kinetic energies were measured from the conduction band minimum. The kinetic energy distributions for the other γ -ray incident energies considered in this work are essentially identical to that obtained at 2 keV (data not shown), as observed in our previous study.¹⁶ There are two noticeable features. The high and

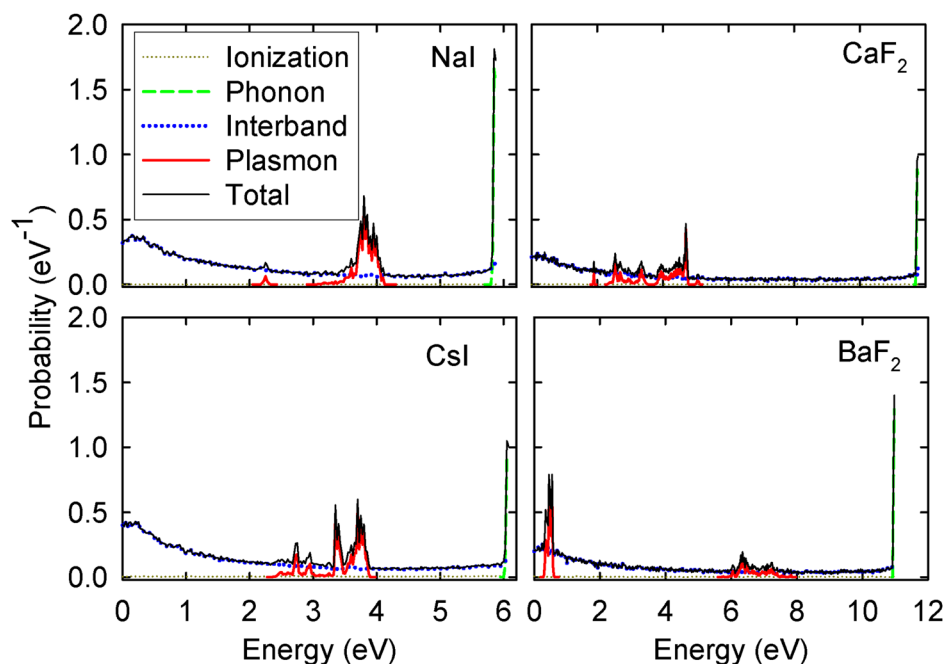


FIG. 1. Kinetic energy distributions of the electrons at the end of the electron cascade for an incident γ -ray energy of 2 keV.

narrow peak at the upper range of non-ionizing kinetic energies is due to electron interactions with phonons. We note that electron-phonon interactions cannot create electron-hole pairs but that energy loss to phonons can bring the electron energy below the energy cutoff. The fine kinetic energy structure is due to electron-hole pairs created via plasmon decay. In our previous publication,¹⁶ a single characteristic plasmon excitation energy was used in NWEGRIM, leading to a large spike in the kinetic energy distribution. In this work, NWEGRIM was modified to include an improved algorithm for simulating plasmon decay.

Plasmons are collective excitations of the electron-ion interaction that we simulated using a screening model in the random phase approximation appropriate to crystals as derived by Adler²⁰ and Wiser.²¹ The ground state electronic structure of the medium was computed using the ABINIT code²² and the band energies adjusted with GW calculations.²³ Any given electronic excitation of a specified energy and momentum transfer arises from a sum over individual particle-hole transitions; these transitions are the decay products of that excitation and their relative weights in the sum thus directly give their un-normalized decay spectrum. After computing the screening, the peak of the zero momentum transfer plasmon excitation was identified and the energy spectrum of decay conduction electrons at this energy was calculated by summing over all directions of the secondary particles in the limit of no local fields (local fields were included in the screening calculations). In BaF₂, a weak but sharp valence-only plasmon was identified along with a separate but much stronger and broader plasmon arising from the combined screening of the valence and semi-core orbitals. For this material, we approximated the plasmon interaction as arising only from the second, stronger peak. This work will be described in more detail in a later publication.

Four electron-phonon interactions were considered, namely, longitudinal optical (LO) phonon emission, LO phonon absorption, acoustic (A) phonon emission, and A phonon absorption. At each simulation step, an electron-phonon interaction is selected with a probability proportional to its scattering rate. In addition, every 10⁻¹⁶s, all the electrons are moved under the influence of the internal electric field. Details of the approach used to model the internal electric field are given in our previous publication.¹⁶ Every time an electron is moved, its new position and energy are used to

evaluate whether it has stopped, recombined with a hole, or trapped at a thallium site. An electron is stopped when its energy becomes lower than a cutoff energy. In our previous publication,¹⁶ the material's electron affinity was used as the cutoff energy as was done in the simulations of Akkerman and co-workers.^{24,25} However, the thermal energy is now used as the energy cutoff, as it was deemed more appropriate for our simulations. An electron recombines with a hole if its kinetic energy is lower than the electrostatic energy between this electron and the nearest hole or if the distance to the nearest hole is less than the self-trapped hole radius. An electron is trapped at a thallium site if a randomly drawn number is less than the energy-dependent probability for electron capture, $P_{trap}(E)$ ²⁶

$$P_{trap}(E) = \frac{\delta}{a} \times f(Tl) e^{-\gamma E}, \quad (1)$$

where E is the electron energy, δ is the electron step length, a is the material's lattice constant, $f(Tl)$ is the fraction of unit cells occupied by a thallium atom, and γ is a constant that limits the energy domain concerned by this process.

The scattering rates, scattering angles, and inverse mean free paths (MFPs) for emission and absorption of LO and A phonons were calculated using the formulations of Llacer and Garwin²⁷ and Sparks *et al.*,²⁸ respectively. The formulation for the electron-A phonon interactions also included the correction of Bradford and Woolf.²⁹ The formulations used in this work are summarized in supporting information (SI).³⁰ The scattering rates thus obtained for all four materials are shown in Fig. 2. To calculate the energy of the emitted or absorbed acoustic phonon, $\hbar\omega_A$, the approach described by Fischetti *et al.*³¹ was employed to determine the acoustic phonon wave vector, q , knowing the energy E of the electron that is creating or annihilating the acoustic phonon. This approach involves inverting the probability function $P(q)$ using the rejection technique whereby

$$P(q) = \frac{\int_0^q dq' p(q')}{\int_0^{q_{max}^\pm} dq' p(q')}, \quad (2)$$

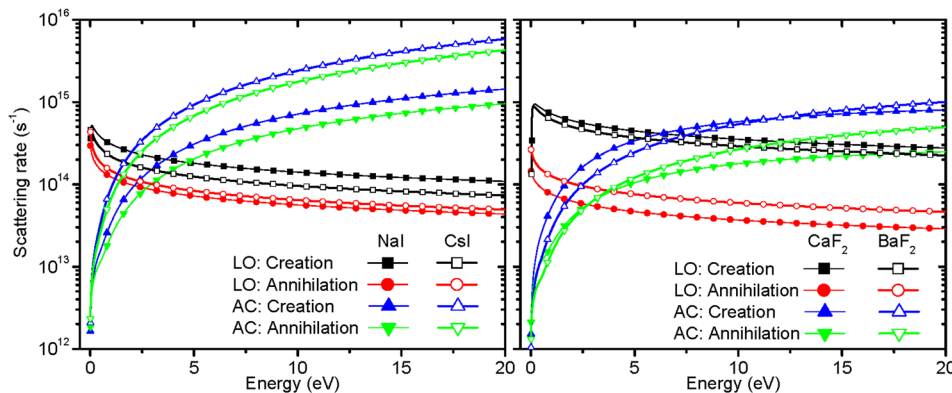


FIG. 2. Electron-phonon scattering rates as a function of electron energy.

TABLE I. Primary and secondary model parameters.

Parameters	Definition	NaI	CsI	CaF ₂	BaF ₂
Primary parameters					
a_0 (nm)	Lattice constant	0.646	0.457	0.546	0.62
ϵ_∞	Optical dielectric constant	2.9 ^a	3.0 ^a	2.02 ^b	2.12 ^b
ϵ_0	Static dielectric constant	7.3 ^a	5.65 ^a	6.80 ^c	7.36 ^c
C_{11} (GPa)	Elastic constant	29.3 ^d	24.3 ^c	164.0 ^f	89.2 ^g
C_{12} (GPa)	Elastic constant	7.8 ^d	6.4 ^c	50.0 ^f	40.0 ^g
C_{44} (GPa)	Elastic constant	7.4 ^d	6.3 ^c	34.7 ^f	25.4 ^g
$\hbar\omega_{LO}$ (eV)	LO phonon energy	0.023 ^a	0.01 ^a	0.0565 ^h	0.0396 ^h
σ (10^{-19} m ²)	Integrated cross section at exciton energy	2.91	6.76	4.13	4.56
E (eV)	Exciton energy	5.61 ⁱ	5.3 ⁱ	11.0 ^j	9.8 ^j
d_{h-h} (nm)	Distance between two halide ions in the h_2^- molecular ion	0.345	0.325	0.19	0.19
Secondary parameters					
E_{BZ} (eV)	Electron kinetic energy of electron (Brillouin zone)	3.495	2.772	4.893	3.794
k_{BZ} (10^9 m ⁻¹)	Equivalent radius of first Brillouin zone	9.58	8.53	11.33	9.98
C_m (10^{-20} m ²)	Primitive cell mass correction factor	0.197	1.31	0.74	0.28
m^*/m	Electron effective mass	1.8	1.9	1.9	2.0
S (eV)	Matrix element for A phonon-electron interaction	0.60	0.61	1.32	0.87
C_S (m·s ⁻¹)	Effective speed of sound in material	1627	1390	3947	2701
α (nm ⁻¹)	Screening correction parameter	77.0	128.1	41.1	69.8

^aReference 34^bReference 42^cReference 43^dReference 44^eReference 45^fReference 46^gReference 47^hReference 48ⁱReference 49^jReference 50.

where $p(q')$ is the content of the integral in Eq. (4) or (5) of the SI.³⁰ We note that plots of $P(q)$ as a function of q/q_{\max} are very similar for all values of E (E determines q_{\max} as shown in Eq. (7) of the SI³⁰). Therefore, to save computational time, a single representative value of E was used to calculate the values of $P(q)$ over the interval 0 to 1 only once prior to the start of the simulation. Because the initial electron kinetic energies are distributed between 0 and E_g from the conduction band minimum, $E_g/2$ was used as the representative energy. For emitted or absorbed LO phonons, the dispersion was ignored and a single characteristic energy was used.

B. Origin of the model parameters

The approach used in this work and described in Sec. II A makes use of a series of parameters, which can be divided into two classes (Table I). The first class of parameters consists of those taken from experimental data or quantum mechanical calculations and will be referred to as primary parameters. The second class of parameters, referred to as secondary parameters, consists of the parameters for which no experimental or quantum mechanical data is available and that have to be determined from the primary parameters. The sources of the values of the primary parameters and the formulations used to determine the secondary parameters are very important aspects of the thermalization model. Therefore, both sets of parameters as well as the sources for the

primary parameters are given in Table I and the formulations used to obtain the secondary parameters are discussed below.

In our previous publication,¹⁶ the free electron mass, m_0 , was used as an approximation for the electron effective mass, m^* . In the present work, m^* is determined using Fröhlich's theory

$$\frac{m^*}{m_0} = 1 + \frac{\beta}{6}, \quad (3)$$

where β is given by

$$\beta = e^2 \frac{1}{4\pi\epsilon} \left[\frac{1}{\epsilon_\infty} - \frac{1}{\epsilon_0} \right] \sqrt{\frac{m_0}{2\hbar^2(\hbar\omega_{LO})}}, \quad (4)$$

where ϵ is the vacuum permittivity, e is the elementary charge, \hbar is the Planck constant, ω_{LO} is LO phonon frequency, and ϵ_∞ and ϵ_0 are the optical and static dielectric constants, respectively. This method was applied to several alkali halides (CsI, KI, RbI, NaI, and CsBr) by Akkerman and co-workers in their study of the escape length of photo-induced electrons from thin films.²⁴

The electron-acoustic phonon interaction matrix element is assumed to be independent of the momentum transfer and was determined by Eq. (5), as applied to SiO₂ by Fischetti³²

$$|\vec{S}(q)|^2 \cong (\pi\hbar^4 N^2/m^{*2})\sigma, \quad (5)$$

where σ is the integrated cross section for electron scattering at the exciton energy following Sparks *et al.*²⁸ and N is the atomic density. The integrated cross sections of CsI, NaI, CaF₂, and BaF₂ were determined using the electron-ion scattering cross sections calculated by the FEFF8 code.³³ As for the electron effective mass, the same method was applied to a series of alkali halides by Akkerman and co-workers.^{24,34}

Although the formulation introduced by Sparks *et al.*²⁸ for the interaction between electrons and acoustic phonons is appropriate for low electron energies, the calculated scattering rates become unphysical as the electron energy increases beyond the energy of the first Brillouin zone. Therefore, as introduced by Bradford and Woolf,²⁹ the correction factor $\{1/[1+(q^2/\alpha^2)]\}^2$ was added into the integrand of the electron-acoustic phonon scattering rate, as shown in Eqs. (3) and (4) of the SI,³⁰ where q is the phonon momentum and α is the screening correction parameter. We used the same approach used by Bradford and Woolf²⁹ to determine the value of α , i.e., by requiring that

$$\lim_{q \rightarrow 0} \left(\frac{4\pi}{V_c} \left(\frac{1}{4\pi\epsilon_0} Z_1 Z_2 e^2 \right) \frac{1}{\alpha^2 + q^2} \right) = S, \quad (6)$$

where V_c is the unit cell volume, $Z_1 = 1$, Z_2 is atomic number of the dominant scattering atom (the anion for the alkali iodides and the cation for the alkaline-earth fluorides), and S is the electron-acoustic phonon interaction matrix element.

The effective speed of sound C_s was calculated using the elastic theory^{31,35}

$$\frac{3}{C_s} = \frac{2}{C_t} + \frac{1}{C_l}, \quad (7)$$

where C_t and C_l are the transverse and longitudinal sound velocities, respectively, which are calculated by³⁵

$$C_l = \sqrt{\frac{\frac{1}{3}(C_{11} + 2C_{12} + 4C_{44})}{\rho}}, \quad (8)$$

$$C_t = \sqrt{\frac{\frac{1}{3}(C_{11} - C_{12} + C_{44})}{\rho}},$$

where C_{11} , C_{12} , and C_{44} are the elastic constants. Experimental data for the effective speed of sound in CaF₂ and BaF₂ are available³⁶ (3730–3800 and 2430–2450 m·s⁻¹, respectively) and are in good agreement with those calculated here (3947 and 2701 m·s⁻¹, respectively).

As was done by Fischetti *et al.*³¹ and Ashley *et al.*³⁷ for SiO₂ and by Sparks *et al.*²⁸ for NaCl, the electron energy at the boundary of the first Brillouin zone, E_{BZ} , was calculated using the equivalent spherical radius, k_{BZ}

$$E_{BZ} = \hbar^2 k_{BZ}^2 / m^*, \quad (9)$$

where

$$k_{BZ} = (6\pi^2/V_p)^{1/3}, \quad (10)$$

and where V_p is the volume of the primitive cell.

Finally, the primitive cell mass correction factor, $f(q)$, which describes the variation of the mass M from the mass of the primitive cell, M_p , for small q , to the mass of the heaviest constituent (M_H) for $q \geq k_{BZ}$, was calculated as proposed by Ashley *et al.*³⁷ to extrapolate between the small q and $q \geq k_{BZ}$ limits described by Sparks *et al.*²⁸

$$f(q) = \begin{cases} 1 + C_m q^2, & q < k_{BZ} \\ 1 + C_m k_{BZ}^2, & q \geq k_{BZ} \end{cases}, \quad (11)$$

where

$$C_m = \left(\frac{M_p}{M_H} - 1 \right) / k_{BZ}^2. \quad (12)$$

III. RESULTS AND DISCUSSION

A. Pure materials: CsI, NaI, CaF₂, and BaF₂

For pure systems, the scintillation light is due mostly to the radiative decay of an excited state resulting from the recombination of an electron with a self-trapped hole. Therefore, the magnitude of the fraction of recombined electrons and its variation among different materials is of great interest. The fraction of recombined electrons as a function of the incident γ -ray energy is shown in Fig. 3(a) for all four materials. The error bars were calculated as the standard deviation of the mean when the electron-hole pair tracks were divided into five groups. The fraction of recombined electrons generally decreases with increasing incident energy. This is due to the fact that the stopping power increases at low incident energies thus generating high electron-hole pair densities at these energies, which, in turn, leads to an increased probability for electron-hole

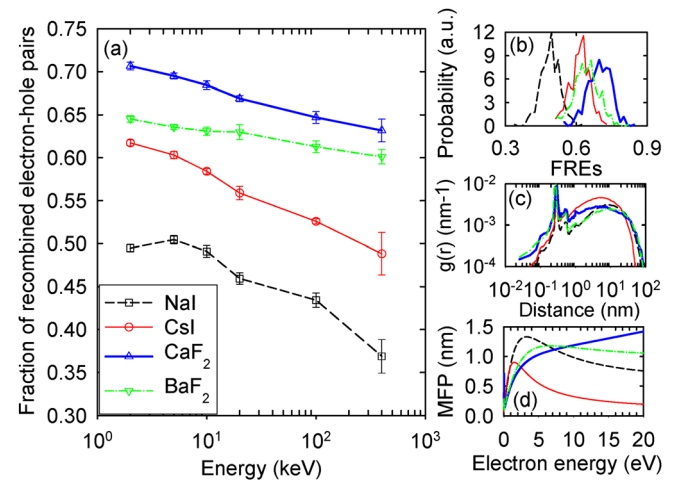


FIG. 3. (a) Fraction of recombined electron-hole pairs as a function of incident γ -ray energy. (b) Distributions of the fractions of recombined electrons (FREs). (c) Initial electron-hole pair distribution functions. (b) and (c) are for an incident γ -ray energy of 2 keV. (d) Electron mean free paths as a function of electron energy.

pair recombination. The fraction of recombined electrons for CsI increases by about 10%, at all energies, relative to the values reported in our previous work.¹⁶ This change is due to the modifications made to the values of some of the simulation parameters, namely, the electron effective mass, the screening correction parameter, and the energy cutoff. An important observation is that the distribution of the fraction of recombined electrons at a given incident energy shows a somewhat wide distribution for all materials, as shown in Fig. 3(b) for 2-keV incident γ -rays. The distributions are fairly symmetrical as the averaged value is close to the peak position. For pure CsI, the distributions of the fraction of recombined electrons at incident energies of 2, 5, and 10 keV were fitted to a Gaussian distribution, as shown in Fig. S1.³⁰ The values of the fitting parameters are shown in Table S1.³⁰ The full width at half maximum is seen to decrease with increasing incident energy, which is consistent with the experimental observation that the intrinsic energy resolution of pure CsI decreases (i.e., the energy resolution improves) with increasing incident energy.³⁸

Fig. 3(a) also shows that the fraction of recombined electrons is different for the four materials. These differences are due to several factors.

(1) MFP. The mean free path was calculated as follows:

$$MFP = \frac{1}{\sqrt{m^*} / 2E_i \sum_{j=1}^4 \tau_j}, \quad (13)$$

where τ_j is the electron-phonon scattering rate of process j , and j is one of the four electron-phonon interactions listed in Sec. II. Fig. 3(d) shows the MFP for each material. A longer MFP means that electrons scatter over longer distances after an electron-phonon interaction, which translates into a decreased likelihood for recombination as the electrons travel further away from the initial track of immobile self-trapped holes.

(2) LO phonon energy. A large LO phonon energy means that electrons are slowed down quickly and thus are more likely to reside near the self-trapped hole track, which increases the probability for recombination.

(3) The initial electron-hole pair density. To describe the initial electron-hole pair density, we use the electron-hole pair distribution function, $g(r)$, which is calculated by

$$g(r) = \frac{n(r)}{N_E N_H \Delta r}, \quad (14)$$

where $n(r)$ represents the number of electron-hole distances within the range $r + \Delta r$, and N_E and N_H are the numbers of electrons and holes in the track, respectively. Fig. 3(c) shows the $g(r)$ distributions obtained for all materials. A greater proportion of short electron-hole distances will lead to an increased probability for electron-hole pair recombination.

(4) Static dielectric constant. As described in Sec. II, one of the conditions used to evaluate whether an electron and a hole have recombined is to determine whether their electrostatic interaction energy is higher than the electron

kinetic energy. As a result, higher static dielectric constants means that the electron-hole electrostatic interactions are better screened and thus the fraction of recombined electrons is less.

Based on these factors, the fractions of recombined electrons shown in Fig. 3(a) can be explained as follows. CaF_2 has both the greatest proportion of short initial electron-hole pair distances and the largest LO phonon energy of the four materials, which explains why it has the largest fraction of recombined electron-hole pairs. In contrast, NaI has the lowest proportion of short initial electron-hole pair distances, the longest MFP at energies lower than its highest initial electron kinetic energy, and also one of the lowest LO phonon energies and, therefore, displays the lowest fraction of recombined electrons. Although BaF_2 has a greater MFP than CsI for most energies lower than its highest initial electron kinetic energy, it has both a higher LO phonon energy than CsI and a greater proportion of short initial electron-hole pair distances; therefore, BaF_2 shows a higher extent of electron-hole pair recombination than CsI. Differences in static dielectric constant between CsI (5.65) and NaI (7.3) and between CaF_2 (6.80) and BaF_2 (7.36) are small but are consistent with the fact that CsI shows a greater fraction of recombined electron-hole pairs than NaI and that of CaF_2 is higher than that of BaF_2 . It should be noted that a direct correlation between the calculated fractions of recombined electron-hole pairs and the experimental light yields of these pure materials cannot be done based on these results alone as the light yield will be strongly influenced by several processes occurring during the energy transfer stage, which follows the thermalization stage, such as the diffusion, radiative decay, and non-radiative decay of excitons, the ability of separated electron-hole pairs to recombine after thermalization, and the presence of activators and defects.

As discussed above, a significant fraction of the electrons recombine with self-trapped holes during thermalization (recombined electrons). The remaining electrons travel through the lattice until they reach thermal energy (stopped electrons). Figs. 4(a) and 4(b) show, respectively, the thermalization distance distributions of the recombined and stopped electrons obtained from the interaction of 2-keV incident γ -rays with all four pure materials considered. The thermalization distance is defined as the distance between the final and initial positions of an electron. The two sets of distributions show very different behaviors. For the recombined electrons, the distributions decay very rapidly, which means that the electrons recombine with self-trapped holes before they can travel long distances. For the stopped electrons, the distributions show a rapid rise to a maximum followed by a long tail. All four distributions peak between approximately 25 and 50 nm, in the following increasing order of peak position: CaF_2 , BaF_2 , NaI, and CsI. Fig. 4(b) also shows that the shorter the peak position, the higher its probability and the faster the distribution decays.

Figs. 5(a) and 5(b) show the thermalization time distributions of the recombined and stopped electrons, respectively, obtained from the same simulations. The thermalization time is defined as the time it takes before an electron either is stopped or recombines with a self-trapped

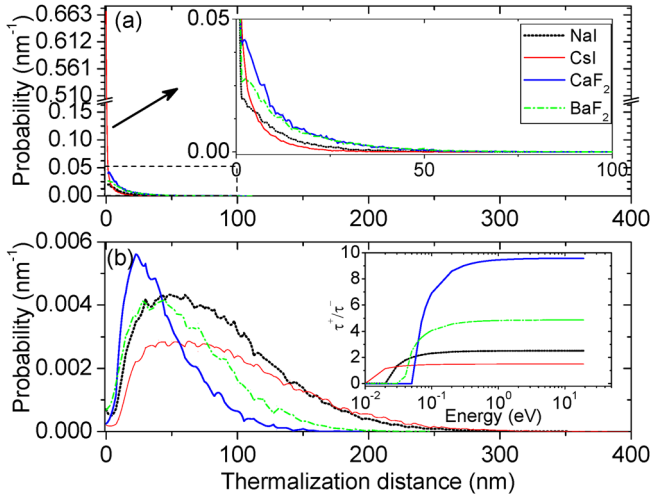


FIG. 4. Thermalization distance distributions for the (a) recombined and (b) stopped electrons for a 2-keV incident γ -ray. The inset in (b) shows the ratio of LO phonon creation and LO phonon annihilation scattering rates.

hole. The thermalization time distributions display the same behavior as the thermalization distance distributions, with an increasing order of maximum extent as follows: CaF_2 (~ 0.5 ps), BaF_2 (~ 1 ps), NaI (~ 2 ps), and CsI (~ 7 ps) for the stopped electrons. The time distribution of CsI was enlarged in the inset of Fig. 5(b) to discern its fine structure. As can be seen in Fig. 5(b), the time distributions of the four materials are all composed of three peaks. The NaI time distribution shows three peaks at 0.25, 0.75, and 1.5 ps, CsI at 1, 3, and 5 ps, CaF_2 at 0.1, 0.25, and 0.35 ps, and BaF_2 at 0.1, 0.55, and 0.75 ps. The first peak corresponds to the electrons generated through interband transitions. As discussed in our previous work,¹⁶ the second and the third peaks correspond to the electrons generated through plasmon decay and those that reached the energy cutoff after electron-phonon interactions, respectively.

The time and distance distributions for the stopped electrons of CsI differ in two ways from those reported in our previous paper¹⁶ as a result of changes in a few parameters. First, Figs. 4(b) and 5(b) do not show peaks at 0 nm and 0 ps in the

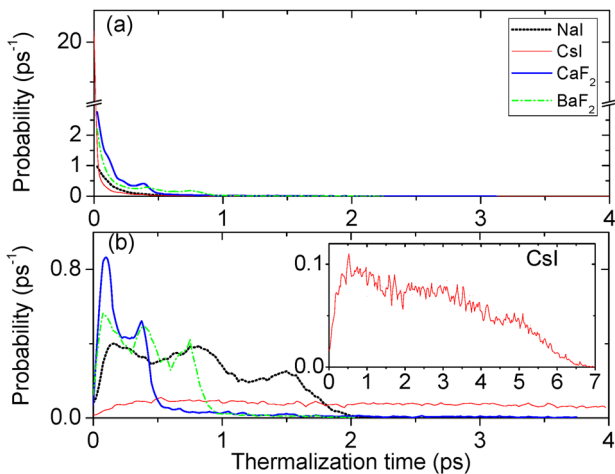


FIG. 5. Thermalization time distributions for the (a) recombined and (b) stopped electrons for a 2-keV incident γ -ray. The inset in (b) shows an enlarged view of the time distribution of CsI .

CsI thermalization distance and time distributions, respectively, unlike what was predicted in our previous work (Fig. 5 of Ref. 16). This is due to the fact that the thermal energy is used instead of the electron affinity as the energy cutoff in this work. Because the thermal energy (~ 0.025 eV) is much lower than the CsI electron affinity (~ 0.1 eV), the probability for an electron to have an initial kinetic energy lower than the energy cutoff is greatly reduced. This means that fewer electrons are stopped before the start of the simulation and that electrons with low initial kinetic energies can travel further. As a result, the peaks previously found at 0 nm and 0 ps disappear and are replaced by an initial rise. Second, in our previous work, the distance distribution extended up to ~ 1000 nm whereas it does not go beyond ~ 400 nm here. Similarly, the thermalization time distribution is calculated to be narrower. This is caused by the modification of the electron effective mass and the screening correction parameter.

The ordering observed in both the distance and time distributions of the stopped electrons is due mostly to the LO phonon scattering rates and the LO phonon energy. The greater the ratio of the phonon creation rate to the phonon annihilation rate (τ_{LO}^+/τ_{LO}^-), the more favored phonon creation is over phonon annihilation and, therefore, the faster the electrons will lose energy to the lattice. As can be deduced from Eqs. (1) and (2) of the SI,³⁰ τ_{LO}^+/τ_{LO}^- becomes solely dependent on the LO phonon energy as the electron energy increases and becomes much larger than the LO phonon energy ($\lim_{E \rightarrow \infty} \tau_{LO}^+/\tau_{LO}^- = (n_q + 1)/n_q = \exp(\hbar\omega_{LO}/k_B T)$). Therefore, this means that the greater the LO phonon energy, the faster the rate of energy loss to the lattice. The inset of Fig. 4(b) shows that the ratios of the creation to annihilation scattering rates converge to 9.6, 4.9, 2.5, and 1.5 for CaF_2 , BaF_2 , NaI , and CsI , respectively, since the LO phonon energies are 0.0565, 0.0396, 0.023, and 0.01 eV for CaF_2 , BaF_2 , NaI , and CsI , respectively. In addition to a greater τ_{LO}^+/τ_{LO}^- ratio, a higher LO phonon energy means that more energy is lost to the lattice for each phonon creation event. Consequently, the ordering of the four LO phonon energies correlates with the peak positions and widths of the thermalization time and distance distributions of the stopped electrons. Finally, as observed in our previous work, the thermalization time and distance distributions did not show any incident-energy dependence, as shown in Fig. S2.³⁰

The ability of electron-hole pairs to recombine during the energy transfer stage will be dependent, in part, on the extent of separation between the self-trapped holes and the stopped electrons as a result of the thermalization process. Therefore, we calculated the distributions of the nearest electron-hole distances for the stopped electrons at the end of the thermalization simulations obtained for the four materials and 2-keV incident γ -rays (Fig. S3 (Ref. 30)). Although the distributions show large fluctuations, they are all centered around 20–40 nm. In addition, the distributions first rise at 7.8, 9.8, 8.3, and 7.5 nm for NaI , CsI , CaF_2 , and BaF_2 , respectively, which means that there is no stopped electron within this radius from each self-trapped hole after thermalization. These values are essentially identical to the Onsager radii of those materials, which are 7.6, 9.9, 8.2, and 7.6 nm at 300 K for NaI , CsI , CaF_2 , and BaF_2 , respectively. For CsI ,

the present results differ slightly from those presented in Ref. 16, in which two distinct peaks were predicted rather than one. As before, this is caused by the fact that the energy cutoff was changed from the material's electron affinity to the thermal energy. As the energy cutoff is reduced, electrons with a low initial kinetic energy can travel further than before and, as a result, the peak previously found at ~ 5 nm is shifted to longer distances and merges with the second peak.

B. Doped materials: CsI(Tl) and NaI (Tl)

Scintillator materials are commonly doped with activators, such as thallium for the alkali iodides, for use as radiation detection materials. In our previous work,¹⁶ we studied the effect of doping on the electron thermalization process in Tl-doped CsI. Therefore, based on the results obtained in the previous section, in this section, we extend our work to Tl-doped NaI to investigate whether Tl doping can affect the electron thermalization process differently between the two materials. BaF₂ was not considered as it is typically used as a pure scintillator. CaF₂ is commonly doped with europium; however, there is at present no approach to determine the relative values of γ for Tl and Eu in Eq. (1) and thus there is no way to differentiate the two dopants. As a result, we chose to study the difference between two materials doped with the same dopant. A value of 0.56 was used for γ as used in our previous study,¹⁶ which also contained a discussion of the dependence of the simulation results upon the value of γ .

Fig. 6 shows the fraction of Tl-trapped electrons as a function of Tl concentration for concentrations up to 1.0 mol. %. A thallium ion becomes Tl⁰ when trapping an electron; therefore, Tl⁰ is synonym to a Tl-trapped electron. As expected, the fraction of Tl-trapped electrons increases and those of the recombined and stopped electrons decrease with increasing Tl concentration. In addition, the fraction of Tl-trapped electrons shows an asymptotic behavior as a function of Tl concentration. At low Tl concentrations, both materials show the same extent of trapping at Tl sites and a difference between the fractions of recombined electrons similar to that obtained with the pure materials. Interestingly,

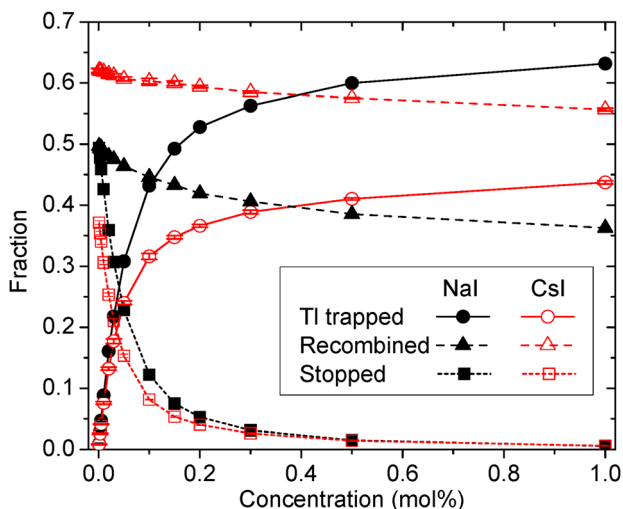


FIG. 6. Fraction of Tl-trapped electrons and recombined electron-hole pairs as a function of Tl concentration for an incident γ -ray energy of 2 keV.

the fraction of Tl-trapped electrons in NaI(Tl) is larger than that in CsI(Tl) as the Tl concentration increases beyond 0.1 mol. %. This result can be attributed to two reasons. First, the larger size of Cs⁺ compared to Na⁺ means that the atomic density of NaI is greater than that of CsI and that, therefore, the trapping probability given by Eq. (1) is higher for NaI than for CsI, for a given Tl mol. %. Second, as shown in Fig. 3(d), the NaI MFP is greater than that of CsI, which translates into an increased probability of capture according to Eq. (1). Both facts lead to a greater extent of trapping in NaI. Correspondingly, fewer electrons are available for recombination with self-trapped holes and the NaI fraction decreases more.

The Tl concentration in commercially available NaI(Tl) and CsI(Tl) scintillators is usually around 0.1 mol. %. Therefore, this dopant concentration was employed to investigate the incident energy dependence of the electron populations. Fig. 7 shows the changes in the fractions of stopped, recombined, and Tl-trapped electrons as a function of γ -ray incident energy for CsI and NaI doped with a Tl concentration of 0.1 mol. %. For both materials, the fraction of Tl-trapped electrons increases with increasing incident energy to the detriment of the fraction of recombined electrons, while the fraction of stopped electrons remains practically constant. The probability that a given electron will recombine with a self-trapped hole rather than being captured at a Tl⁺ site is an increasing function of the density of the self-trapped holes, hence an increasing function of the ionization density. As observed for the pure materials, because the stopping power diminishes with increasing incident energy, the ionization density also decreases and thus the fraction of recombined electrons diminishes. As discussed in our previous work,¹⁶ this result agrees well with the experimental findings of Syntfeld-Kazuch *et al.*,³⁹ who showed that the intensity of the light component corresponding to the prompt creation of a thallium excited state, either via nonthermal capture of an electron and a hole at the same Tl⁺ site or via exciton capture^{40,41} decreased with increasing incident energy, and that the intensity of the light component which is generally

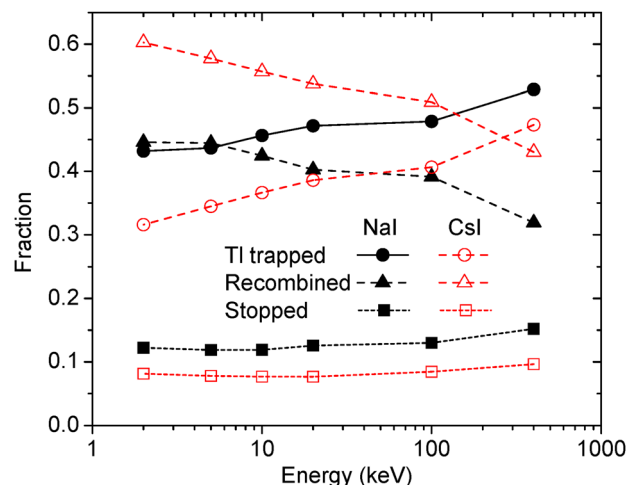


FIG. 7. Fraction of Tl-trapped, stopped and recombined electrons as a function of incident γ -ray energy for a Tl concentration of 0.1 mol. %.

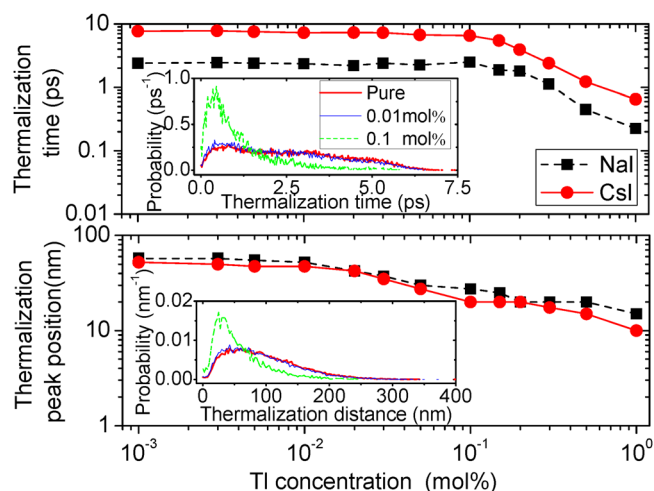


FIG. 8. (a) Maximum thermalization time and (b) thermalization distance peak of the stopped electrons as a function of Tl concentration for an incident γ -ray energy of 2 keV. Inset shows the thermalization distance and time distributions for three Tl concentrations in CsI.

assigned to binary processes involving the formation of Tl^0 species increased with increasing incident energy.

Finally, the maximum value of the thermalization time distribution and the position of the thermalization distance distribution maximum of the stopped electrons were determined as a function of Tl concentration for 2-keV incident γ -rays in order to investigate the effect of Tl concentration on the thermalization process in Tl-doped CsI and NaI (Fig. 8). Because the thermalization time distributions show multiple peaks (Fig. 5(b)), the maximum value was used instead of the position of the distribution maximum. As shown in Fig. 8(a), at concentrations lower than 0.1 mol. %, the maximum value of the thermalization time shows little dependence on the Tl concentration, whereas it decreases as the concentration increases beyond 0.1 mol. %. This is caused by the fact that most of the electrons are trapped at Tl sites as the Tl concentration increases beyond 0.05 mol. %. The change in the thermalization distance peak position with Tl concentration is shown in Fig. 8(b). The trend is the same as observed for the maximum thermalization time except for the fact that the peak position begins to shift to lower values for concentrations higher than 0.01 mol. %. Importantly, the extents of change in the maximum thermalization time and the position of the thermalization distance maximum are similar for both alkali iodides. The results presented in Fig. 8 indicate that Tl doping can significantly reduce the time and spatial scales of electron thermalization in alkali iodides.

IV. CONCLUSIONS

In this work, the electron thermalization process in pure and Tl-doped alkali iodides (CsI and NaI) and pure alkaline-earth halides (CaF_2 and BaF_2) was simulated using a Monte Carlo model. For all four pure materials, a large fraction of the electrons rapidly recombine with self-trapped holes. The distances the electrons that avoid recombination travel during thermalization show a distribution that peaks between approximately 25 and 50 nm and that can extend to a few hundreds of nanometers. The time required for all the elec-

trons to reach thermal energy varies from approximately 0.5 ps for CaF_2 to 7 ps for CsI. The LO phonon energy was found to be the major parameter determining the differences in thermalization time and distance between the four pure materials. The extent of electron-hole pair recombination was also found to vary among the four pure materials and the electron mean free path, LO phonon energy, initial electron-hole pair density, and static dielectric constant were identified as the principal factors responsible for these variations. For CsI, some quantitative changes were observed compared to our previous publication¹⁶ due to changes in the cutoff energy, the algorithm for simulating plasmon decay, and the approach used to calculate the electron effective mass and the screening correction parameter; however, the conclusions reached in our previous publication were not affected by these changes.

The effect of doping CsI and NaI with thallium was also investigated. In our previous publication,¹⁶ it was shown that the fraction of Tl-trapped electrons increases with increasing incident γ -ray energy to the detriment of the fraction of recombined electron-hole pairs. This was found, in this work, to also be true for Tl-doped NaI. However, the fraction of Tl-trapped electrons was greater for NaI than for CsI. This difference is due to the higher atomic density and the longer electron mean free path of NaI compared to CsI.

ACKNOWLEDGMENTS

The authors would like to acknowledge Professor A. Akkerman for insightful discussions. This research was supported by the National Nuclear Security Administration, Office of Nuclear Nonproliferation Research and Engineering (NA-22), of the U.S. Department of Energy (DOE).

- ¹J. E. Jaffe, D. V. Jordan, and A. J. Peurrung, *Nucl. Instrum Methods A* **570**, 72 (2007).
- ²S. Kerisit, K. M. Rosso, B. D. Cannon, F. Gao, and Y. Xie, *J. Appl. Phys.* **105**, 114915 (2009).
- ³P. Dorenbos, J. T. M. de Haas, and C. W. E. van Eijk, *IEEE Trans. Nucl. Sci.* **42**, 2190 (1995).
- ⁴W. W. Moses, S. A. Payne, W.-S. Choong, G. Hull, and B. W. Reutter, *IEEE Trans. Nucl. Sci.* **55**, 1049 (2008).
- ⁵R. B. Murray and A. Meyer, *Phys. Rev.* **122**, 815 (1961).
- ⁶R. T. Williams, K. B. Ucer, J. Q. Grim, K. C. Lipke, L. M. Trefilova, and W. W. Moses, *IEEE Trans. Nucl. Sci.* **57**, 1187 (2010).
- ⁷R. T. Williams, Q. Li, J. Q. Grim, K. B. Ucer, G. Bizarri, and W. W. Moses, *Proc. SPIE* **7805**, 78050K (2010).
- ⁸Q. Li, J. Q. Grim, R. T. Williams, G. A. Bizarri, and W. W. Moses, *J. Appl. Phys.* **109**, 123716 (2011).
- ⁹R. T. Williams, J. Q. Grim, Q. Li, K. B. Ucer, and W. W. Moses, *Phys. Status Solidi B* **248**, 426 (2011).
- ¹⁰J. Singh, *J. Appl. Phys.* **110**, 024503 (2011).
- ¹¹F. Gao, L. W. Campbell, R. Devanathan, Y. Xie, L. R. Corrales, A. J. Peurrung, and W. J. Weber, *Nucl. Instrum. Methods A* **579**, 292 (2007).
- ¹²F. Gao, L. W. Campbell, R. Devanathan, Y. Xie, Y. Zhang, A. J. Peurrung, and W. J. Weber, *Nucl. Instrum. Methods B* **255**, 286 (2007).
- ¹³F. Gao, L. W. Campbell, Y. Xie, R. Devanathan, A. J. Peurrung, and W. J. Weber, *IEEE Trans. Nucl. Sci.* **55**, 1079 (2008).
- ¹⁴F. Gao, Y. Xie, S. Kerisit, L. W. Campbell, and W. J. Weber, *Nucl. Instrum. Methods Phys. Res. A* **652**, 564 (2011).
- ¹⁵S. Kerisit, K. M. Rosso, and B. D. Cannon, *IEEE Trans. Nucl. Sci.* **55**, 1251 (2008).
- ¹⁶Z. Wang, Y. L. Xie, B. D. Cannon, L. W. Campbell, F. Gao, and S. Kerisit, *J. Appl. Phys.* **110**, 064903 (2011).

- ¹⁷R. Hofstadter, *Phys. Rev.* **74**, 100 (1948).
- ¹⁸M. Laval, M. Moszyński, R. Allemand, E. Cormoreche, P. Guinet, R. Odru, and J. Vacher, *Nucl. Instrum. Methods* **206**, 169 (1983).
- ¹⁹J. Menefee, C. F. Swinehart, and E. W. O'Dell, *IEEE Trans. Nucl. Sci.* **13**, 720 (1966).
- ²⁰S. L. Adler, *Phys. Rev.* **126**, 413 (1962).
- ²¹N. Wisner, *Phys. Rev.* **129**, 62 (1963).
- ²²X. Gonze, J. M. Beuken, R. Caracas, F. Detraux, M. Fuchs, G. M. Rignanesse, L. Sindic, M. Verstraete, G. Zerah, F. Jollet, M. Torrent, A. Roy, M. Mikami, P. Ghosez, J. Y. Raty, and D. C. Allan, *Comput. Mater. Sci.* **25**, 478 (2002).
- ²³L. Hedin, *Phys. Rev.* **139**, A796 (1965).
- ²⁴A. Akkerman, T. Boutboul, A. Breskin, R. Chechik, and A. Gibrekhterman, *J. Appl. Phys.* **76**, 4656 (1994).
- ²⁵T. Boutboul, A. Akkerman, A. Gibrekhterman, A. Breskin, and R. Chechik, *J. Appl. Phys.* **86**, 5841 (1999).
- ²⁶J. P. Ganachaud, C. Attard, and R. Renoud, *Phys. Status Solidi B* **199**, 175 (1997).
- ²⁷J. Llacer and E. L. Garwin, *J. Appl. Phys.* **40**, 2766 (1969).
- ²⁸M. Sparks, D. L. Mills, R. Warren, T. Holstein, A. A. Maradudin, L. J. Sham, E. Loh, Jr., and D. F. King, *Phys. Rev. B* **24**, 3519 (1981).
- ²⁹J. N. Bradford and S. Woolf, *J. Appl. Phys.* **70**, 490 (1991).
- ³⁰See supplementary material at <http://dx.doi.org/10.1063/1.4736088> for the formulation employed to model electron thermalization, distributions of the fractions of recombined electron-hole pairs for CsI for incident γ -rays of energies 2, 5, and 10 keV and values of the fitting parameters, thermalization distance, and time distributions for the stopped electrons as obtained for incident γ -ray with different energies, and distributions of the nearest electron-hole distances for the stopped electrons after thermalization for a 2-keV incident γ -ray.
- ³¹M. V. Fischetti, D. J. DiMaria, S. D. Brorson, T. N. Theis, and J. R. Kirtley, *Phys. Rev. B* **31**, 8124 (1985).
- ³²M. V. Fischetti, *Phys. Rev. Lett.* **53**, 1755 (1984).
- ³³A. L. Ankudinov, B. Ravel, J. J. Rehr, and S. D. Conradson, *Phys. Rev. B* **58**, 7565 (1998).
- ³⁴T. Boutboul, A. Akkerman, A. Breskin, and R. Chechik, *J. Appl. Phys.* **84**, 2890 (1998).
- ³⁵C. Kittel, *Introduction to Solid State Physics*, 8th ed. (Wiley, 2005).
- ³⁶C. J. Carlile and B. T. M. Willis, *Acta Crystallogr. Sec. A* **45**, 708 (1989).
- ³⁷J. C. Ashley, R. H. Ritchie, and O. H. Crawford, in *Proceedings of the 10th Werner Brandt Conference* (1988), p. 329.
- ³⁸M. Moszyński, M. Balcerzyk, W. Czarnacki, M. Kapusta, W. Klamra, P. Schotanus, A. Syntfeld, M. Szawłowski, and V. Kozlov, *Nucl. Instrum. Methods A* **537**, 357 (2005).
- ³⁹A. Syntfeld-Każuch, M. Moszyński, Ł. Świdorski, W. Klamra, and A. Nassalski, *IEEE Trans. Nucl. Sci.* **55**, 1246 (2008).
- ⁴⁰M. M. Hamada, F. E. Costa, M. C. C. Pereira, and S. Kubota, *IEEE Trans. Nucl. Sci.* **48**, 1148 (2001).
- ⁴¹H. B. Dietrich and R. B. Murray, *J. Lumin.* **5**, 155 (1972).
- ⁴²T. P. de Silans, I. Maurin, P. C. D. Segundo, S. Saltiel, M. P. Gorza, M. Ducloy, D. Bloch, D. D. S. Meneses, and P. Echegut, *J. Phys. Condens. Matter* **21**, 255902 (2009).
- ⁴³C. Andeen, J. Fontanel, and D. Schuele, *Rev. Sci. Instrum.* **41**, 1573 (1970).
- ⁴⁴S. Eros and J. R. Reitz, *J. Appl. Phys.* **29**, 683 (1958).
- ⁴⁵K. Reinitz, *Phys. Rev.* **123**, 1615 (1961).
- ⁴⁶S. Speziale and T. S. Duffy, *Phys. Chem. Miner.* **29**, 465 (2002).
- ⁴⁷J. M. Leger, J. Haines, A. Atouf, O. Schulte, and S. Hull, *Phys. Rev. B* **52**, 13247 (1995).
- ⁴⁸I. Richman, *J. Chem. Phys.* **41**, 2836 (1964).
- ⁴⁹R. T. Williams and K. S. Song, *J. Phys. Chem. Solids* **51**, 679 (1990).
- ⁵⁰T. Tsujibayashi, K. Toyoda, S. Sakuragi, M. Kamada, and M. Itoh, *Appl. Phys. Lett.* **80**, 2883 (2002).

physica **p** status **s** solidi **s**

www.pss-journals.com

reprint



Kinetic Monte Carlo simulations of excitation density dependent scintillation in CsI and CsI(Tl)

Zhiguo Wang¹, Richard T. Williams², Joel Q. Grim², Fei Gao¹, and Sebastien Kerisit^{*1}

¹Fundamental and Computational Sciences Directorate, Pacific Northwest National Laboratory, Richland, WA 99352, USA

²Department of Physics, Wake Forest University, Winston-Salem, NC 27109, USA

Received 6 December 2012, revised 7 February 2013, accepted 13 February 2013

Published online 14 March 2013

Keywords inorganic scintillators, kinetic Monte Carlo, nonlinear quenching, non-proportionality, scintillation mechanisms

* Corresponding author: e-mail sebastien.kerisit@pnnl.gov, Phone: 509-371-6382, Fax: 509-371-1226

Nonlinear quenching of electron–hole pairs in the denser regions of ionization tracks created by γ -ray and high-energy electrons is a likely cause of the light yield non-proportionality of many inorganic scintillators. Therefore, kinetic Monte Carlo (KMC) simulations were carried out to investigate the scintillation properties of pure and thallium-doped CsI as a function of electron–hole pair density. The availability of recent experimental data on the excitation density dependence of the light yield of CsI following ultraviolet excitation allowed for an improved parameterization of the interactions between self-

trapped excitons (STE) in the KMC model via dipole–dipole Förster transfer. The KMC simulations reveal that nonlinear quenching occurs very rapidly (within a few picoseconds) in the early stages of the scintillation process. In addition, the simulations predict that the concentration of thallium activators can affect the extent of nonlinear quenching as it has a direct influence on the STE density through STE dissociation and electron scavenging. This improved model will enable more realistic simulations of the non-proportional γ -ray and electron response of inorganic scintillators.

© 2013 WILEY-VCH Verlag GmbH & Co. KGaA, Weinheim

1 Introduction High-energy photons and electrons that penetrate scintillator materials create tracks of electron–hole pairs, also referred to as ionization tracks, with densities that vary as the energetic particle slows down inside the solid. Relaxation of ionization tracks eventually leads to the emission of many lower-energy scintillation photons, a phenomenon that is exploited, for example, in radiation detection and γ -ray spectroscopy. Key scintillation properties, such as emission spectra, decay times, and light yields, strongly depend on the kinetics and efficiency of the relaxation of ionization tracks. The variation of the ionization track density as a function of the incident particle energy can also lead to non-proportionality, a phenomenon whereby the yield of scintillation photons normalized to the incident energy is not constant with incident energy. Although the non-proportionality of inorganic scintillators has been studied quite intensively (see for example, reviews [1–4] and references therein), its underlying mechanisms remain incompletely identified.

From a solid state physics perspective, non-proportionality challenges our understanding of (i) the dependence of

ionization tracks on incident particle energy, (ii) the relaxation of small high-excitation-density regions, and (iii) the competition among the processes that dictate the light yields of scintillators. From an application perspective, non-proportionality is the main source of degradation of the energy resolution in radiation detection and γ -ray spectroscopy with inorganic scintillators [5, 6] and, therefore, there is great interest in understanding the root cause(s) of non-proportionality in order to help guide the search for new and improved scintillator materials.

Significant progress has been made towards developing models of the elementary processes that take place in ionization tracks and give rise to the electron or photon response of inorganic scintillators. These elementary processes include the creation of excited states, the transport of excited carriers through the scintillator lattice, and the quenching of excitations as they propagate. Approaches employed to model these processes include minimalist phenomenological models [7, 8], kinetic models [9–13], diffusion models [14–16], and microscopic models that explicitly deal with individual electron–hole pairs [17–20].

Accurately describing the rate and extent of nonlinear quenching in conditions relevant to ionization tracks has amounted to one of the most challenging tasks faced by scintillation models to date; mostly due to the considerable difficulties in obtaining experimental data for parameterization and validation of the models. For example, we previously used kinetic Monte Carlo simulations (KMC) to evaluate the contribution of an annihilation mechanism between self-trapped excitons (STE) to the non-proportional scintillation response of pure CsI at low temperature [18]. Although the KMC simulations suggested that STE–STE annihilation could account for the non-proportional behavior of CsI, this process could not be independently parameterized and its probability was used as a variable.

Fortunately, experimental data on nonlinear quenching is now beginning to become available [15, 16, 21–27]. For example, Williams and co-workers recently investigated the excitation density dependence of the light yield of pure and thallium-doped CsI and NaI using ultraviolet (UV) excitation [16, 27]. In these experiments (referred to hereafter as z-scan experiments), 0.5-ps pulses of 5.9-eV light were used to generate electron–hole pair densities estimated to be consistent with the denser regions of ionization tracks created by γ -rays and energetic electrons. The excitation density was controlled by varying the distance between the sample and the UV-beam waist thus allowing for scintillation decay curves and light yields to be determined as a function of excitation density.

Therefore, in this work, we make use of a KMC model of scintillation mechanisms in CsI and CsI(Tl), developed in a previous study [17] and based on the kinetic model of Dietrich and Murray [28], to model the excitation density dependence of the kinetics and efficiency of scintillation in the z-scan experiments. Our aim is to identify the relevant elementary processes, determine and parameterize the extent of nonlinear quenching due to STE–STE interactions, and thus develop a more accurate model for simulating the relaxation of ionization tracks. The KMC model makes use of an explicit atomistic representation of the crystal lattice, thallium sites and individual electron–hole pairs and assigns probabilities for each individual elementary process based on rate parameters (i.e., activation energies and pre-exponential factors).

One of the advantages of the KMC model is that it can use as input realistic ionization tracks produced by the Monte Carlo code NWEGRIM (Northwest Electron and Gamma Ray Interaction in Matter) [29–32]. NWEGRIM follows the collisions of each individual particle generated during the energy cascade and can generate a microscopic-level three-dimensional description of ionization tracks. Therefore, in combination with progress made recently in simulating electron thermalization in alkali and alkaline-earth halides [19, 20], these techniques and models provide a path toward modeling the response of inorganic scintillators at the level of individual electron–hole pairs. Such an approach is attractive as it has the potential ultimately to account for any heterogeneity of the ionization tracks, scintillator lattice, or

activator distribution, incorporate input from first-principles calculations, and lead to the development of a predictive simulation framework.

The focus of this study is on CsI, pure and thallium doped, as it was studied in both our previous modeling work [17] and the experimental work of Williams and co-workers [16, 27]. It should be noted that CsI is also attractive for its wide-spread use as a radiation detection material, simple crystal structure, large deviation from proportionality and frequent use as a model system for studying non-proportionality.

2 Computational methods

2.1 Kinetic Monte Carlo model

The KMC model was developed and implemented in a previous study [17] and was based on the model originally developed by Dietrich and Murray [28] to describe the kinetics of scintillation of thallium-doped alkali halides. In the KMC model, the scintillator lattice and all the relevant species are represented explicitly and the diffusion of self-trapped holes (STH) and STE is treated using a random-walk approach. The model considers a number of scintillation processes, as illustrated in Fig. 1.

All electron–hole pairs begin the simulations as STE, for reasons to be explained in Sections 2.3 and 3.1. STEs can diffuse through the lattice and be trapped at Tl^+ sites. STEs can also decay radiatively or non-radiatively or interact via dipole–dipole Förster transfer, a non-radiative transfer whereby a first STE decays by emitting a virtual phonon, which is absorbed by a second STE. In addition, STEs can undergo dissociation. Indeed, recent picosecond time-resolved measurements of optical absorption by Williams and co-workers [33] showed that, in CsI doped with 0.3 mol% of Tl, the absorption band due to STEs decayed on the time scale of picoseconds and was replaced by a band that was assigned to Tl^0 . This experimental result indicates that a STE electron, possibly in an excited bound state, may be scavenged by tunneling transfer to a nearby Tl^+ site to

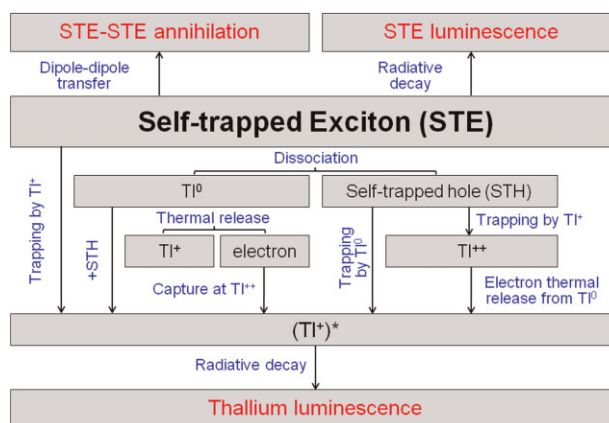


Figure 1 (online color at: www.pss-b.com) Schematic of the elementary species (black), elementary processes (blue), and possible final outcomes (red) considered in the KMC model of scintillation.

form Tl^0 . Therefore, the dissociation of a STE results in the formation of a STH and a Tl^0 site. A STH can diffuse through the lattice and trap at Tl^+ or Tl^0 and Tl^0 can release its electron to be trapped at a Tl^{++} site and thus form $(Ti^+)^*$.

Overall, scintillation light can be emitted by radiative decay of either STE or excited thallium ions, which can be formed by three different mechanisms: (i) diffusion of a STE and capture at a Tl^+ site; (ii) diffusion of a STH and capture at a Tl^0 site; and (iii) diffusion of a STH and capture at a Tl^+ site to form Tl^{++} , followed by thermal release of an electron from a Tl^0 site and capture at Tl^{++} .

For each elementary process, the rate, k , is described by an Arrhenius equation,

$$k = A \exp\left(\frac{-W}{k_B T}\right), \quad (1)$$

where A is the pre-exponential factor, W the activation energy, k_B the Boltzmann constant, and T is the temperature. In previous work [18], second-order quenching of STEs was simulated by assigning a probability for annihilation when a STE hopped to a site already occupied by another STE. This is replaced in this work by dipole–dipole Förster transfer between STEs. Förster transfer is an exception to Eq. (1) in that the rate is dependent on the distance between STEs [34]:

$$k(r) = B \left(\frac{R_{dd}}{r}\right)^6, \quad (2)$$

where R_{dd} is the Förster transfer radius and B is set to the STE radiative decay rate following the formulation of Vasil'ev [34] used subsequently by Kirm et al. [21] and Williams et al. [16]. The model parameters are given in Table 1 and discussed in the next section.

The KMC algorithm is executed using the following algorithm: (i) the rate of each process is calculated using Eqs. (1) or (2); (ii) a process is selected with a probability proportional to its rate using a random number; (iii) the selected process is executed; (iv) time is increased by $-\ln x/\Gamma$, where x is another random number and Γ is the sum of all rates. Steps (i)–(iv) are repeated until all electron–hole pairs have undergone radiative or non-radiative decay or have been quenched.

Table 1 Parameters of the KMC model of scintillation.

process	A (s^{-1})	W (eV)
STH diffusion	5.1×10^{12}	0.1500
STE diffusion	5.1×10^{12}	0.1500
STE radiative decay	7.1×10^8	0.0000
STE non-radiative decay	1.0×10^{10}	0.1160
STE dissociation ^a	1.7×10^{11}	0.0000
$(Ti^+)^*$ radiative decay	6.0×10^7	0.0662
electron thermal release from Tl^0	8.8×10^6	0.0880
process	R_{dd} (a_0)	B (s^{-1})
dipole–dipole Förster transfer	8	1.7×10^8

^aThis process can take place only if a Tl^+ is available within a $3a_0$ radius.

2.2 Origin of the model parameters Eight processes are considered in the KMC model. Six processes were included in the derivation of the original KMC model [17]: STH and STE diffusion, STE radiative and non-radiative decay, $(Ti^+)^*$ radiative decay, and electron thermal release from Tl^0 . Two processes were added for the purposes of this work: STE dissociation and dipole–dipole Förster transfer. All the parameters related to these eight processes are given in Table 1.

STH diffusion occurs via thermally activated hopping to nearest-neighbor sites following 90 or 180° hops of the STH [35]. Initial assignment of the two peaks of thermoluminescence below 100 K (at approximately 60 and 90 K) observed by Sidler et al. [35] led to the conclusion that the 180° hop had a lower activation energy than the 90° one in CsI. However, Barland et al. [36] showed that there was no thermoconductivity peak associated with the 60 K thermoluminescence peak and that its isothermal decay exhibited a $1/t$ dependence, strongly suggesting that this peak was due to recombination through tunneling and not diffusion via 180° hops. Therefore, there is no experimental consensus on the relative activation energies of the two possible hops. Derenzo and Weber [37] computed an activation energy of 0.15 eV for the 180° hop using MP2 level of theory but they did not compute the activation energy for the 90° hop; therefore, this value was used for both types of hops in the KMC simulations. As before [17], the value derived by Keller and Murray [38] from thermal-reorientation experiments of STHs in KI was used for the pre-exponential factor.

At low temperatures, pure CsI shows two main STE emission bands but as the temperature is increased to room temperature only one wide band is observed [39]. Nishimura et al. [39] suggested that the wide band at room temperature originates from the on-center configuration of the STEs (it should be noted that other researchers have shown evidence for the interaction of multiple excitations as a possible alternate origin of this emission [40, 41]). Because the radiative lifetime of the singlet on-center STE is shorter than that of the triplet, the rate of dipole–dipole Förster transfer will be faster for the singlet state. In addition, the experimental data of Williams et al. [16] used in this work for comparison were subject to surface quenching that reduces the observed radiative lifetime. This competing surface quenching depletes the slower triplet light yield more than the faster singlet light yield. Both effects suggest that the experimental data are mainly representing the singlet channel. Therefore, as was done in the original KMC model [17], we make the simplifying assumption that the STE emission in pure CsI originates from a single type of STE at room temperature. However, there is no experimental data available on the activation energy and pre-exponential factor for STE hopping in CsI. Previously [17], the STE diffusion parameters were estimated from a combination of the data on STH and STE hopping in NaI and that on STH hopping in CsI and resulted in STE diffusion being faster than STH diffusion. However, recent electronic structure calculations by two research groups have shown that STEs and STHs are

equally mobile in NaI [42, 43] and this finding is expected to extend to CsI. Therefore, the energy barrier and pre-exponential factors for STEs in CsI were set to be the same as those used for STHs.

In the original KMC model [17], the parameters for STE radiative and non-radiative decay were fitted to the experimental light yield and decay time of pure CsI obtained by Amsler et al. [44] as a function of temperature and under excitation by 511 and 1275 keV γ -rays. The fit initially produced a very small value for the activation energy of the STE radiative decay process (0.011 eV) and a second fit with this activation energy fixed to zero yielded equivalent temperature dependence of the light yield and decay time. Therefore, W in Eq. (1) was set to zero in this work. The STE lifetime derived by Williams et al. [16] from the decay of the STE luminescence of UV-excited pure CsI was shorter than that measured in the bulk by Nishimura et al. [39]. Williams et al. suggested that this shortening of the lifetime for UV excitation was due to quenching on surface defects, which could provide an additional channel for STE decay. Therefore, because this study focuses on modeling the experimental results of Williams et al., the pre-exponential factor of the STE radiative decay process was changed to the inverse of the lifetime derived by Williams et al. to implicitly account for surface quenching.

The parameters for electron thermal release and $(\text{Ti}^+)^*$ radiative decay were derived in the original model from the temperature dependence of the scintillation light measured by Valentine et al. [45] following excitation of CsI(Tl) with 511 keV γ -rays. These parameters were kept in the current model with the exception of the pre-exponential factor for $(\text{Ti}^+)^*$ radiative decay, which was increased from 1.9×10^7 to 6.0×10^7 to improve the agreement with the kinetics of $(\text{Ti}^+)^*$ luminescence reported by Williams et al. [16]. This was a fairly small modification; although Williams et al. [16] did not compare their observed $(\text{Ti}^+)^*$ lifetime to previous work, it is possible that, again, differences in excitation energy and densities slightly affected the rate of $(\text{Ti}^+)^*$ radiative decay in their experiments.

Turning now to the two processes that were added in the current version of the model, there is no available experimental data to directly parameterize the STE dissociation process; therefore, the rate assigned to this process was based on the observation of Williams et al. [33], from their time-resolved optical absorption data, that the band assigned to STEs essentially disappeared within 6 ps (i.e., the pre-exponential factor for this process was set to $1.67 \times 10^{11} \text{ s}^{-1}$ while the activation energy was set to zero as temperature dependent data would be needed to extract the activation energy). For the dipole–dipole Förster transfer, the parameter B was set to the STE radiative decay rate in analogy with the formulation of Vasil'ev [34]. To exclude the effect of surface quenching and for consistency with the original KMC model [17], B was set to the inverse of the lifetime measured by Amsler et al. [44] in the bulk and at room temperature (6 ns). As one of the goals of this work is to derive parameters for describing nonlinear quenching based

on the experimental data of Williams and co-workers [16, 27], the value of R_{dd} was varied by increments of a_0 , the CsI lattice parameter, while the other model parameters were kept fixed, until agreement with the z-scan experiments was obtained.

Finally, we note that, in the original KMC model, a prompt capture radius of 1.4 nm was used to model non-thermal capture of holes at Ti^+ sites, as suggested by Hadley et al. [46] and Kaufman et al. [47] in their experimental studies of KI(Tl) and NaI(Tl). This process was not included in the current model as all the electron–hole pairs begin the simulations as STEs. The data compared here are for photon excitation at 5.9 eV, whereas the work of Hadley et al. and Kaufman et al. used X-ray irradiation. In addition, as noted by Williams et al. [16], the excitation energy used in their experiments does not significantly overlap with the D band of Ti^+ , which should produce negligible direct excitation of Ti^+ .

2.3 Simulation setup The KMC model uses a simple cubic lattice whereby each lattice point represents one unit cell (i.e., 1 Cs^+ ion and 1 I^- ion). In alkali halides, a STH is localized on two neighboring halide ions and forms an X_2^- molecular ion or V_{k} center. A V_{k} center can capture an electron to form a STE. Therefore, STHs and STEs are represented in the KMC model as occupying two neighboring unit cells.

The KMC simulations were set to represent as closely as possible the conditions of the z-scan experiments. Based on a band gap energy of 6.05 eV for CsI at 20 K [48] and the observation that the band gap decreases with increasing temperature, the photon energy of the UV pulse in the z-scan experiments (5.9 eV) was close to the band gap energy and higher than the 1s exciton peak (5.6 eV) [49]. The comparison of one-photon [50] and two-photon [48] absorption spectra at low temperature give an experimental exciton binding energy of about 250 meV. Therefore, excitons are stable at room temperature and STEs are stable also, as evidenced by their efficient radiative emission. Therefore, the electron–hole pairs were all assumed to begin the simulations as STE. The STEs were placed on the lattice following an exponentially decaying distribution: $N(z) = N_0 \exp(-\alpha z)$, where z is the depth from the surface in lattice layers, $N(z)$ is the number of excitons at depth z , and α is the absorption coefficient. The absorption coefficient used here was set to approximately twice that derived experimentally by Williams et al. [16] (i.e., 5.0×10^5 vs. $2.7 \times 10^5 \text{ cm}^{-1}$) to give a characteristic length of 20 nm instead of 37 nm and thus reduce the extent of the z direction needed in the simulations to encompass the STE distributions. A test simulation was run for $\alpha = 2.7 \times 10^5 \text{ cm}^{-1}$, but no significant change was observed.

The simulation cell was a three-dimensional lattice of dimensions $32 \times 32 \times 256$ sites. Given a lattice parameter of 0.457 nm for CsI, this corresponds to real dimensions of $14.6 \times 14.6 \times 117 \text{ nm}^3$. The UV beam was assumed to be incident along the z direction. Periodic boundary conditions were applied in the directions perpendicular to the beam but

not in the direction of the beam. The $z = 0$ boundary represented the crystal surface. Given the length of the simulation cell in the z direction relative to the absorption coefficient, the STE population was extremely small at the other z boundary. TI^+ sites were placed randomly on the lattice to achieve the desired concentration. All the simulations were carried out at room temperature.

Knowing the on-axis laser fluence, the absorption coefficient, the excitation energy, and the position of the beam waist relative to the sample surface, the excitation density can be calculated and parameterized by its value N_0 at the sample surface. The same range of values as used experimentally was used here for N_0 .

3 Results

3.1 Light yield of CsI:0.3% TI as a function of excitation density A series of KMC simulations were performed to calculate the light yield of CsI:0.3% TI as a function of excitation density. The excitation densities were taken from the experimental estimates, as described in Section 2.3. For each excitation density, the light yield was determined using the average of 400 simulations. Although not necessarily true in practice because of the increase in background light for the positive side, the positive and negative sides of the z -scan should be identical and therefore, for the KMC simulations, the positive side was obtained by simply taking the mirror image of the negative side.

Recent z -scan measurements by Grim et al. [27] comparing $\text{Bi}_4\text{Ge}_3\text{O}_{12}$, NaI:Tl, and CsI:Tl at 5.9-eV excitation indicate that CsI:Tl does not follow purely second-order quenching kinetics (Förster transfer) but shows some contribution from a third-order quenching process (e.g., Auger recombination). Because this work focuses on second-order quenching, a fit to the experimental data with a mixed 2nd/3rd order analytical model [27] was carried out and only the second-order component is considered further in our KMC simulations with Förster transfer. Future work will investigate the effects of incorporating a third-order quenching process in the KMC simulations applied to z -scan experiments with UV excitation energies higher than 5.9 eV and to ionization tracks of high-energy electrons.

The value of R_{dd} was changed in increments of a_0 (i.e., 0.457 nm) until the best possible agreement with the second-order component of the experimental data was obtained. Figure 2 shows the excitation density dependent light yield obtained for $R_{\text{dd}} = 8a_0$ along with the yield obtained experimentally from the z -scan experiments and the second-order component [27]. A value of $8a_0$ for R_{dd} corresponds to 3.66 nm, which is close to the value of 3.8 nm derived by Grim et al. [27] from their analytical fit. Notably, Kirm et al. [21] and Nagirnyi et al. [22] derived values of 2.1 and 3 nm, respectively, for Förster transfer in CdWO_4 using the same analytical model as used subsequently by Williams and co-workers [16, 27].

Figure 2 shows that excellent agreement with the second-order component of the experimental data can be obtained within the framework of the KMC simulations.

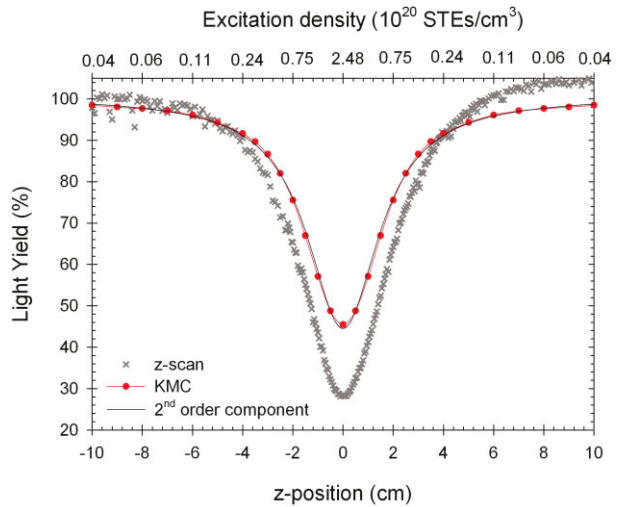


Figure 2 (online color at: www.pss-b.com) Calculated light yield as a function of z -position and excitation density and comparison with the z -scan data and second-order component of Grim et al. [27].

3.2 Scintillation kinetics of CsI:0.3% TI as a function of excitation density Although the KMC model can reproduce the efficiency of the scintillation process, there remains to determine whether the same model parameters can yield an accurate description of the kinetics of scintillation. Therefore, in Fig. 3, the scintillation decay curves obtained at two excitation densities from 20000 KMC simulations are compared to those reported by Williams et al. [16]. Experimentally, no noticeable differences were found between the high and low excitation densities and therefore a single curve is shown in Fig. 3 for the experimental data.

As seen experimentally, the KMC model shows a rising time of a few nanoseconds. Experimentally, the scintillation maximum was found at approximately 6.2 ns. The KMC simulations show a slightly delayed maximum; although the

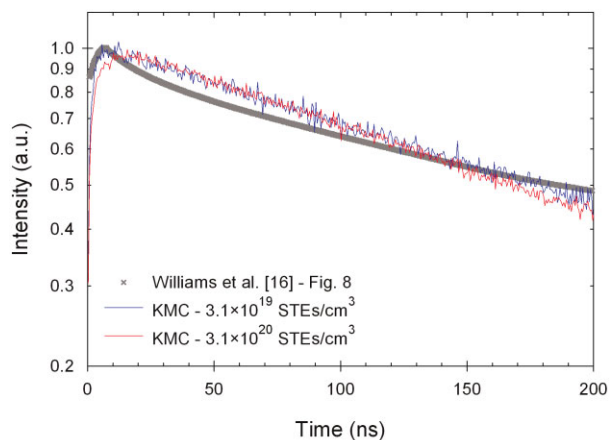


Figure 3 (online color at: www.pss-b.com) Decay curves of the $(\text{TI}^+)^*$ emission of CsI:0.3%TI calculated at two excitation densities and comparison with the results of Williams et al. [16].

resolution of the streak camera on the 200 ns frame scale is likely to be lower than the difference between the simulations and measurements. In the KMC simulations, the high excitation density curve shows a slight increase after scintillation reaches its intensity maximum, relative to that obtained at low excitation density, and a corresponding slightly faster decrease at later times. Again, it is possible that such differences are too subtle to be observed within the uncertainties of the experimental apparatus employed by Williams et al. [16]. Experimentally, no quenching of the $(\text{TI}^+)^*$ emission was observed with increasing excitation density, which strongly suggests that nonlinear quenching occurs before excitations are trapped at TI^+ sites and not within the $(\text{TI}^+)^*$ population. Therefore, this process was not included in the KMC model and the results shown in Fig. 3 indicate that, indeed, such a process is not needed to give a good account of the kinetics of the $(\text{TI}^+)^*$ emission.

3.3 Scintillation kinetics of pure CsI as a function of excitation density

The same two excitation densities were considered to determine the kinetics of scintillation of pure CsI. As before, the scintillation decay curves were obtained by averaging 20 000 simulations. The agreement is good except in the first 0.3 ns. This can be explained by the fact that there is a finite time required for the formation of STEs from free electrons and holes that is not taken into account in the KMC simulations since all electron–hole pairs are assumed to begin the simulations as STEs. We note that the data of Williams et al. [16] shown in Fig. 4 does not correspond to their raw data but to their fits before introducing the bimolecular growth function that accounts for the rising time of the STE luminescence. The calculated scintillation decay curves also show similar features to the experimental curves reported by Kirm et al. [21] for CdWO_4 , with fast initial decay followed by exponential decay at later time and greater deviation from exponential decay initially at high excitation densities.

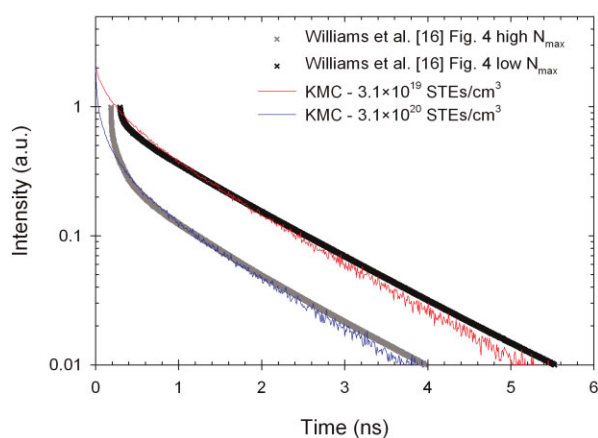


Figure 4 (online color at: www.pss-b.com) Decay curves of the STE emission of pure CsI calculated at two excitation densities and comparison with the curve fits of Williams et al. [16].

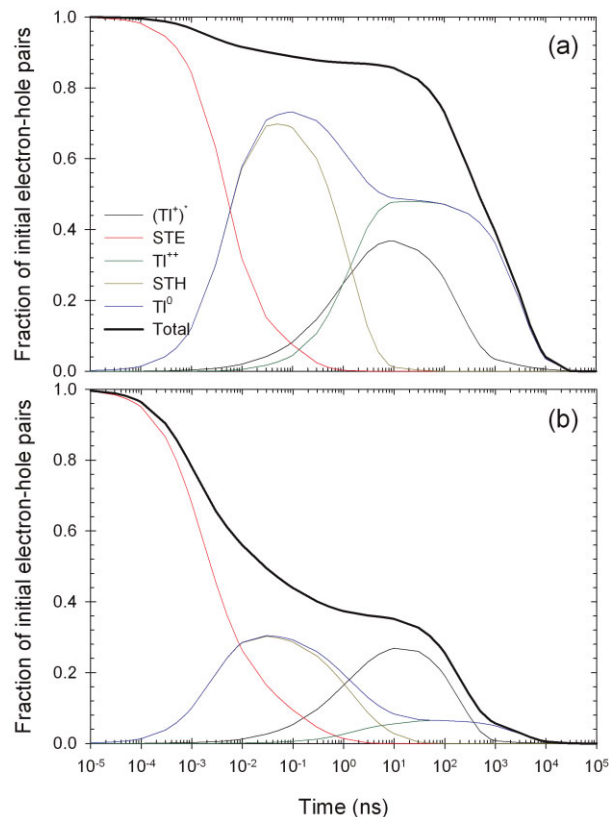


Figure 5 (online color at: www.pss-b.com) Time evolution of the populations of the species considered in the KMC model for CsI:0.3% Tl at (a) low excitation density (3.1×10^{19} STEs/cm³) and (b) high excitation density (3.1×10^{20} STEs/cm³).

4 Discussion The time evolution of the populations of each species (STE, STH, TI^{++} , TI^0 , and $(\text{TI}^+)^*$) are shown in Fig. 5 for excitation densities 3.1×10^{19} and 3.1×10^{20} STEs/cm³. The general sequence of events is as follows. Early on, on the time scale of picoseconds or even sub-picoseconds, the STE population diminishes due to dipole–dipole Förster transfer and electron scavenging by TI^+ sites. The latter process appears to culminate at approximately 10 ps, at which point the STH population does not equal the TI^0 population anymore as the diffusing STHs begin to trap at TI^+ sites to form TI^{++} or $(\text{TI}^+)^*$ species. By about 10 ns, all the STHs have been trapped at Tl sites and the TI^0 and TI^{++} populations thus become equal in size. Beyond this point, recombination only takes place via thermal release of electrons from TI^0 to TI^{++} sites to form $(\text{TI}^+)^*$.

There is no noticeable increase of the $(\text{TI}^+)^*$ population until the STE population has almost completely vanished, suggesting that Tl excitation through STE capture is limited in these conditions and occurs via binary electron–hole recombination instead. This is consistent with the findings of Dietrich et al. [51] for Tl-doped alkali halides excited with high-energy electrons. Interestingly, the KMC simulations indicate that there are two stages in which the population of

electron–hole pairs diminishes (thick black curves in Fig. 5): the nonlinear quenching and photon emission stages; and that these two stages are temporally well separated at both low and high excitation densities. Consequently, results such as those presented in Fig. 5 can help further experimental investigations of scintillation processes by identifying the relevant time scale needed to probe particular mechanisms.

As noted above, the STE population decays mostly via dissociation to form STH and TI^0 sites on the scale of picoseconds. This is consistent with the time-resolved optical absorption data of Williams et al. [33]. In their study, Williams et al. used a pump-probe laser setup to determine the transient infrared absorption spectra of CsI induced by sub-picosecond two-photon band-gap excitation at room temperature. The absorption band assigned to STEs was seen to disappear in 5–10 ps after excitation of the CsI sample doped with 0.3 mol% Tl, whereas the band assigned to TI^0 rose within the same time scale. The experimental findings of Williams et al. are consistent with the transient optical absorption measurements of Yakovlev et al. [52], which indicated the presence of only STH and TI^0 on the time scale of nanoseconds after excitation of a Tl-doped CsI crystal at 80 K. Because the experimental data of Williams et al. [33] guided the parameterization of the STE dissociation process, it is not surprising to observe this agreement; however, the KMC simulations do confirm that STE dissociation is a viable process at this time scale given the other active processes. For example, if STE dissociation happened at a slower rate, the KMC model predicts that a greater extent of Förster transfer and STE radiative and non-radiative decay would be observed, which would be inconsistent with the z-scan and kinetics data.

It is important to note that the STE dissociation process is necessary for the model to account for all experimental observations consistently. Indeed, although the STEs diffuse at the same rate as the STHs in the KMC simulations and thus could potentially explain the rising time observed in the $(\text{TI}^+)^*$ scintillation kinetics, the kinetics of STE emission indicate that the STEs radiatively decay at a rate that is too fast to allow them to survive long enough to diffuse to and be captured at TI^+ sites. Figure 4 indicates that at least 99% of the STEs have decayed or quenched by 5 ns, i.e., approximately the time it takes to reach the maximum of the $(\text{TI}^+)^*$ luminescence curve (Fig. 3). Therefore, the dissociation mechanism prevents the STEs from decaying radiatively or annihilating via dipole–dipole Förster transfer. This strongly suggests that nonlinear quenching occurs in the very early stages and over a very short amount of time relative to the overall scintillation process.

Finally, given the ability of the KMC model to describe accurately the kinetics and efficiency of scintillation in CsI:0.3% Tl and the kinetics of scintillation in pure CsI, we used this model to predict the effect of Tl concentration on the extent of nonlinear quenching. Figure 6 shows the light yield as a function of excitation density for pure CsI and CsI doped with 0.1 and 0.3 mol% Tl, whereby each curve is normalized to the light yield at -10 cm. It should be noted

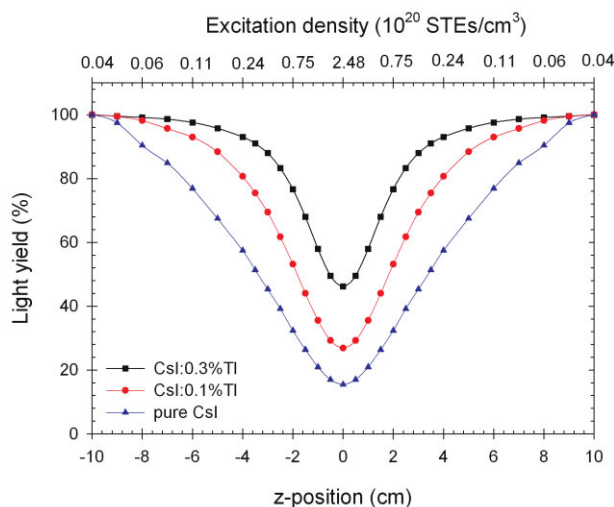


Figure 6 (online color at: www.pss-b.com) Calculated light yield as a function of z-position and excitation density for pure CsI and CsI doped with 0.1 or 0.3 mol% Tl.

that the KMC model may not include all the processes that are affected by the Tl concentration. For example, it does not explicitly account for surface quenching of STEs and this process is likely to play an increasing role as the Tl concentration decreases. However, Fig. 6 suggests that one effect of decreasing the Tl concentration is to increase the relative extent of quenching. This effect is due to a lower extent of STE dissociation at lower Tl concentrations, which allows the STEs to survive longer and thus increases the amount of dipole–dipole Förster transfer, thereby leading to a greater extent of nonlinear quenching. This is supported by the time-resolved optical absorption study of Williams et al. [33] discussed above, which also showed that the rate and extent of conversion between the STE and TI^0 bands was slower for the CsI sample doped with 0.01 mol% Tl versus that doped with 0.3 mol% Tl. The simulations also predict a slight increase in STE emission when decreasing the Tl concentration from 0.3 to 0.1 mol% Tl, in agreement with experimental luminescence spectra [16].

5 Conclusions A KMC model of scintillation mechanisms in CsI and CsI(Tl), previously developed for simulating the kinetics and efficiency of scintillation of γ -ray irradiated CsI [17], was modified to extend its applicability to high excitation densities. Specifically, a distance-dependent dipole–dipole Förster transfer process was added to the KMC model. Recent experimental data on the excitation density dependence of scintillation light yields offered an unprecedented opportunity to parameterize this process for CsI. Within the framework of the KMC model, good agreement was obtained with the kinetics and efficiency of the scintillation of UV-excited CsI samples. The simulations were then used to identify the general sequence of events following UV excitation and the time evolution of the populations of the principal species involved

in the scintillation process. This approach provides a unique opportunity to calibrate STE–STE interaction parameters for other scintillators. Such microscopic models of scintillation mechanisms can be used in combination with γ -ray-induced ionization tracks calculated by NWEGRIM to investigate the non-proportional response of CsI and other inorganic scintillators.

Acknowledgements The authors acknowledge Drs. Luke W. Campbell, Micah Prange, Renee M. Van Ginhoven, and YuLong Xie for insightful discussions. This research was supported by the National Nuclear Security Administration, Office of Nuclear Nonproliferation Research and Engineering (NA-22), of the U.S. Department of Energy (DOE).

References

- [1] P. Dorenbos, J. T. M. de Haas, and C. W. E. van Eijk, *IEEE Trans. Nucl. Sci.* **42**, 2190 (1995).
- [2] J. E. Jaffe, D. V. Jordan, and A. J. Peurrung, *Nucl. Instrum. Methods A* **570**, 72 (2007).
- [3] W. W. Moses, S. A. Payne, W.-S. Choong, G. Hull, and B. W. Reutter, *IEEE Trans. Nucl. Sci.* **55**, 1049 (2008).
- [4] W. W. Moses, G. A. Bizarri, R. T. Williams, S. A. Payne, A. N. Vasil'ev, J. Singh, Q. Li, J. Q. Grim, and W.-S. Choong, *IEEE Trans. Nucl. Sci.* **59**, 2038 (2012).
- [5] M. Moszyński, J. Zalipska, M. Balcerzyk, M. Kapusta, W. Mengesha, and J. D. Valentine, *Nucl. Instrum. Methods Phys. Res. A* **484**, 259 (2002).
- [6] M. Moszyński, *Nucl. Instrum. Methods Phys. Res. A* **505**, 101 (2003).
- [7] S. A. Payne, N. J. Cherepy, G. Hull, J. D. Valentine, W. W. Moses, and W.-S. Choong, *IEEE Trans. Nucl. Sci.* **56**, 2506 (2009).
- [8] S. A. Payne, W. W. Moses, S. Sheets, L. Ahle, N. J. Cherepy, B. Sturm, S. Dazeley, G. Bizarri, and W.-S. Choong, *IEEE Trans. Nucl. Sci.* **58**, 3392 (2011).
- [9] G. Bizarri, W. W. Moses, J. Singh, A. N. Vasil'ev, and R. T. Williams, *J. Appl. Phys.* **105**, 044507 (2009).
- [10] G. Bizarri, W. W. Moses, J. Singh, A. N. Vasil'ev, and R. T. Williams, *J. Lumin.* **129**, 1790 (2009).
- [11] G. Bizarri, W. W. Moses, J. Singh, A. N. Vasil'ev, and R. T. Williams, *Phys. Status Solidi C* **6**, 97 (2009).
- [12] G. Bizarri, N. J. Cherepy, W.-S. Choong, G. Hull, W. W. Moses, S. A. Payne, J. Singh, J. D. Valentine, A. N. Vasilev, and R. T. Williams, *IEEE Trans. Nucl. Sci.* **56**, 2313 (2009).
- [13] J. Singh, *J. Appl. Phys.* **110**, 024503 (2011).
- [14] Q. Li, J. Q. Grim, R. T. Williams, G. A. Bizarri, and W. W. Moses, *J. Appl. Phys.* **109**, 123716 (2011).
- [15] R. T. Williams, Q. Li, J. Q. Grim, K. B. Ucer, G. Bizarri, and W. W. Moses, *Proc. SPIE* **7805**, 1 (2010).
- [16] R. T. Williams, J. Q. Grim, Q. Li, K. B. Ucer, and W. W. Moses, *Phys. Status Solidi B* **248**, 426 (2011).
- [17] S. Kerisit, K. M. Rosso, and B. D. Cannon, *IEEE Trans. Nucl. Sci.* **55**, 1251 (2008).
- [18] S. Kerisit, K. M. Rosso, B. D. Cannon, F. Gao, and Y. Xie, *J. Appl. Phys.* **105**, 114915 (2009).
- [19] Z. Wang, Y.-L. Xie, B. D. Cannon, L. W. Campbell, F. Gao, and S. Kerisit, *J. Appl. Phys.* **110**, 064903 (2011).
- [20] Z. Wang, Y.-L. Xie, L. W. Campbell, F. Gao, and S. Kerisit, *J. Appl. Phys.* **112**, 014906 (2012).
- [21] M. Kirm, V. Nagirnyi, E. Feldbach, M. De Grazia, B. Carré, G. Geoffroy, J. Gaudin, N. Fedorov, P. Martin, A. Vasil'ev, and A. Belsky, *Phys. Rev. B* **79**, 233103 (2009).
- [22] V. Nagirnyi, S. Dolgov, M. Kirm, L. L. Nagornaya, F. Savikhin, V. Sirutkaitis, S. Vielhauer, and A. Vasil'ev, *IEEE Trans. Nucl. Sci.* **57**, 1182 (2010).
- [23] J. Q. Grim, Q. Li, K. B. Ucer, R. T. Williams, A. Burger, P. Bhattacharya, E. Tupitsyn, G. A. Bizarri, and W. W. Moses, *MRS Proc.* **1341**, 15 (2011).
- [24] J. Q. Grim, Q. Li, K. B. Ucer, R. T. Williams, and W. W. Moses, *Nucl. Instrum. Methods Phys. Res. A* **652**, 284 (2011).
- [25] J. Q. Grim, *Experimental and Computational Studies of Nonlinear Quenching in Materials used as Radiation Detectors*, Ph.D. Thesis, Wake Forest University, Winston-Salem, NC, 2012.
- [26] J. Q. Grim, K. B. Ucer, R. T. Williams, A. Burger, P. Bhattacharya, E. Tupitsyn, G. A. Bizarri, and W. W. Moses, *IEEE Symposium on Radiation Measurements and Applications*, Oakland, CA, USA (2012).
- [27] J. Q. Grim, K. B. Ucer, A. Burger, P. Bhattacharya, E. Tupitsyn, E. Rowe, V. M. Buliga, L. Trefilova, A. Gektin, G. A. Bizarri, W. W. Moses, and R. T. Williams, *Phys. Rev. B* (in press, 2013).
- [28] H. B. Dietrich, and R. B. Murray, *J. Lumin.* **5**, 155 (1972).
- [29] F. Gao, L. W. Campbell, R. Devanathan, Y. Xie, L. R. Corrales, A. J. Peurrung, and W. J. Weber, *Nucl. Instrum. Methods A* **579**, 292 (2007).
- [30] F. Gao, L. W. Campbell, R. Devanathan, Y. Xie, Y. Zhang, A. J. Peurrung, and W. J. Weber, *Nucl. Instrum. Methods B* **255**, 286 (2007).
- [31] F. Gao, L. W. Campbell, Y. Xie, R. Devanathan, A. J. Peurrung, and W. J. Weber, *IEEE Trans. Nucl. Sci.* **55**, 1079 (2008).
- [32] F. Gao, Y. Xie, S. Kerisit, L. W. Campbell, and W. J. Weber, *Nucl. Instrum. Methods Phys. Res. A* **652**, 564 (2011).
- [33] R. T. Williams, K. B. Ucer, J. Q. Grim, K. C. Lipke, L. M. Trefilova, and W. W. Moses, *IEEE Trans. Nucl. Sci.* **57**, 1187 (2010).
- [34] A. N. Vasil'ev, *IEEE Trans. Nucl. Sci.* **55**, 1054 (2008).
- [35] T. Sidler, J. P. Pellaux, A. Nouailhat, and M. A. Aegerter, *Solid State Commun.* **13**, 479 (1973).
- [36] M. Barland, E. Duval, and A. Nouailhat, *J. Phys. C, Solid State Phys.* **14**, 4237 (1981).
- [37] S. E. Derenzo, and M. J. Weber, *Nucl. Instrum. Methods A* **422**, 111 (1999).
- [38] F. J. Keller, and R. B. Murray, *Phys. Rev.* **150**, 670 (1966).
- [39] H. Nishimura, M. Sakata, T. Tsujimoto, and M. Nakayama, *Phys. Rev. B* **51**, 2167 (1995).
- [40] A. N. Belsky, A. N. Vasil'ev, V. V. Mikhailin, A. V. Gektin, P. Martin, C. Pedrini, and D. Bouttet, *Phys. Rev. B* **49**, 13197 (1994).
- [41] A. N. C. Belsky, R. Cortes, A. V. Gektin, P. Martin, V. V. Mikhailin, and C. Pedrini, *J. Lumin.* **72–74**, 93 (1997).
- [42] M. P. Prange, R. M. Van Ginhoven, N. Govind, and F. Gao, (in review, 2013).
- [43] B. Sadigh, D. Åberg, and P. Erhart, *IEEE Symposium on Radiation Measurements and Applications*, Oakland, CA, USA (2012).
- [44] C. Amsler, D. Grögler, W. Joffrain, D. Lindelöf, M. Marchesotti, P. Niederberger, H. Pruys, C. Regenfus, P. Riedler, and A. Rotondi, *Nucl. Instrum. Methods A* **480**, 494 (2002).

- [45] J. D. Valentine, W. W. Moses, S. E. Derenzo, D. K. Wehe, and G. F. Knoll, *Nucl. Instrum. Methods A* **325**, 147 (1993).
- [46] W. B. Hadley, S. Polick, R. G. Kaufman, and H. N. Hersh, *J. Chem. Phys.* **45**, 2040 (1966).
- [47] R. G. Kaufman, W. B. Hadley, and H. N. Hersh, *IEEE Trans. Nucl. Sci.* **17**, 82 (1970).
- [48] D. Fröhlich, B. Staginnus, and Y. Onodera, *Phys. Status Solidi* **40**, 547 (1970).
- [49] J. E. Eby, K. J. Teegarden, and D. B. Dutton, *Phys. Rev.* **116**, 1099 (1959).
- [50] K. Teegarden, and G. Baldini, *Phys. Rev.* **155**, 896 (1967).
- [51] H. B. Dietrich, A. E. Purdy, R. B. Murray, and R. T. Williams, *Phys. Rev. B* **8**, 5894 (1973).
- [52] V. Yakovlev, L. Trefilova, and A. Meleshko, *J. Lumin.* **129**, 790 (2009).



Pacific Northwest
NATIONAL LABORATORY

*Proudly Operated by **Battelle** Since 1965*

902 Battelle Boulevard
P.O. Box 999
Richland, WA 99352
1-888-375-PNNL (7665)

U.S. DEPARTMENT OF
ENERGY

www.pnnl.gov